Bioactive Materials 6 (2021) 4209–4242

Contents lists available at ScienceDirect

Bioactive Materials

journal homepage: www.sciencedirect.com/journal/bioactive-materials

MoS_2-based nanocomposites for cancer diagnosis and therapy

Jianling Wang [a,b,1], Lihua Sui [a,b,1], Jia Huang [a,b], Lu Miao [a,b], Yubing Nie [a,b], Kuansong Wang [c,d], Zhichun Yang [a,b,**], Qiong Huang [e], Xue Gong [f], Yayun Nan [g], Kelong Ai [a,b,*]

[a] Xiangya School of Pharmaceutical Sciences, Central South University, Changsha, 410078, China
[b] Hunan Provincial Key Laboratory of Cardiovascular Research, Xiangya School of Pharmaceutical Sciences, Central South University, Changsha, 410078, China
[c] Department of Pathology, Xiangya Hospital, Central South University, Changsha, Hunan, 410078, China
[d] Department of Pathology, School of Basic Medical Science, Central South University, Changsha, Hunan, 410013, China
[e] Department of Pharmacology, Xiangya Hospital, Central South University, Changsha, 410008, Hunan, China
[f] Department of Radiology, The Second Hospital of Jilin University, Changchun, 130041, China
[g] Geriatric Medical Center, Ningxia People's Hospital, Yinchuan, China

ARTICLE INFO

Keywords:
MoS_2
Cancer
Biosensor
Bioimaging
Chemotherapy
Phototherapy
Microwave hyperthermia
Combination therapy

ABSTRACT

Molybdenum is a trace dietary element necessary for the survival of humans. Some molybdenum-bearing enzymes are involved in key metabolic activities in the human body (such as xanthine oxidase, aldehyde oxidase and sulfite oxidase). Many molybdenum-based compounds have been widely used in biomedical research. Especially, MoS_2-nanomaterials have attracted more attention in cancer diagnosis and treatment recently because of their unique physical and chemical properties. MoS_2 can adsorb various biomolecules and drug molecules via covalent or non-covalent interactions because it is easy to modify and possess a high specific surface area, improving its tumor targeting and colloidal stability, as well as accuracy and sensitivity for detecting specific biomarkers. At the same time, in the near-infrared (NIR) window, MoS_2 has excellent optical absorption and prominent photothermal conversion efficiency, which can achieve NIR-based phototherapy and NIR-responsive controlled drug-release. Significantly, the modified MoS_2-nanocomposite can specifically respond to the tumor microenvironment, leading to drug accumulation in the tumor site increased, reducing its side effects on non-cancerous tissues, and improved therapeutic effect. In this review, we introduced the latest developments of MoS_2-nanocomposites in cancer diagnosis and therapy, mainly focusing on biosensors, bioimaging, chemotherapy, phototherapy, microwave hyperthermia, and combination therapy. Furthermore, we also discuss the current challenges and prospects of MoS_2-nanocomposites in cancer treatment.

1. Introduction

Cancer is one of the main causes of human death. The global cancer statistics released by the World Health Organization show that there were 18.1 million new cancer cases and 9.7 million deaths from cancer in 2018 [1]. The current main methods of cancer treatment are surgery, chemotherapy, and radiotherapy [2]. These therapies can only show limited efficacy [3]. The size of nanomaterials is between the size of biomolecules and cells. In theory, carefully designed nanomaterials can realize the regulation of cell state and function like organelles and exosomes. Nanomaterials for cancer treatment have been intensively studied in the past two decades. The latest advances in nanotechnology have made it possible to engineer complex nanostructures with unique physical properties and surface chemistry. Currently, nanomedicines for cancer have shown great potential compared to traditional therapeutic agents. Nanomaterials such as MoS_2, gold nanoparticles, MnO_2, iron oxide, carbon nanotubes and others have been widely developed for detection of cancer markers, imaging diagnosis, and treatment of cancer. Gold nanomaterials have a unique SPR effect and high X-ray attenuation coefficient, and can be used as efficient photothermal reagents and CT contrast agents for cancer. MnO_2 nanoparticles can catalyze H_2O_2 to generate oxygen (O_2), relieving tumor hypoxia and inhibiting cancer cell

Peer review under responsibility of KeAi Communications Co., Ltd.
* Corresponding author. Xiangya School of Pharmaceutical Sciences, Central South University, Changsha, 410078, China.
** Corresponding author. Xiangya School of Pharmaceutical Sciences, Central South University, Changsha, 410078, China.
E-mail addresses: yzhichun@csu.edu.cn (Z. Yang), aikelong@csu.edu.cn (K. Ai).
[1] There authors contributed equally to this work.

https://doi.org/10.1016/j.bioactmat.2021.04.021
Received 25 December 2020; Received in revised form 5 April 2021; Accepted 11 April 2021

proliferation and migration. Carbon nanotubes can be used as a good carrier of anti-cancer drug. Iron oxide nanoparticles (IONPs) that are one of the most promising magnetic resonance imaging (MRI) contrast agent precursors, which can be used for cancer diagnosis [4]. At the same time, IONPs can convert the magnetic energy of an alternating magnetic field into heat energy, effectively ablating cancer cells at high temperatures [5].

Among many nanomaterials, MoS_2 nanomaterials are extremely attractive in cancer diagnosis and treatment [6–9]. First, MoS_2 is a two-dimensional (2D) semiconductor nanomaterial, so it has the unique characteristics of 2D materials and the properties of semiconductors. These characteristics make it have great application prospects in cancer marker detection, cancer imaging, and treatment. Second, MoS_2 are easy to achieve controllable preparation. Many 2D nanomaterials such as graphene, Ti_3C_2Tx MXene, black phosphorus and others are generally prepared in a top-down manner. It is difficult to control the size, morphology and surface properties of 2D nanomaterials. MoS_2 nanomaterials can be synthesized in two ways, top-down and bottom-up. As a result, the controllable and precise synthesis of MoS_2 nanomaterials can be achieved according to the needs of cancer diagnosis and treatment. Third, MoS_2 nanomaterials is easy to functionalized with biomolecules and combined with other nanomaterials. Mo is a transition metal element with multiple valence states (from +1 to +6). MoS_2 nanomaterials is extremely flexible and easy to achieve surface modification and doping of other elements. Therefore, MoS_2 nanomaterials can also be used as a platform material to integrate other nanomaterials to form a multifunctional nanomedicine according to the require of cancer diagnosis and treatment. Finally, unlike many inorganic nanomaterials, such as gold nanomaterials, up-conversion nanomaterials, MoS_2 (sulfur and molybdenum) are composed of elements that exist in the human body. Mo is a trace element necessary for human survival [10]. Molybdenum-bearing enzymes play a key role in human metabolism, such as xanthine oxidase, aldehyde oxidase and sulfite oxidase. Insufficient intake of molybdenum in humans can lead to esophageal cancer [11]. Many studies have shown that MoS_2 nanomaterials has very good biocompatibility. In general, these advantages make MoS_2 nanomaterials very promising in cancer treatment and diagnosis.

MoS_2, as a diamagnetic compound with the property of semiconductor, exhibits excellent chemical and thermal stability. As shown in Fig. 1a, MoS_2 has a typical two-dimensional layered structure, which belongs to the hexagonal crystal system. Each layer consists of two sulfur (S) atoms and a molybdenum (Mo) atom, forming an S–Mo–S sandwich plate with a spacing of 0.315 nm. Meanwhile, each Mo atom and six S atom coordinating ligand to form a triangular prism or octahedral structure [12,13]. The layers with the spacing of 0.349 nm connected through the weak van der Waals force, as well as the stacking order of different S–Mo–S layers for the C axis constitute various MoS_2 crystal structures (Fig. 1b) [14].

As shown in Fig. 1c, 1T-MoS_2, 2H–MoS_2, and 3R–MoS_2 are three different crystal structures of MoS_2. The 1T-MoS_2 has a metastable phase structure that Mo atoms adopt octahedral coordination, while each S–Mo–S unit constitutes a crystal cell, resulting in metalloid or metallic properties of MoS_2. The 2H–MoS_2 structure is more stable that Mo atoms adopt trigonal prismatic coordination, in which two S–Mo–S units form

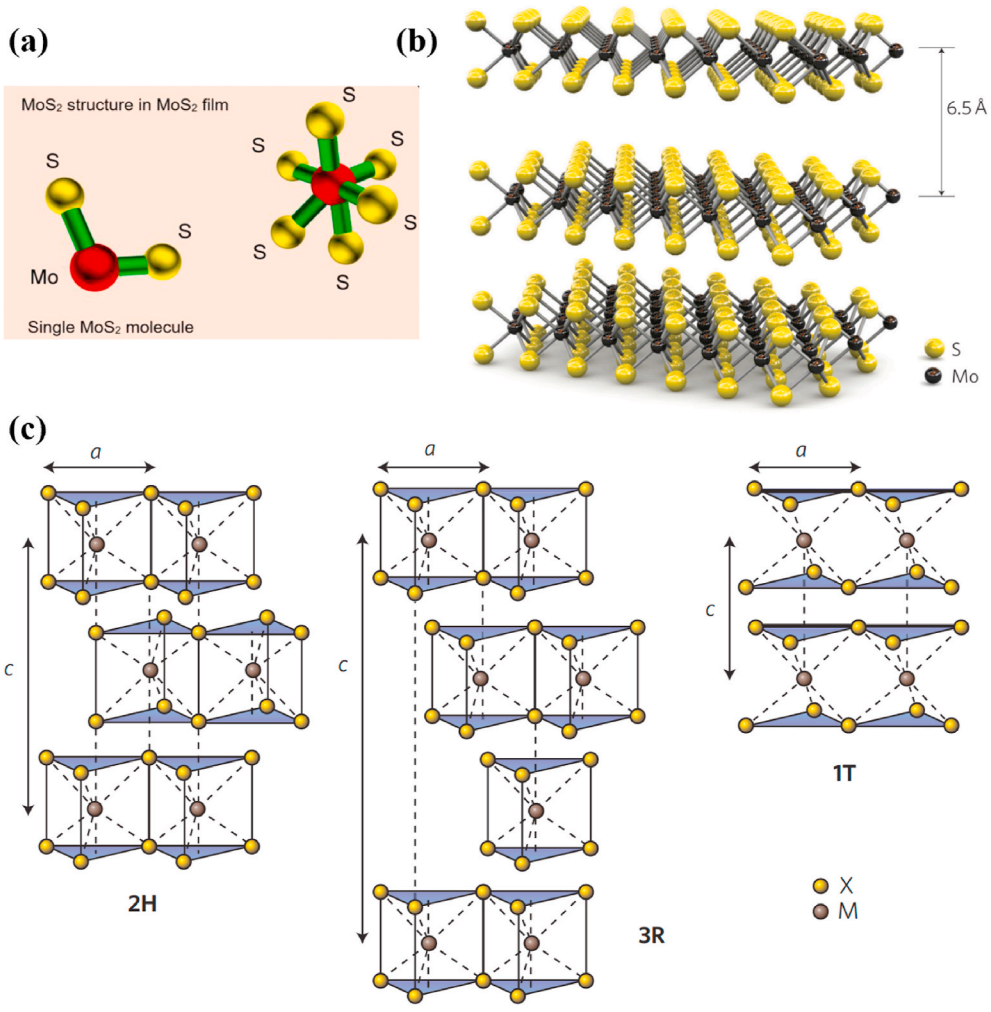

Fig. 1. (a) Structure of a single molybdenum disulphide molecule and an elemental unit of molybdenum disulphide film. Reprinted with permission from Ref. [13]. Copyright 2019, Journal of Physics D: Applied Physics. **(b)** Three dimensional representation of the structure of MoS_2. Reprinted with permission from Ref. [14]. Copyright 2011, Nature Nanotechnology. **(c)** Schematics of the structural polytypes: 1T (tetragonal symmetry, one layer per repeat unit, octahedral coordination), 2H (hexagonal symmetry, two layers per repeat unit, trigonal prismatic coordination) and 3R (rhombohedral symmetry, three layers per repeat unit, trigonal prismatic coordination). Reprinted with permission from Ref. [15]. Copyright 2012, Nature Nanotechnology.

a unit cell. The 3R–MoS_2 structure is also a metastable phase and Mo atoms adopt trigonal prismatic coordination, while every three S–Mo–S units form a crystal cell [15].

MoS_2-nanomaterials have been widely used in a lot of fields, on account of the unique physical and chemical properties, including electronic devices, a transistor, and a catalytic energy storage device [15–17]. In recent years, MoS_2-nanomaterials have attracted more attention in cancer diagnosis and treatment [7]. Firstly, MoS_2 has the large specific surface area and can effectively adsorb various molecules through covalent or non-covalent interactions, such as nucleic acids, proteins, drugs, fluorescent probes, and other molecules, forming MoS_2-nanocomposites with radioactivity, magnetism and imaging, also achieving excellent controlled release by specifically responding to the tumor microenvironment [18]. Secondly, the high absorption rate of MoS_2 in a wide wavelength range promotes its application in phototherapy, including the energy receptor of fluorescence resonance energy transfer, photodynamic therapy agent, and photothermal therapy agent. Meanwhile, a large number of negative charges are distributed on the surface of the MoS_2-nanocomposite, which enables them to be stably dispersed in the aqueous medium without obvious aggregation [19]. Finally, MoS_2 has the advantages of high electron mobility, tunable energy band, photoluminescence, good flexibility, and biocompatibility [14,20–24], which further promote its application in the biomedical field.

However, research MoS_2-nanocomposites in the biomedical field is still at an early stage, especially in terms of diagnosis and treatment of cancer [25]. In this review, we describe the latest developments of MoS_2-nanocomposites in cancer diagnosis and treatment systematically, mainly focusing on bioimaging, chemotherapy, phototherapy, and various combination therapy, with brief introduction of achievements in microwave thermotherapy. Subsequently, we discussed the existing problems and the future foreground of MoS_2-nanocomposites in cancer treatment, providing new ideas for designing nanocomposites to diagnose and treat cancer.

2. Biosensors

The unique microenvironment and abnormal expression of specific biomarkers in cancer cells promote the occurrence and development of cancer. Therefore, accurate, sensitive, and rapid detection of biomarkers is very important for disease diagnosis and treatment [26]. Due to the extremely low concentration of biomarkers, outstanding methods for their detection have attracted a lot of attention [26–28].

As an excellent tool in detection of biomolecules, biosensors have high specificity and sensitivity [29]. The biosensor generally consists of a biorecognition element and a transducer, which can convert the interactions between the biorecognition element and the specific target into an output signal that can be detected and displayed by the processor [30]. However, traditional label-based detection methods have many defects including tedious sample processing, high operation cost, inconvenient portability and limited application in real-time monitoring [31,32]. Label-free biosensors based on nanostructure are superior to the traditional methods in detection speed, sensitivity, cost, and versatility [33]. MoS_2 has the large specific surface area that can cause charge transfer by adsorbing small molecules, resulting in changes in its electron mobility. Meanwhile, MoS_2 is an outstanding energy receptor for quenching fluorescence. Therefore, MoS_2 biosensors can be used as detection devices of biomolecules. In this review, we mainly discuss their application in field-effect transistor sensors, fluorescence resonance energy transfer-based sensors, and electrochemical sensors.

2.1. Field effect transistor (FET) biosensors

FET sensor has advantages of small size, high sensitivity, large detection range and low energy consumption. It has broad application prospects in the detection of cancer markers, especially in the point-of-care testing of cancer markers. FET biosensor is mainly composed of four parts: channel, drain, source and substrate. Among them, the channel is the core part of FET biosensor. FET biosensors can detect the binding events of biomolecules and gate dielectrics or semiconductor channels by monitoring changes in channel conductance [34,35]. The biggest bottleneck of FET biosensors comes from channel materials. The channel materials must be easy to be functionalized with the bioreceptor, and have good semiconductor properties. MoS_2 nanomaterial can be used as a very good channel material of FET biosensors thanks to its unique physical and chemical properties. Controllably switching between the conductive and insulating states of MoS_2 nanostructures can be achieved because MoS_2 has an adjustable bandgap [36]. A larger bandgap provides a better state switching capability, which is very important for isolating any current leakage during device shutdown while improving detection sensitivity and accuracy [37]. MoS_2-based FET biosensors can better control static electricity and reduce low-frequency flicker noise due to interface traps and low surface roughness in its pristine surfaces.

PSA is a biomarker for diagnosing prostate cancer, the second most common cancer among men worldwide [1]. The survival time of prostate cancer patients can be prolonged if it is detected early. Wang et al. [38] designed a label-free FET sensor based on MoS_2 to detect PSA detection, which was the first demonstration and application of the biological functionalization of MoS_2 nanosheet field-effect devices in the liquid phase. The specific binding of PSA with the antibody fixed to the mechanical exfoliated MoS_2 membrane caused a significant change of drain current. The method had high sensitivity, high specificity, and timeliness. However, the mechanical exfoliation method for obtaining single-layer or multi-layer MoS_2-nanomaterials has many limitations, such as long synthesis time, low yield, and batch-to-batch variations [39,40]. Kukkar et al. [41] obtained few-layered MoS_2 nanosheets by electrolytic intercalation of sodium (Na^+) ions into an original molybdenum sheet to produce Mo ions which could combine with S ions. During the process, the raw materials were easy to obtain, and the preparation of few-layered MoS_2 nanosheets was simple, without inorganic or organic byproducts. The MoS_2 nanosheets and anti-PSA antibodies were introduced into FET microdevices for constructing a particular PSA immunosensor that had a wider detection area (10^{-5} to 75 ng/mL). Although many studies have reported the sensitivity and specificity of FET sensors, the repeatability and accuracy have not been explored. Park et al. [42] prepared a MoS_2-based FET in which the 30–45 nm thick MoS_2 flakes had high field-effect mobility (μ = 30–50 $cm^2/(V{\cdot}s)$ on SiO_2/Si substrate), and Al_2O_3 could improve the electrical performance of the device and it was easy to be functionalized by 3-aminoproplytriethoysilane (APTES) and glutaraldehyde (GA). The anti-PSA was fixed to the CHO end of GA via the reaction of lysine and aldehyde. Casein is used as a blocking agent to reduce non-specific molecular binding events in the immune response while uniformly chemisorbed anti-PSA on the surface of MoS_2, which could reliably and quantitatively detect PSA in a non-aqueous environment with excellent accuracy and repeatability (Fig. 2). Most traditional methods of diagnosing PSA are laboratory tests, which are inconvenient and expensive. In contrast, point-of-care (POC) testing has become a trend with the development of biosensors [43]. Yoo et al. [44] designed an epidermal skin-type POC device for real-time monitoring of PSA, which integrated the MoS_2 FET biosensor, readout circuit, along with the light-emitting diode (LED) that as an indicator into a system. PSA antibody could physically absorb on MoS_2 channel by van der Waals force without pre-surface chemical treatment. Meanwhile, the channel conductance of the MoS_2 FET could be affected when anti-PSA combined with PSA. Therefore, highly sensitive detection of PSA could be achieved through the current change of MoS_2 channel. The POC testing device had good electrical performance and mechanical durability under various mechanical stress conditions, and its detection limit (1 pg/mL) was much less than the clinical cut-off.

Recently, Yang et al. [45] prepared a FET sensor based on MoS_2 nanosheets to simultaneously detect the bladder cancer biomarkers (NMP22 and CK8) in patients' urine. The recognition molecules of

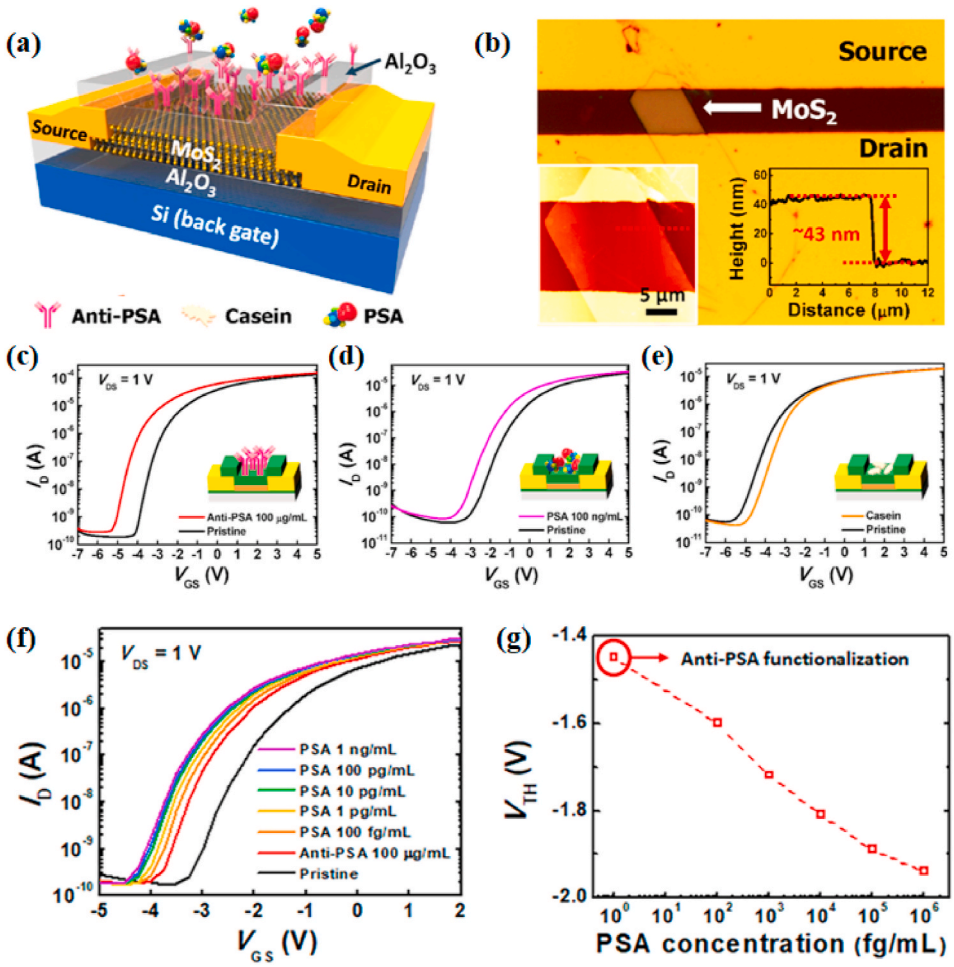

Fig. 2. (a) The pseudo-double-gate structure of a MoS_2 biosensor. **(b)** Optical image of the MoS_2 bio-FET with insets representing a tapping-mode AFM image and its thickness profile. Shifts in the transfer curves for the MoS_2 bio-FET immobilized with **(c)** anti-PSA of 100 μg/mL, **(d)** PSA of 100 ng/mL and, **(e)** casein of 1% (w/v). **(f)** Transfer characteristics with PSA concentrations from 100 fg/mL to 1 ng/mL on the anti-PSA-immobilized MoS_2 bio-FET. **(g)** Plot of V_{TH} against PSA concentrations. Reprinted with permission from Ref. [42]. Copyright 2017, ACS Applied Materials & Interfaces.

NMP22 and CK8 were conjugated on different sensing channels of MoS_2 nanosheets, and the channel current would change and achieve highly sensitive detection of NMP22 and CK8 when NMP22 and CK8 bound to their specific recognition molecules (the detection limits of NMP22 and CK8 as low as 0.027 aM and 0.019 aM, respectively).

2.2. Fluorescent biosensors

The traditional fluorescence methods easily are interfered with background fluorescence, leading to inaccurate detection results [46]. Fluorescence resonance energy transfer (FRET) requires the transfer of energy from donor to the recipient to sensitively detect biomolecules [47]. Fluorescence sensors based on nanomaterials can overcome the shortcomings of traditional fluorescence methods and selectively combine with target substances to ensure a high labeling success rate, obtain strong fluorescence detection signals, facilitate detection equipment to capture signals, and significantly improve detection sensitivity and reliability. MoS_2 has been regarded as an effective energy receptor for quenching fluorescence, on account of its high surface area and particular optical characteristics [48]. Meanwhile, MoS_2 is suitable for intracellular analysis due to its low cytotoxicity [49].

miRNAs play important roles in molecular pathways and are promising molecular biological markers to predict the early tumorigenesis or metastasis [50]. Currently, miRNAs are mainly detected by end-point technologies, including northern blotting, qualitative reverse transcription-polymerase chain reaction (qRT-PCR) [51], Northern blotting [52], and microarrays [53], which require a good deal of samples simultaneously take a long time. MoS_2 nanomaterial-based fluorescent biosensors can overcome the above defects and improve detection sensitivity and specificity [54,55]. Xiao et al. [56] found that polycytosine (polyC) DNA could non-covalently functionalize MoS_2 nanosheets to retain DNA activity and increase the recognition ability of probes. They synthesized diblock molecular beacons that possessed polyC tails attached to MoS_2 nanosheets to detect miRNA. During co-incubation with layered MoS_2, the van der Waals force make the polyC-MB adsorbed on MoS_2 [57], and then the fluorescence of the dye is quenched by FRET [58]. DNA/RNA heteroduplex could be formed with the target miRNA because of the specific affinity between MB block and miRNA, while the duplex-specific nuclease (DSN) would cleave it, leading to fluorescence recovery. Furthermore, DNS could cause signal amplification by target recirculation. Considering that the extracellular detection of miRNA is complicated and time-consuming, Oudeng et al. [59] prepared the folic acid (FA)-poly (ethyleneglycol)-modificatory MoS_2 nanosheets and used fluorescent-labeled ssDNA probes to fix it (ssDNA-MoS_2-PEG-FA) for the first time, realizing one-step in-situ to detect endogenous miRNAs in the single cancer cell. After the cancer cells internalized the ssDNA-MoS_2-PEG-FA, the high binding force of miRNA-21 and ssDNA made the probe fall off from the MoS_2 nanosheet, resulting in the rapid fluorescence recovery (Fig. 3 a, b). Nevertheless, there are many challenges in intracellular detection due to the high homology, small size and low abundance of miRNAs. For example, the signals read by a single step of in situ hybridization are relatively low and the sensitivity of miRNA detection is limited [59]. Besides, false-positive signals may be caused by the complex intracellular environment, nuclease degradation, or non-specific binding. A living cell detection strategy related to isothermal amplification and enzyme-catalyzed cycling reaction can increase the sensitivity of the intracellular analysis [60,61]. To this end, Zhu et al. [62] used the DNA

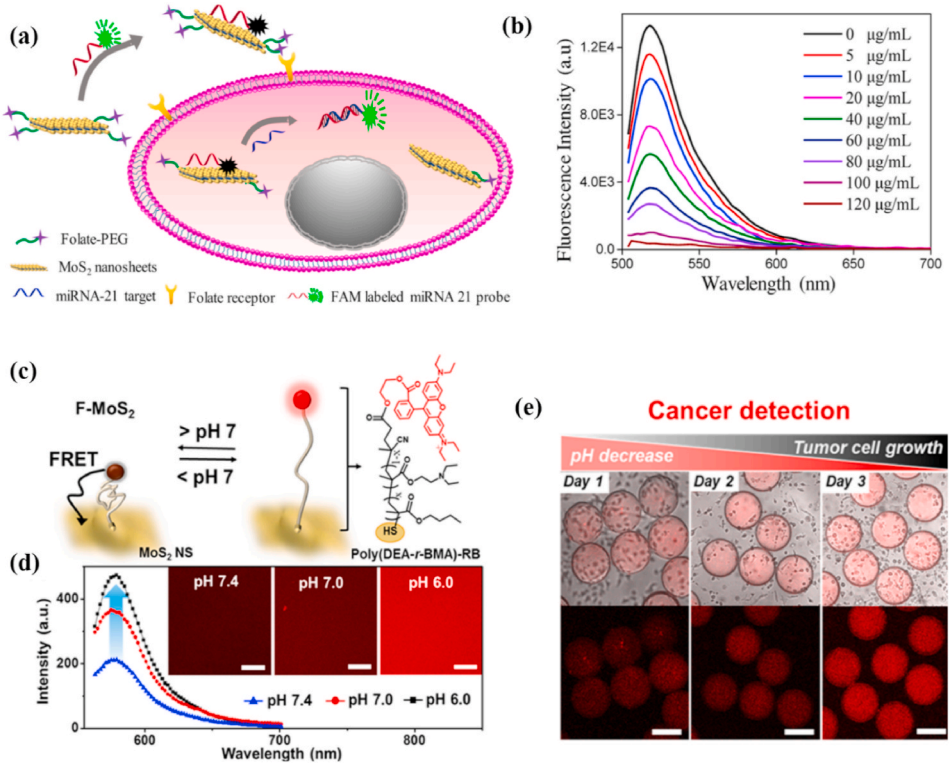

Fig. 3. (a) Schematic of ssDNA-MoS_2-PEG-FA probe-based FRET platform for intracellular miRNA-21 detection. **(b)** Photoluminescence spectra of FAM-labeled miRNA-21 probes incubated with MoS_2 nanosheets with a series of concentrations. Reprinted with permission from Ref. [59]. Copyright 2018, ACS Applied Materials & Interfaces. **(c)** Schematic illustration showing the construction of the F–MoS_2 NSs and pH-dependent FRET, which is mediated by a conformation change of poly (DEA-r-BMA). **(d)** PL spectra of F–MoS_2 NSs at three different pH values of 7.4, 7.0, and 6.0. Insets are the corresponding confocal microscopy images of the solution. Scale bars are 100 μm. **(e)** Series of overlaid bright-field and fluorescence confocal microscopy images (top) and confocal microscopy images (bottom) showing the progressive enhancement of fluorescence intensity in the microcapsules during the growth of A549 tumor cells. Scale bars are 200 μm. Reprinted with permission from Ref. [63]. Copyright 2018, ACS Applied Materials & Interfaces.

catalytic hairpin supported by MoS_2 as a signal amplifier to detect the low expression of miRNA-21 in living cells. Three kinds of DNA molecular beacons modified with Cy3 in the terminal consist of the three-branched catalyzed hairpin assembly (TB-CHA) probes that form "Y"-shaped three-branched duplex nanostructure when miRNA-21 is presented, releasing from the surface of the MoS_2 nanosheet. In the microenvironment of living cells, multi-site fluorescence modification and cyclic reaction enable TB-CHA probe to achieve significant fluorescence recovery.

Cancer cells secrete lactic acid to maintain their weakly acidic microenvironment (pH 6–7). Therefore, tumor sites can be confirmed by pH [64]. Detecting the regional pH of the tumor microenvironment via traditional ways (e.g., a pH meter or litmus test paper) is difficult because of its limited accessibility. pH-responsive polymers [65] with good biocompatibility can link the fluorescent molecules and optical quenchers to produce pH-dependent FRET compounds [66,67]. The MoS_2 nanosheets have a large specific surface area and abundant sulfur binding sites, thus the oligomeric or polymeric molecules can briefly functionalize them under mild conditions [68,69]. Park et al. [63] synthesized a FRET-based microsensor and encapsulated it in a microcapsule by attaching a pH-responsive polymer that contain a fluorescent terminal to the surface of a MoS_2 nanosheet (F–MoS_2 NSs). The pH-sensitive polymer could respond to subtle pH changes through conformational changes and converted it into FRET signals at a lower pH for detecting cancer cells. The microcapsules ensured that MoS_2 NSs did not leak while preventing the entry of adhesion proteins and lipids, avoiding the inactivation of encapsulated MoS_2 NSs, meanwhile realizing home position pH monitoring (Fig. 3 c-e).

EpCAM protein can be applied as a biomarker for cancer diagnosis, treatment, and prognosis because its overexpression was found in most cancer [70–72]. The majority of EpCAM-based diagnoses and treatments depend on anti-EpCAM antibodies, which cannot supply accurate clinical outcomes due to their instability and large-size under the physiological condition [73,74]. Aptamers, with small size and high specificity towards biomolecules, have been widely used in the sensor field [75]. On the other hand, Graphene quantum dots (GQDs) can serve as good FRET donors to detect specific biomarkers because of their high light stability [76]. Meanwhile, MoS_2 has a good light absorption capacity at a wide wavelength range and can be used as an efficient energy acceptor. For these reasons, Shi et al. [77] designed a novel GQD-PEG-aptamer/MoS_2 "turn-on" fluorescent biosensors based FRET mechanism for the rapid and sensitive detection of EpCAM. Since EpCAM aptamer and the EpCAM protein have a stronger affinity, the separation of MoS_2 nanosheet and GQD-PEG-EpCAM aptamer could be promoted in the existence of EpCAM proteins, causing the restoration of fluorescence intensity. The biosensor could sensitively and selectively detect EpCAM in the detection range of 3 nM–54 nM, with a low detection limit (450 pM).

Recently, Xu et al. [78] synthesized silver nanocluster (AgNC) @ MoS_2 to detect ATP in Hela cells. ATP aptamer was as templates to prepare DNA-AgNCs, which was as a fluorescent label and an Ag element tag to quantitatively analyze ATP. In addition, DNA-AgNC was loaded on MoS_2 nanosheets by van der Waals forces, and its fluorescence was quenched by MoS_2 nanosheets. The interaction between DNA-AgNCs and MoS_2 nanosheets could be weakened when ATP specifically bound to its aptamer. As a result, DNA-AgNC was released from the surface of MoS_2 nanosheets, and its fluorescence was recovered. The detection limits of this nanoplatform as low as 0.18 nmol/L. Similarly, Zhao et al. [79] used fluorescein (FAM) labeled DNA to functionalize MoS_2 for detecting CA15-3. The fluorescence of FAM-DNA was quenched by MoS_2 via FRET and was restored when CA15-3 bound to FAM-DNA. The fluorescent biosensor not only had a low detection limit (0.0039 U/mL) but also displayed high sensitivity.

2.3. Electrochemical biosensors

The electrochemical biosensor converts the interaction of biomarkers and bioreceptors into electrical signals, which has many advantages such as simple preparation, low cost, simple operation, fast speed, good stability, strong specificity, high sensitivity. The introduction of nanomaterials in electrochemical biosensor systems can further enhance the detection signal, improve detection specificity and

accuracy, and has been widely used in the biomedical field. As a semiconductor that possesses an indirect energy band of 1.29 eV, MoS_2 has good electrocatalytic activity due to the enhancement of planar electrical transmission performance [80]. Furthermore, MoS_2 modified by monometallic, bimetallic or even trimetallic nanoparticles exhibits higher catalytic performance [81,82]. Currently, the MoS_2-based electrochemical sensors have detected multiple tumor markers, such as H_2O_2, carcinoembryonic antigen (CEA), circulating tumor cells (CTCs) and miRNA.

MoS_2-based nanocomposites can electrochemically catalyze the reduction of H_2O_2 to produce H_2O and O_2, detecting H_2O_2 via the current change induced by redox reaction [83]. In situ detecting H_2O_2 secreted by cells is extremely significance because the intracellular H_2O_2 concentration level is a key physiological parameter for early screening and diagnosis of primary cancer [84]. Electrochemical methods can be utilized for detecting H_2O_2 secreted from living cells because they can offer an interface to bridge cells and sensing electrodes [85]. However, electrochemical sensors currently used for in situ detecting H_2O_2 not only require complicated manufacturing processes but also are not feasible for cell adhesion and growth. Dou et al. [86] synthesized Au–Pd–Pt nanoflower-modified MoS_2 nanosheet-based sensor through a wet chemical method to in-situ monitor the secretion of H_2O_2 that from living MCF-7 cancer cells, which enhanced the electrochemical catalytic activity through synergistic action of the MoS_2 nanosheets and the highly dispersed tri-metal hybrid nanoflower, and improved the biocompatibility of cell adhesion and growth by immobilizing laminins on the surface of nanocomplexes. Although loading noble metals on MoS_2 can improve detection sensitivity, it would decrease stability and increase costs. Interlayer expanded MoS_2 (IE-MoS_2) without noble metal nanoparticles can also provide high sensitivity, clarity, and resolution for H_2O_2 detection. Shu et al. [87] used excessive thiourea to synthesize IE-MoS_2 with a wide interlayer spacing of 9.40 Å via the one-step hydrothermal reaction with good electrical conductivity and strong combining ability with *OH intermediates, realizing the rapid kinetics reduction of H_2O_2 ($H_2O_2 + 2e^- \rightarrow 2OH^-$). The sensitivity of the first-rank IE-MoS_2 is considerably high (1706.0 μA/(mM·cm^2)), while the detection limit is very low (0.2 μM). Thanks to Mo_2C advantages of high conductivity, Mo_2C@MoS_2 co-axial nanorods had a higher sensitivity of H_2O_2 (1080 μA/(mM·cm^2)) and lower detection limit (0.2 μM) than IE-MoS_2. At the same time, Mo_2C@MoS_2 had rich surface amino groups, and could be used to specifically detect MDA-MB-231 cells after functionalized folate ligand [88]. Besides, studies found that self-supporting nanoarrays with a three-dimensional (3D) structure could further enhance the sensitivity of H_2O_2 detection because they had more catalytic sites and larger contact areas than the two-dimensional electrode [89]. Du et al. [90] designed a MoS_2 nanosheet array that distributed over the carbon cloth (MoS_2/CC) for ultrasensitive detection of trace amounts of H_2O_2 secreted by living cells. MoS_2/CC with low charge transfer resistance and abundant surface area as a good electron conductor facilitated the electron transfer from the MoS_2/CC electrode to reduce H_2O_2, which led to significant current changes to sensitively detect the concentration of H_2O_2. As a result, MoS_2/CC afforded an outstanding sensitivity of 5300 μA/(mM·cm^2). Recently, Yang et al. [91] prepared 3D MoS_2/reduced graphene oxide composite (3D-MoS_2/rGO) as a sensitive sensor of H_2O_2. Graphene could not only serve as the supporting structure for the growth of MoS_2 but also increase the specific surface area of MoS_2/rGO to promote reaction with H_2O_2. The 3D-MoS_2/rGO sensor had a good anti-interference ability, a lower detection limit (0.19 μM), and a wider linear range (2 μM–23.18 mM).

CEA (tumor-associated glycoprotein) is a crucial marker to detect multiple tumors but its concentration is ultralow in the early stages of cancer. Hence, in order to early diagnosis cancer, high sensitivity detection of CEA is very vital. MoS_2 can easily modify with specific antibodies to prepare highly sensitive electrochemical sensors to detect tumor-specific antigens. Wang et al. [92] integrated MoS_2–Au with strong catalytic activity and Ag nanospheres (AgNPs) with good electricity into an electrochemical immunosensor for detecting CEA. MoS_2–Au used as the solid support for CEA primary antibody (Ab_1) and AgNPs were served as the supporter of glucose oxidase (GOx) and CEA secondary antibody (Ab_2), which could combine with CEA respectively to form a sandwich-type immunosensor. The H_2O_2 was produced after glucose was added and MoS_2–Au could catalyze reduction of H_2O_2 to cause the current to vary with the concentration of CEA. The biosensor had a range of linearity from 1 pg/mL to 50 ng/mL and a limit of detection of 0.27 pg/mL. Analogously, Ma et al. [93] also synthesized a sandwich-type electrochemical immunosensor with a broader detecting range (10 fg/mL to 100 ng/mL) and a lower limit of detection (3.09 fg/mL). The trimetallic yolk-shell Au@AgPt nanocubes (Au@AgPt YNCs) with good catalytic activity loaded on amino-modified MoS_2 nanoflowers to form MoS_2 NFs/Au@AgPt YNCs as the marker of Ab_2, which could catalyze the reduction of H_2O_2 more effectively and thus amplify the current signal. At the same time, gold triangle nanoprisms (Au TNPs) as substrate materials offered a steady environment for immunosensors. The reduction reaction of H_2O_2 was triggered to realize the detection of CEA concentration when CEA was combined with Au TNPs and MoS_2 NFs/Au@AgPt YNCs respectively. Jia et al. [94] used MoS_2/CuS–Au as sensing platform and Au@PtPd porous nanorods (Au@PtPd MP-Ab_1) as signal amplifiers to fabricate sandwich-type biosensor for detecting CEA. MoS_2/CuS–Au could increase the loading rate of Ab_1 and the electron transport rate. Au@PtPd MP-Ab_1 had excellent catalytic activity and could generate highly sensitive current signal, which could efficiently detect CEA in human serum samples. Despite tremendous progress of electrochemical immunosensors have been achieved, ultra-sensitive high-performance immunosensors with multiple amplified signals are still challenging [95]. In order to further improve their detection performance and amplify detection signal of CEA, the reducing substrate (o-phenylenediamine[o-PD], Cu_2O, and Ferrocene[Fc]) and enzyme amplifiers were introduced into the detection system of MoS_2 and H_2O_2 [96–99]. Su et al. [100] used MoS_2 nanocomposites (MoS_2-AuNPs) decorated with gold nanoparticles to construct an enzyme-assisted signal amplification sensor for CEA analysis. MoS_2-AuNPs could load anti-CEA (Ab_1) after being modified onto the cleaned glassy carbon electrode (GCE) to form anti--CEA/MoS_2-AuNPs/GCE. Meanwhile, HRP-anti-CEA (Ab_2) was loaded on the surface of MoS_2-AuNPs to produce HRP-anti-CEA/MoS_2-AuNPs nanoprobe for blocking the nonspecific absorption. The effective amplification of the electrochemical signal is attributed to the following three strategies. Firstly, MoS_2-AuNPs catalyze the reduction of H_2O_2 to produce *OH intermediates which could oxidize o-PD to form o-PDox, amplifying the changes of current response signal. Second, the HRP-anti-CEA could also generate the above reaction to further amplify the current change. Third, the introduction of HRP could not only prevent non-specific adsorption but also catalyze the redox reaction of H_2O_2 and o-PD to enhance the electrochemical properties of the sensor. Such immunosensor has a lower limit of detection of 1.2 fg/mL.

CTCs, are the malignant cells found in biological fluids and indicate the invasion and metastasis of tumor, which ultimately lead to the death of the patient [101,102]. At present, multifarious methods have been used to capture and detect CTCs, such as immunomagnetic separation [103], microfluidic chip [104], as well as flow cytometry [105]. Nevertheless, majority of methods are complicated to operate or require expensive instruments [106–108]. Label-free detection of CTCs by electrochemical methods will greatly simplify analytical techniques and accelerate the capture of CTCs [109,110]. MoS_2 is a semiconductor that possesses good electrical conductivity and easily functionalized surface, and it is thus a very suitable candidate for electrodes. Chen et al. [111] constructed MoS_2/FA-modified AuE (AuE/MoS_2/FA) by using folic acid-modified two-dimensional MoS_2 (MoS_2/FA) as a signal indicator and assembling it on the surface of the gold electrode (AuE), which could detect CTCs by an alternating current (AC) impedimetric method. Since the conductivity of MoS_2 (0.14 S/m) and cancer cells (0.13–0.23 S/m) is approximate, the sensitivity of the MoS_2 electrochemical sensor

may be enhanced after adding cancer cells. This is because that an insignificant change in the conductivity caused by cancer cells causes a conspicuous change in the impedance of the semiconductor electrode. Meanwhile, MoS_2/FA with a high specific surface area might increase the contact sites between semiconductor and CTCs, further improving the sensitivity. Besides, the FA loaded on 2D MoS_2 could specifically recognize HeLa cells that is enrichment of folate receptor (FR), significantly increasing the impedance even in the presence of a few HeLa cells, because MoS_2 is loaded with a lot of FA. Therefore, the prepared electrochemical sensor could detect cancer cells in a linear range of 1 to 10^5 cell/mL, and the limit of detection is 0.43 cell/mL (S/N = 3) (Fig. 4).

However, the captured CTCs were incapable of effectively releasing, greatly hindering the further proliferation and downstream biomedical applications of cells [112]. It is known that most of the current cell release strategies based on enzymes or other chemical methods would seriously damage cells, reduce cell viability and affect analysis results [106,107]. Light-induced cell release has highly precise controllability [108]. MoS_2 nanosheets (NFs) can be used as the NIR-regulated control element to effectively release CTCs. Wang et al. [113] designed a NIR optical switch biological platform to capture, detect, and release CTCs. Firstly, the surface of ITO was modified with PEG-MoS_2 NFs@ gelatin as the working electrode. The MUC1 aptamer is then fixed to its surface by amination between the aptamer and gelatin. Thus, it could specifically bind to the MUC1 protein overexpressed on the membrane of MCF-7. The rapid electron transfer between the nanoplatform and the redox probe could result in a significant change of impedance when cancer cells were added, which was attributed to the quite high conductivity of MoS_2 NFs. Meanwhile, MoS_2 with strong photothermal ability could make the NIR-light transform into heat that would melt the solid gelatine, releasing cancer cells. Notably, the nanoplatform had a remarkable release efficiency of 92.5% and the released cells remained in good cellular shape and proliferative ability.

In addition, electrochemical sensors based on MoS_2 can also sensitively detect miRNA, triiodothyronine, cytokeratin 19 fragment antigen 21-1, EpCAM, and α-methylacyl-CoA racemase [114–119]. These probes were prepared by functionally modifying specifical ligands at the MoS_2-based nanocomposites. The current or impedance of the probes would change when the target substances and the ligands on the probe surface specifically interacted. In this way, highly sensitive detection of target substances could be achieved. For example, Su et al. [120] prepared highly sensitive miRNA-21 probe (MLNP)by functionally modifying specific DNA (specifically binds to miRNA-21) on MoS_2–AuNPs. In the presence of miRNA-21, MLNPs formed a typical "sandwich" structure to cause changes of impedance. The miRNA-21 detection limit of the probe was as low as 38 aM and the detection range was as wide as 10 aM - 1 μm.

2.4. Other biosensors

Surface-enhanced Raman scattering (SERS) overcomes the inherent limitations of traditional Raman spectroscopy and improves its sensitivity by SERS substates [121]. SERS substrates are dependent on plasmonic effects in electromagnetic "hotspots" and highly concentrated charges originating from surface roughness [122]. SERS biosensors have obvious advantages, such as fingerprint recognition and single-molecule sensitivity. Recently, MoS_2 were prepare MoS_2/precious metal nanocomposites to fabricate highly sensitive SERS substrates [123]. For example, Liu et al. [123] designed Ti_3C_2 (MXene)/MoS_2@ Au nanoparticles (AuNPs) (MMA) to detect miRNA-182. AuNPs not only were used to enhanced the signal of SERS, but also could graft the hairpin probe DNA labeled with Cyanine 5 (Cy5) via Au–S bonds. Cy5 were released from the MoS_2 nanocomposites when the probe DNA bound with miRNA-182, and then reduced the intensity of the SERS peak at 1362 cm^{-1}. In this way, miRNA-182 could be detected with high sensitivity and the detection limit of miRNA-182 was 6.61 aM.

MoS_2 nanomaterials usually have weak peroxidase activity. Recently, Sun et al. [124] found that the peroxidase activity of MoS_2 could be greatly increased by modifying MoS_2 with gold nanoparticles. On this basis, the MoS_2/Au could catalyze H_2O_2 to generate *OH with strong oxidizing properties that could oxidize 3,30,5,50-tetramethylbenzidine (TMB) to the colorimetric assay of H_2O_2. Electrochemiluminescence (ECL) has many advantages, such as low background, high sensitivity, simple operation, good controllability. Recently, MoS_2 nanocomposites also have been used in ECL biosensors

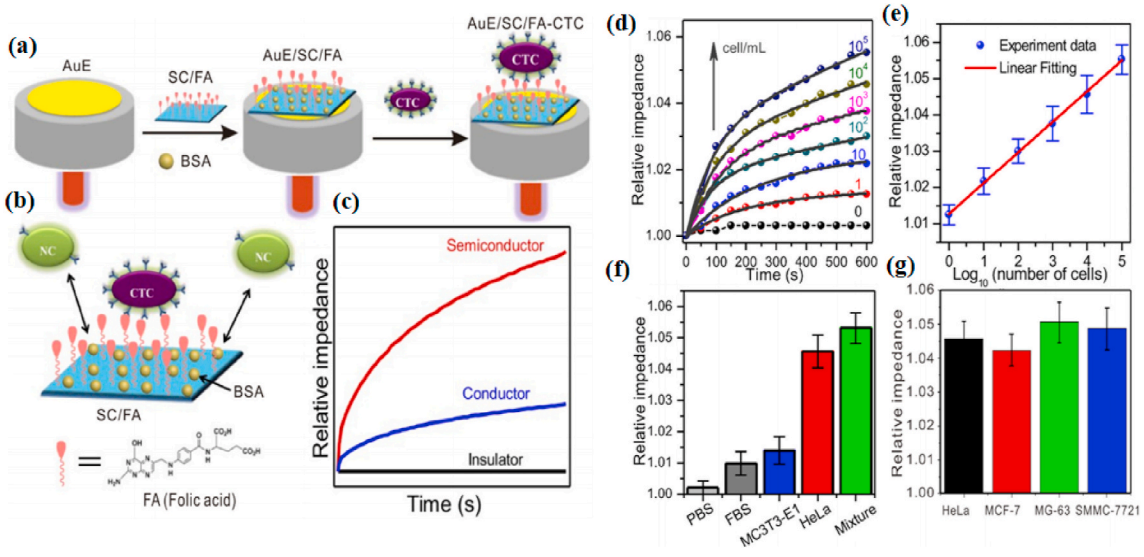

Fig. 4. (a) The fabrication of AuE/SC/FA for CTC capture. **(b)** Schematic model of HeLa cell binding with FA and repelling NC on a negatively charged AuE/SC/FA electrode surface. **(c)** The corresponding impedance curves. SC: Semiconductor; AuE: gold electrode; BSA: albumin from bovine serum; CTC: circulating tumor cells; FA: folic acid; NC: normal cells with low folic receptor expression. **(d)** Relative impedance at 10 Hz with time for AuE/MoS_2/FA electrodes scanned while being immersed in HeLa cell with different concentrations in PBS. The grey solid lines indicate fittings using exponential association. **(e)** Calibration plots of relative impedance at 10 min for determining HeLa cells at AuE/MoS_2/FA electrodes while changing the concentration of HeLa cell in PBS. **(f)** Relative impedance at 10 min at AuE/MoS_2/FA electrodes for PBS, 10% FBS solution, MC3T3-E1 cell suspension, HeLa cell suspension and the mixture of all, indicating a good selectivity of AuE/MoS_2/FA electrodes. **(g)** Relative impedance at 10 min at AuE/MoS_2/FA electrodes for HeLa, MCF-7, MG-63 and SMMC-7721 cancer cell suspensions. Three replicates were performed. Reprinted with permission from Ref. [111]. Copyright 2019, Biosensors & Bioelectronics.

due to their strong fluoresce quenching ability and electrocatalytic performance [125,126]. For example, Delnia Bahari et al. [127] prepared MoS_2 based electrochemiluminescence sensor (GO-HBP-Ru-complex-NCND-anti-CA19-9 Ab_1) to detect carbohydrate antigen 19-9 (CA19-9). In this sensor, amine-rich nitrogen-doped carbon nanodots (NCNDs) linked to $Ru(bpy)_2(phen\text{-}NH2)^{2+}$ was loaded on graphene oxide grafted hyperbranched aromatic polyamide (GO-HBP) to generate and amply the ECL signal, and MoS_2 was used as a strong quencher. The sandwich complex of GO-HBP and MoS_2 would be formed and cause ECL signal quenching via FRET effects when CA19-9 antigen and MoS_2-Ab_2 were added.

3. Bioimaging

Early biological behavior analysis and high-precision positioning of tumors improve the accuracy of tumor qualitative, tumor staging and curative effect analysis. Therefore, high-precision imagological examinations play an increasingly important role during the treatment process to achieve personalized medicine, optimize treatment effect, and monitor the treatment response [128–132]. The common tumor imaging method is fluorescence (FL) imaging which has good selectivity, fast response, high resolution that can observe subcellular structures and realize real-time imaging. For example, Zhang et al. [133] fabricated poly(N-isopropylacrylamide) (PNIPAM)-peptide-Au nanospheres with red fluorescence for observing its endocytosis pathway in HeLa cells. FL imaging usually obtained under ultraviolet rays or visible light irradiation, but hemoglobin and other biomolecules have strong absorption of visible light and ultraviolet rays, leading to a weaker penetration depth of FL imaging. Most tumors are located inside the body that requires imaging methods have longer penetration depth and high resolution, implying that common FL is not very suitable for deep tumor imaging.

Currently, there are many imaging methods used to overcome the above difficulties. These methods are mainly divided into three categories: The first category mainly uses near-infrared light as the excitation light source or detection signal, including near-infrared fluorescence imaging (NIRF), two-photon imaging (TPF), and photoacoustic imaging (PA); The second category is to use ultra-short wavelength, high-energy rays as the excitation light source or detection signal, including positron emission tomography (PET, γ-photons) and X-ray computed tomography (CT, X-ray); The third category is the use of ultra-long wavelength electromagnetic waves as the excitation light source (such as MRI). The penetration depth of these imaging is longer than common FL imaging (Table 1). MoS_2 has various physicochemical properties (such as strong near-infrared absorption and easy functional modification), which enables it to be combined with other materials to fabrication powerful imaging platforms. MoS_2 nanocomposites have aroused great concern from scientific researchers in recent years (Table 2). In this part, we will introduce the NIRF imaging, PA imaging, CT imaging, PET imaging and MRI based on MoS_2 nanomaterials according to the penetration depth from shallow to deep.

Table 1
Principle and depth of imaging detection.

Imaging modality	Incident radio	Detection signal	Depth	Resolution
Common FL imaging	350–650 nm	Vis	~1 mm	0.2–0.4 μm
NIRF imaging	650–900 nm	NIR	~6 mm	0.35–0.5 μm
TPF imaging	1000–1700 nm	Vis-NIR	~7 mm	0.3~1 μm
PA imaging	650–950 nm	Ultrasonic	~50 mm	20–300 μm
CT imaging	0.01 nm–10 nm	X-rays	No limit	50–500 μm
PET imaging	~0.002 nm (511 KeV)	γ-photons	No limit	2~7 mm
MR imaging	~7 m (42.6 MHz)	Radio wave	No limit	25–100 μm

3.1. FL imaging

Near-infrared light can be divided into two areas: the first area (NIR-1, 650–900 nm) and the second part (NIR-2, 1000–1700 nm). NIR-1 and NIR-2 both have a longer penetration depth in the body than visible light because biological tissues have a low absorption for them [134–136], indicating that NIR-1 and NIR-2 are biological transparent windows. Meanwhile, the normal biological tissues hardly get damage and not emit light (without background fluorescence) when exposed to the NIR light. Once special nanomaterials absorb NIR light and then transform into required signal or energy at tumor site, good contrast imaging of tumor can be achieved by NIR light irradiation, as shown in Fig. 5. These advantages have made NIRF imaging widely used in cancer imaging in recent years.

NIRF imaging is a novel in vivo imaging method with low background signal, high resolution, and high stability. Zero-dimensional (0D) semiconductor nanocrystals, commonly called quantum dots (QDs), have a variety of special optical characters, including wide excitation and narrow emission spectra, strong fluorescence, and high photobleach resistance [137]. Therefore, QDs have become a fluorescent labels for biomedical imaging [138]. Nevertheless, it is difficult to prepare multifunctional MoS_2 nanoplatform with excellent luminescence due to the strong quenching effect when QDs directly bind with MoS_2. Zhang et al. [139] prepared RGD-QD-MoS_2 nanosheets (NSs) that could successfully be used for targeted fluorescence imaging under NIR (785 nm) laser. MoS_2 NSs adsorbed BSA (bovine serum albumin) on its surface by the van der Waals force, and BSA was conjugated QDs (CdSSe/ZnS, 580 nm) by forming amide bonds. Subsequently, RGD (arginine-glycine-aspartic) with outstanding tumor-targeting capability combined with the carboxyl-activated QDs to obtain RGD-QD-MoS_2 NSs. BSA not only acted as an anchor to conjugate QDs but also decreased the fluorescence quenching of QDs by broadening the distance between QDs and MoS_2 NSs. Meanwhile, MoS_2 NFs with lots of defect sites could be efficiently modified with thiolated PEG to enhance their colloidal stability. Compared with QD-MoS_2 NSs (without RGD), RGD-QD-MoS_2 NSs could specifically combine with integrin αvβ3 that is highly expressed on HeLa cells membrane, which is beneficial to produce a stronger fluorescence signal on the HeLa cell membrane and in the tumor areas of HeLa tumor-bearing Balb/c nude mice when treated with RGD-QD-MoS_2 NSs (Fig. 6 a-d).

MoS_2 must be modified by NIR fluorescent substance to obtain the function of NIRF imaging because themselves cannot emit NIR light [142,143], which requires careful design and complex synthesis process. The TPF excitation is a kind of fluorescence process, in which simultaneously absorb two photons to excite the fluorophore. The excitation light source of TPF usually is near-infrared laser which can emit fluorimetry under the visible light region. Compared with traditional fluorescence (SPF) imaging technology, TPF imaging technology has deeper tissue penetration, lower tissue autofluorescence and less photobleaching [144,145]. Monolayer MoS_2 has great photoluminescence because of their indirect-direct band gap transition, but its applications in TPF imaging are rare due to its extremely low room-temperature TPF quantum yield (QY) ($\Phi \approx 1\%$) [146–151]. Different from monolayer MoS_2, MoS_2 quantum dots (QDs, their size are below 10 nm) have unique optical and electrical properties that attributed to the size and quantum confinement effect [152,153]. MoS_2 QDs have a higher two-photon absorption cross-section than organic dyes and common semiconductor QDs, representing it can be applied to TPF imaging [154]. Dai et al. [140] fabricated controllable-size MoS_2 QDs which had high TPF QY ($\Phi = 9.65\%$), long fluorescence lifetime (4.66 ns), and favourable fluorescent stability in the pH range of 4–10. The bright blue fluorescence could be observed in HeLa cell treated by MoS_2 QDs when irradiated by NIR-1 (700 nm) and the fluorescence brightness had not changed significantly after continuous excitation 30 min, indicating that

Table 2
MoS_2-based nanocomposites for cancer imaging and therapy.

Materials	Physically trigger	Therapy	Imaging modes	In vivo models	Therapeutic effect	Refs
DOX-MoS_2/Pt	/	drug delivery	/	/	/	[378]
DOX-PSMS-PEG	NIR laser(808 nm)	drug delivery	/	/	/	[206]
DOX/DNA/MoS_2-NS	ATP	drug delivery	/	/	/	[379]
MoS_2/GO@DOX	GO-targeting	drug delivery	/	Mice bearing B16 tumor	Completely eradicate tumor	[213]
DOX@MoS_2-PEI-HA	NIR laser(808 nm)/pH/HAase	drug delivery	PET	Mice bearing MCF-7-ADR tumor	Completely eradicate tumor	[181]
F–MoS_2 NSs.	NIR laser(808 nm)	PTT	/	/	/	[63]
MoS_2-CS-Cype	NIR laser(808 nm)	PTT	/	/	/	[380]
MoS_2-PEG nanoflakes	NIR laser(808 nm)	PTT	/	Mice bearing 4T1 tumor	/	[244]
MoS_2-PEG	NIR laser(808 nm)	PTT	/	Mice bearing 4T1 tumor	Delay tumor growth	[240]
MoS_2-PPEG	NIR laser(808 nm)	PTT	/	Mice bearing 4T1 tumor	Reduce tumor volume	[258]
MoS_2-GSH nanodots	NIR laser(808 nm)	PTT	PA	Mice bearing 4T1 tumor	Completely eradicate tumor	[252]
RGD-QD-MoS_2 NSs	NIR laser(785 nm)	PTT	NIRF	Mice bearing HeLa tumor	Reduce tumor volume	[][][]139]
MoS_2@PZAC	NIR laser(808 nm)	PTT	MRI	Mice bearing 4T1 tumor	Reduce tumor volume	[178]
MoS_2-Gd-BSA	NIR laser(808 nm)	PTT	MR/PA	Mice bearing 4T1 tumor	Completely eradicate tumor	[305]
Layered MoS_2 hollow spheres	NIR laser(808 nm)	PTT	CT/IR	Rabbit bearing VX2 tumor	Completely eradicate tumor	[242]
HA-MoS_2	NIR laser(808 nm)	PTT	FL/PA	Mice bearing HCT116 tumor	Reduce tumor volume	[293]
^{64}Cu-MoS_2-IO-(d)PEG	NIR laser(808 nm)	PTT	MRI/PA/PET	Mice bearing 4T1 tumor	Reduce tumor volume	[177]
p-MoS_2/n-rGO-MnO_2-PEG	NIR laser(980 nm)	PDT	/	/	/	[262]
MoS_2-PEG/Ce6	NIR laser(808 nm)/660 nm	PTT/PDT	/	Mice bearing 4T1 tumor	Delay tumor growth	[269]
MoS_2-LA-K11(DMA)-TBO (MKT)	NIR laser(808 nm)/630 nm	PTT/PDT	/	Mice bearing SCC-7 tumor	Reduce tumor volume	[270]
MoS_2-UCNPs-FA/ZnPc	NIR laser(808 nm)/980 nm	PTT/PDT	NIRF	Mice bearing HCC38 tumor	Delay tumor growth	[289]
PEG-MoS_2-Au-Ce6	NIR laser(808 nm)/660 nm	PTT/PDT	CT/NIRF	Mice bearing 4T1 tumor	Reduce tumor volume	[381]
Cy5.5-BSA-MoS_2	NIR laser(808 nm)	PTT/PDT	FL/PAT	Mice bearing HepG2 tumor	Completely eradicate tumor	[292]
MoS_2-UCNPs@Ce6@SiO_2	NIR laser(808 nm)	PTT/PDT	CT/MRI/UCL	Mice bearing U14 tumor	Reduce tumor volume	[382]
BSA-MoS_2	MW irradiation	MW thermal therapy	/	Mice bearing H22 tumor models	Completely eradicate tumor	[279]
MoS_2 encapsulated in microcapsules	MW irradiation	MW thermal therapy	CT	Rabbit bearing VX2 tumor	Completely eradicate tumor	[280]
sandwich-like MoS_2@MOS	NIR laser(808 nm)	PTT/drug delivery	/	/	/	[334]
Fe_3O_4@MoS_2@ZnO-DOX	NIR laser(808 nm)	PTT/drug delivery	/	/	/	[320]
HMSNs/DOX@MoS_2/Tf	NIR laser(808 nm)	PTT/drug delivery	/	/	/	[207]
Mn-doped Fe_3O_4@MoS_2	NIR laser(808 nm)	PTT/drug delivery	MRI	/	/	[307]
PMO-DOX@MoS_2-PEG	NIR laser(808 nm)	PTT/drug delivery	/	Mice bearing MCF-7 tumor	Delay tumor growth	[322]
MoS_2-HPG-DOX	NIR laser(808 nm)	PTT/drug delivery	/	Mice bearing B16 tumor	Delay tumor growth	[325]
MoS_2-PEG-FA/DOX	NIR laser(808 nm)	PTT/drug delivery	/	Mice bearing 4T1 tumor	Delay tumor growth	[68]
MoS_2/HSA-DOX	NIR laser(808 nm)	PTT/drug delivery	/	Mice bearing MCF-7 tumor	Completely eradicate tumor	[328]
HA-PEI-LA-MoS_2-PEG@(DOX/Mel)	NIR laser(808 nm)/pH	PTT/drug delivery	/	Mice bearing MCF-7 tumor	Reduce tumor volume	[314]
MoS_2-Lipid-DOX	NIR laser(808 nm)/pH	PTT/drug delivery	/	Mice bearing 4T1tumor	Reduce tumor volume	[326]
NIR-CD/DOX/MoS_2	NIR laser(808 nm)	PTT/drug delivery	CT	Mice bearing 4T1tumor	Completely eradicate tumor	[383]
MoS_2-HA-DTPA-Gd/Gef	NIR laser(808 nm)	PTT/drug delivery	MRI	Mice bearing A549 tumor	Reduce tumor volume	[384]
Fe_3O_4@MoS_2-PEG(DOX)-2DG	NIR laser(808 nm)	PTT/drug delivery	MRI	Mice bearing MDA-MB-23 tumor	Reduce tumor volume	[303]
MoS_2-CS-DOX	NIR laser(808 nm)	PTT/drug delivery	CT	Mice bearing Panc-1 tumor	Reduce tumor volume	[237]
PLGA/MoS_2/DOX (PMD)	NIR laser(808 nm)	PTT/drug delivery	PA	Mice bearing 4T1 tumor	Completely eradicate tumor	[290]
MoS_2/$Cu_{1.8}S$/DOX	NIR laser(980 nm)	PTT/drug delivery	PLI/PAT/PTI	Mice bearing A549 tumor	Completely eradicate tumor	[295]
MoS_2@Fe_3O_4-ICG/Pt(IV)	NIR laser(808 nm)	PTT/PDT/drug delivery	MR/IR/PA	Mice bearing H22 tumor	Completely eradicate tumor	[301]
MoS_2-PEG-PEI/siPLK1	/	gene delivery	/	/	/	[352]
G5-MoS_2/Bcl-2 siRNA	NIR laser(808 nm)	PTT/gene delivery	/	Mice bearing 4T1 tumor	Delay tumor growth	[363]
FA/MoS_2/siRNA (HDAC1+KRAS)	NIR laser(808 nm)	PTT/gene delivery	/	Mice bearing Panc-1 tumor	Delay tumor growth	[361]

(*continued on next page*)

Table 2 (*continued*)

Materials	Physically trigger	Therapy	Imaging modes	In vivo models	Therapeutic effect	Refs
MoS_2-AKT scaffolds	NIR laser(808 nm)	PTT/tissue regeneration	/	Mice bearing Saos-2 tumor	Reduce tumor volume	[346]
AuNBPs@MoS_2	NIR laser(808 nm)	PTT/CDT	TPF	/	/	[369]
MoS_2@PANI	NIR laser(808 nm)	PTT/RT	CT/PA	Mice bearing 4T1 tumor	Delay tumor growth	[189]
MoS_2-PEG-CpG	NIR laser(808 nm)	PTT/immunotherapy	/	/	/	[366]
FePt/MoS_2-FA	NIR laser(808 nm)	PTT/drug delivery/ immunotherapy	CT/MRI	Mice bearing 4T1 tumor	Completely eradicate tumor	[374]
$PC_{10}A$/DOX/MoS_2	NIR laser(808 nm)	PTT/PDT/drug delivery/ immunotherapy	/	Mice bearing 4T1 tumor	Completely eradicate tumor	[377]

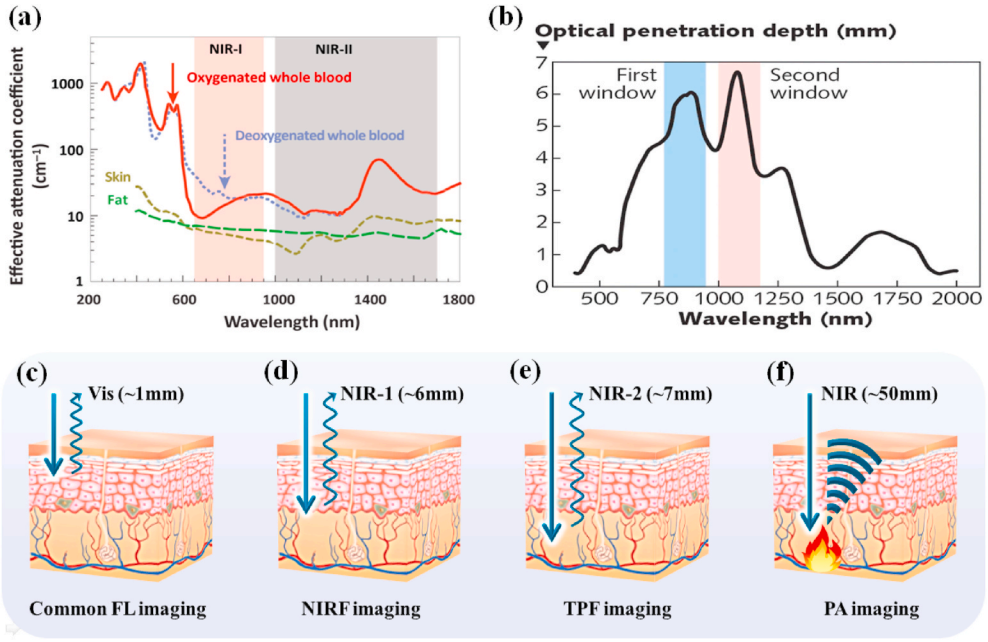

Fig. 5. (a) Effective attenuation coefficient of various biological components, including oxygenated blood, deoxygenated blood, skin, and fatty tissue. Reprinted with permission from Ref. [135]. Copyright 2019, Trends in Chemistry. **(b)** The optical penetration depth of light into skin over the wavelength range from 400 to 2000 nm. Reprinted with permission from Ref. [136]. Copyright 2005, Journal of Physics D: Applied Physics. The penetration depth of **(c)** common FL imaging **(d)** NIRF imaging **(e)** TPF imaging **(f)** PA imaging, respectively.

MoS_2 QDs was an outstanding multiphoton imaging probe (Fig. 6 e). NIR-2 has a longer penetration depth in the living body, lower phototoxicity and better image contrast than NIR-1 [155–160]. Sweet et al. [141] designed a water-soluble anti-PSMA antibody-conjugated MoS_2 QD-based TPF probe for targeted bioimaging of LnCaP prostate cancer cells. Firstly, they used LA-PEG to modify MoS_2 quantum dots (QDs) to improve the stability in physiological environment. LA can effectively form a covalent bond with Mo on the edge of molybdenum sulfide. Subsequently, anti-PSMA antibody conjugated with MoS_2 QDs via PEG to make the TPF probe has targeting ability for prostate cancer cells. The QY of MoS_2 QDs was as high as 54% and their two-photon brightness was detected to be 4.7×10^3 GM, which indicated that MoS_2 QDs were a good TPF imaging probe under the excitation of NIR-2 light (1064 nm). Furthermore, the TPL imaging data proved that anti-PSMA antibody-conjugated MoS_2 QDs could selectively target LnCaP prostate cancer cells and achieve effective TPL imaging in living cells (Fig. 6f and g).

3.2. PA imaging

The principle of PA imaging is that a NIR laser pulse is transmitted into biological tissue, and some of the laser energy is absorbed and transformed into heat, causing a transient thermoelastic expansion, resulting in broadband ultrasonic emission. The resulting ultrasonic waves are then examined by ultrasonic transducers, which are ultimately analyzed to produce an image. The penetration depth of PA imaging can reach ~50 mm thanks to strong penetration of ultrasonic wave. PA imaging technology combines advantages of optical imaging and ultrasound imaging to achieve the tissue image of high resolution and high contrast [161–165]. MoS_2 has outstanding photothermal conversion efficiency and excellent NIR absorption capacity, which can be used for high-quality PA imaging. Yu et al. [166] developed a MoS_2/Fe_3O_4 composite (MSIOs) for photoacoustic tomography (PAT) imaging. MSIOs were prepared by attaching Fe_3O_4 nanoparticles to the surface of the MoS_2 nanoflakes. It's worth noting that MSIOs was a highly sensitive PAT imaging contrast agents and the PAT signals of MSIOs exhibited a concentration-dependent manner with a good linear relationship ($r^2 = 0.995$). The data in vivo showed that the PAT signals were remarkably increased with the prolonging of time after intravenously injecting MSIOs into PANC-1 tumor bearing mice, confirming the gradual accumulation of MSIOs into tumor sites to generate strong PAT contrasts. Furthermore, the relatively long residence time (24 h) of MSIOs in tumors further improved their PAT imaging effect, realizing more effective cancer diagnosis.

In order to further enhance the effect of PA imaging and obtain more accurate information of cancer diagnosis, it is a very effective way to modify nanomaterials with specific targeting functional groups of cancers. Jiang et al. [167] developed transmembrane peptide LNP-modified porous MoS_2 nanoflowers (MNFPPL) as PA contrast agents that could actively target breast cancer. MNFPPL was spiny nanoparticle composed of three dimensional (3D)-stacked MoS_2 nanosheets with large surfaces and abundant pores and the 3D nanostructure could trap the near-infrared light through multiple reflection to strengthen the signal of PA imaging. MNFPPL and porous MoS_2 nanoflowers (MNF) had

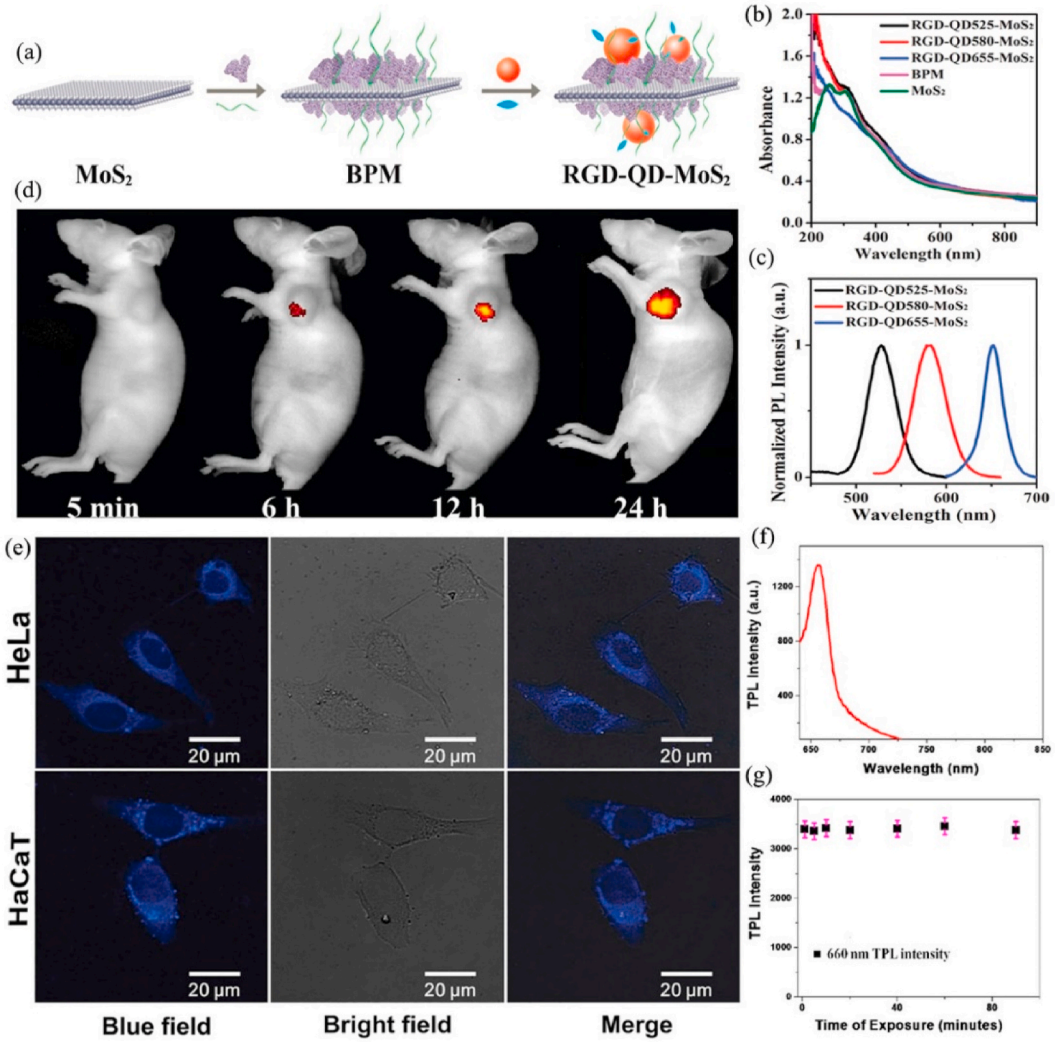

Fig. 6. (a) The preparation of RGD-QD-MoS_2 NSs. **(b)** Ultravioletvisible-near infrared (UV–Vis–NIR) absorption spectra of MoS_2 NSs, BPM NSs, and RGD-QD-MoS_2 NSs. **(c)** Normalized photoluminescence spectra of RGD-QD-MoS_2 NSs. **(d)** Fluorescence images of HeLa tumor-bearing Balb/c nude mice at different times after i. v. injection of RGD-QD_{655}-MoS_2 NSs. Reprinted with permission from Ref. [139]. Copyright 2017, Nanoscale. **(e)** The multiphoton luminescence image of HeLa and HaCaT cells with internalized MoS_2 QDs. Excitation wavelength was 700 nm and detection wavelength in the 420–460 nm range. Reprinted with permission from Ref. [140] Copyright 2015, Small. **(f)** TPL intensity of the MoS_2 QDs at 1064 nm excitation. **(g)** Variation in the TPL intensity with time, indicating that anti-PSMA antibody-attached MoS_2 QDs exhibit very good photostability. For this experiment, we used a laser power density of 40 W/cm^2. Reprinted with permission from Ref. [141] Copyright 2017, ACS omega.

similar near-infrared absorption curves around 808 nm, manifesting that the modification of transmembrane peptide LNP did not change the NIR absorption of MNF. Meanwhile, MNFPPL was absorbed by tumor cells faster and more efficiently than MNF. This result could be attributed to the targeting effect of transmembrane peptide LNP. After intravenously injected MNFPPL or MNFPP (MAL-PEG-PEI-MoS_2), the PA signals reached the maximum at 4 h in carcinoma tissues of 4T1 tumor-bearing mice but PA signal of MNFPPL more rapidly enhanced than MNFPP, which implied that MNFPPL could target the tumor site (Fig. 7 a-c).

Highly sensitive PA signals of MoS_2 can also be obtained by reducing the its layers. The PA signal of MoS_2 will further increase along with the number of layers lessen because MoS_2 with less layers has a higher light absorbance. Currently, PA molecular imaging of deep cerebral tumors remains a challenge partly because the available PA molecular probe has insufficient sensitivity and limited selectivity [168,169]. Chen et al. [170] directly obtained single-layer (S–MoS_2), few-layer (F–MoS_2), and multi-layer (M − MoS_2) nanosheets through albumin-assisted exfoliation without further surface modification. The results showed that reducing the number of nanosheet layers from M − MoS_2 to S–MoS_2 could improve the elasticity of nanomaterials and enhance the absorption of near-infrared light, greatly increasing the PA effect. Meanwhile, S–MoS_2 could be effectively endocytosed by U87 glioma cells and generated a strong PA signal to detect brain tumor cells with high sensitivity. Tumor tissue with a size less than 1.5 mm of skull was still observed in vivo (Fig. 7 d-h).

3.3. CT/PET/MR imaging

NIF-based imaging technology usually can only detect tumors whose subcutaneous depth is less than 50 mm (Table 1). Ultra-short electromagnetic wave like X-rays, γ-photons and long-wavelength electromagnetic wave (42.6 MHz, its wavelength is 7 m) all have extremely longer tissue penetration depth that represents CT/MRI/PET imaging based on these rays can realize a better imaging effect in most tumors located inside the body, as shown in Table 1.

CT is a kind of medical imaging technology, it uses computer to handle multiple X-ray measurements taken from different angles combined to generate the tomographic image of human body. CT imaging

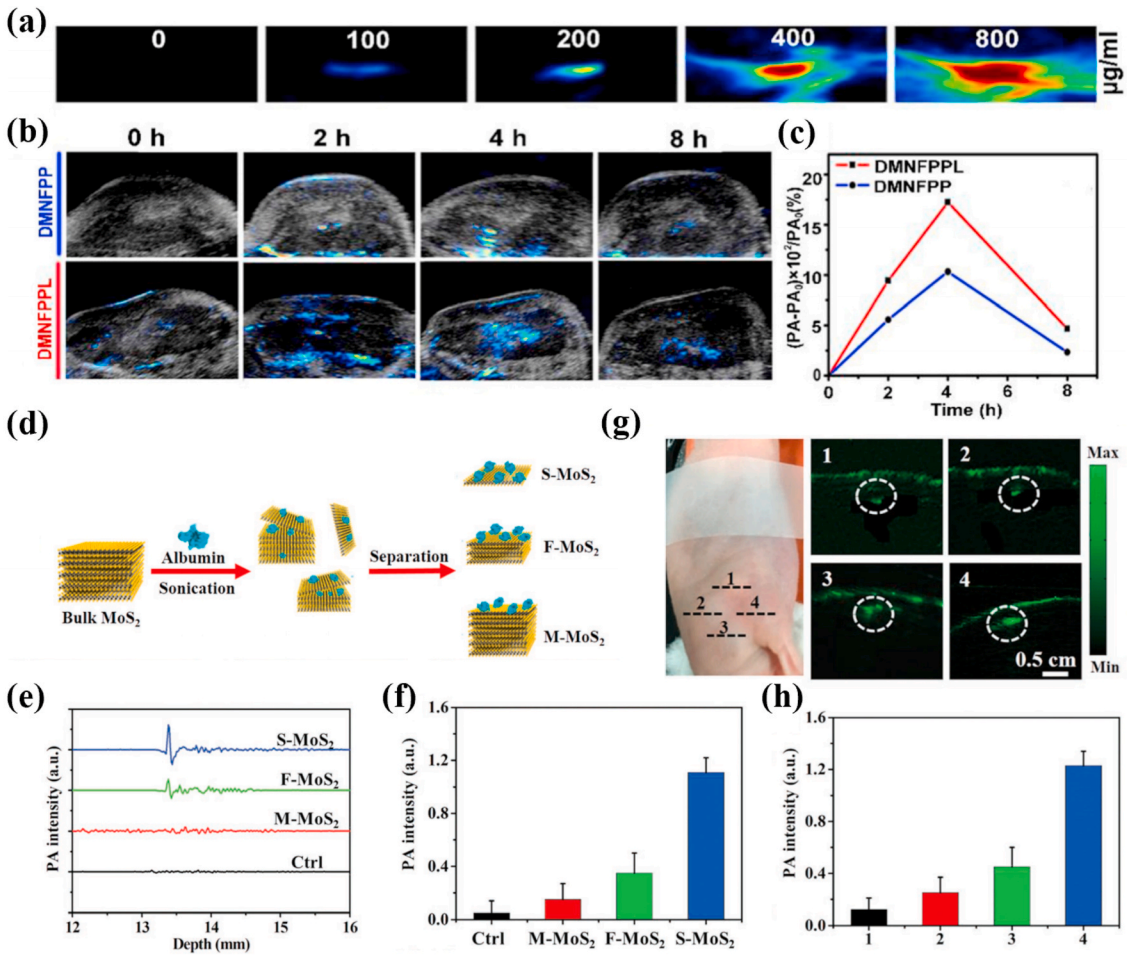

Fig. 7. (a) In vitro PA images of DMNFPPL with different concentrations. **(b)** Real-time PA images of 4T1 tumor-bearing mice at different time points after intravenous administration of DMNFPP and DMNFPPL. **(c)** The curves of PA signal rate changed with administration time periods. Reprinted with permission from Ref. [167]. Copyright 2020, International journal of pharmaceutics. **(d)** Schematic illustration of the synthesis procedure of MoS_2 nanosheets with various layered nanostructures. **(e)** The PA signals produced by S–MoS_2, F–MoS_2, and M − MoS_2 and **(f)** their quantitative results. **(g)** PA images of S–MoS_2, F–MoS_2, and M − MoS_2 in subcutaneous tissue of mice and **(h)** their quantitative results. 1: Control group, 2: M − MoS_2 treated group, 3: F–MoS_2 treated group, 4: S–MoS_2 treated group. Reprinted with permission from Ref. [170]. Copyright 2016, Advanced functional materials.

with fast detection speed can provide tissue density distribution of a certain section and visualize deep cancer structures in the body [171, 172]. MoS_2 nanomaterials can be applied to contrast agents in CT imaging [68,173,174] because Mo atom with high absorption coefficient and atomic number has stronger X-ray attenuation than the components of the body. Liu et al. [175] synthesize antitumor nanocomposites (PEG-MoS_2-Au-Ce6) through adsorbing chlorin e6 (Ce6) onto PEG-MoS_2 nanosheets decorated with gold nanoparticles (AuNPs). The Hounsfield unit (HU) value, represents CT contrast ability, was increased from 121.0 ± 20.1(0 h) to 245.7 ± 18.6 (6 h) when intravenously injected PEG-MoS2-Au-Ce6 into 4T1 tumor bearing Balb/c nude mice, indicating excellent CT imaging effect (Fig. 8 a-c). Besides, Researchers found that MoS_2 nanocomposites had a stronger CT imaging ability in tumor-bearing mice than iohexol [171] or iopromide [176], both are common clinical X-ray contrast agents.

PET imaging has outstanding sensitivity, excellent temporal resolution and superb tissue penetration, which makes it receive much attention in cancer diagnosis, staging and treatment monitoring [179]. Isotope-labeled drugs (PET imaging agents) with positron emission can happen annihilation effects during the physiological metabolism after injecting them into body, producing two γ-photons with equal energy and opposite directions. Radioisotope ^{64}Cu (the half-life of the positron emitter is 12.7 h) could successfully modify MoS_2 for PET imaging [180]. Liu et al. [177] straightforwardly efficiently labeled ^{64}Cu onto double-PEGylated MoS_2-iron oxide (MoS_2-IO-(d)PEG) by mixing $^{64}CuCl_2$ with MoS_2-IO-(d)PEG, which was attributed that the Cu^{2+} ions could anchor on the Mo defect sites of MoS_2 nanosheets. The serum stability test indicated that ^{64}Cu-MoS_2-IO-(d)PEG had a strong stability within 48 h and quantitative PET data, a percentage injected dose per gram of tissue (%ID/g), and confirmed that the enhancement of ^{64}Cu signal was time-dependent. Therefore, ^{64}Cu-MoS_2-IO-(d)PEG could be applied to PET imaging contrast agent for real-time monitoring the body distribution of MoS_2-IO-(d)PEG and therapeutic effect in 4T1 tumor-bearing mice (Fig. 8 d-f). Furthermore, HA could specifically bind to a CD44 receptor overexpressed in MCF-7-ADR cancer cells to improve the tumor-targeting of PET imaging contrast agent. Dong et al. [181] also synthesized ^{64}Cu-NOTA labeled MoS_2-PEI-HA for PET imaging of MCF-7-ADR tumor-bearing mice. PET imaging indicated that the signals at tumor site were remarkably stronger in the HA-targeted group than no targeting group when ^{64}Cu-NOTA labeled MoS_2-PEI-HA and MoS_2-PEI were intravenously injected into MCF-7-ADR tumor-bearing mice for 4 h. Meanwhile, the quantitative results of biodistribution for the MoS_2-PEI and MoS_2-PEI-HA acquired by γ-counter indicated that the accumulation of ^{64}Cu– MoS_2-PEI-HA-NOTA was 10.486 ID/g in MCF-7-ADR tumor area at 4 h post-injection but ^{64}Cu– MoS_2-PEI- NOTA was only 5.015 ID/g, which proved that MoS_2-PEI-HA has high targeting ability to achieve more accurate PET imaging.

MRI is a non-invasive bioimaging technology with a high spatial

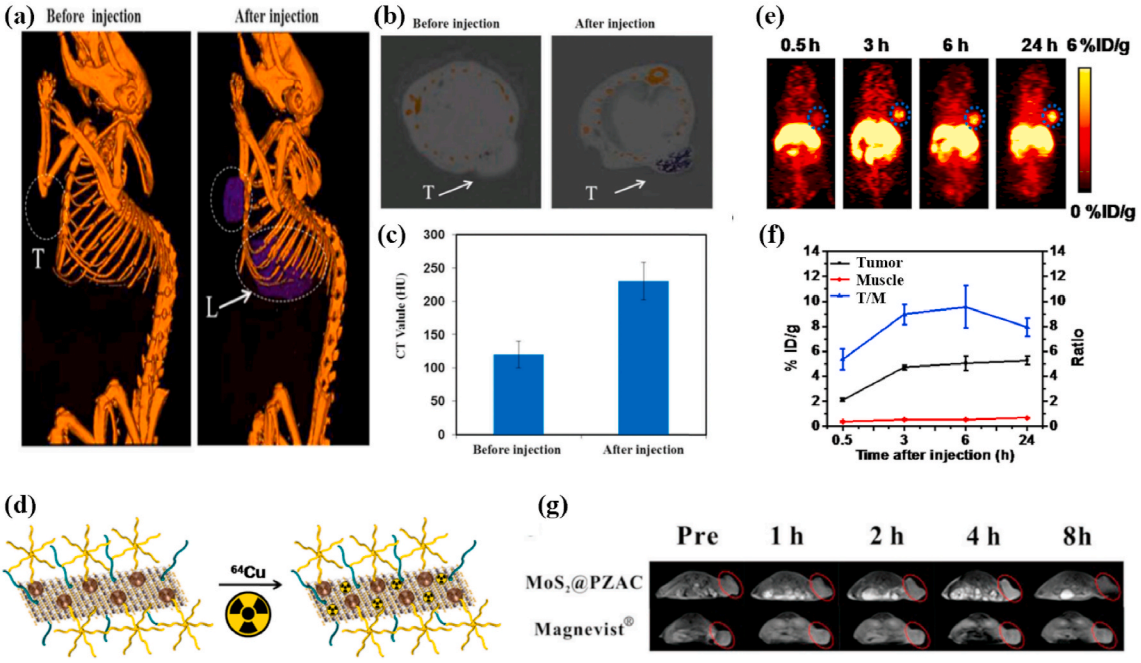

Fig. 8. (a) In vivo CT images of 4T1 tumor-bearing mice before and 6 h after intravenous injection with PEG-MoS_2-Au-Ce6 nanocomposites, tumor (T) and liver (L). **(b)** In vivo CT images of tumors on mice before and 6 h after intravenous injection with PEG-MoS_2-Au-Ce6 nanocomposites. **(c)** Corresponding HU value of PEG-MoS_2-Au-Ce6 nanocomposites in the tumor before injection and 6 h after injection. Reprinted with permission from Ref. [175]. Copyright 2017, Journal of materials chemistry. **(d)** Scheme presenting the ^{64}Cu labeling on MoS_2-IO-(d)PEG via a chelator-free manner. **(e)** PET images of 4T1 tumor-bearing mice taken at various time points post iv injection of ^{64}Cu-MoS_2-IO-(d)PEG. The blue dot circles highlight the 4T1 tumor site of mice. **(f)** Quantification of ^{64}Cu-MoS_2-IO-(d)PEG uptake in the tumor and muscle, as well as the tumor/muscle (T/M) ratio at various time points pi. Reprinted with permission from Ref. [177]. Copyright 2015, ACS nano. **(g)** In vivo T1-weighted MR images of Balb/c mice after injection at different time points (pre-injection, 1 h, 2 h, 4 h, 8 h). Reprinted with permission from Ref. [178]. Copyright 2018, Journal of materials chemistry.

resolution [182] and the image contrast can be enhanced between the diseased and the tissues normal tissues [183,184]. Using long-wavelength electromagnetic waves pulses with a specific frequency (the frequency must match the magnetic field strength) to stimulate the hydrogen nucleus in the body, making the hydrogen nucleus absorb energy and generate resonance. The hydrogen nucleus releases the absorbed energy and emits electromagnetic wave signals after the long-wavelength electromagnetic waves pulses is stopped, which is gathered by a receiver in vitro and treated through an electronic computer for obtaining the MRI image. Gadolinium (Gd) complexes are commonly clinical T1-weighted MRI contrast agents, but free Gd^{3+} has high biotoxicity. Zwitterions are expected to be a substitute to PEG because they have systemic circulating stability and can avoid nonspecific protein adsorption [185,186]. Also, the carboxybetaine monomers of zwitterionic polymers are rich in –COOH groups which can coordinate with MoS_2 to form a stable conjugated system [187]. Yu et al. [178] prepared paramagnetic zwitterionic amphiphilic copolymer (PZAC) by introducing the zwitterionic monomer carboxybetaine methacrylate (CBMA) into the amphiphilic copolymer backbone to lengthen systemic circulation, and the paramagnetic crosslinker was the Gd^{3+}-monomer complex. Subsequently, PAZC interacted with ammonium tetrathiomolybdate (ATTM) to form MoS_2@PZAC under microwave irradiation. The synergistic effect of the combination between the edge Mo atoms in MoS_2 and the –COOH groups of the CBMA chain in PZAC and the noncovalent interactions between Mo and N on the CBMA promoted the hybridization of MoS_2 and PZAC. The result showed that MoS_2@PZAC had a higher relaxivity (r_1 = 11.2 mM^{-1} s^{-1}) than Magnevists (r_1 of approximately 4.4 mM^{-1} s^{-1}) due to two reasons. One was that the hydrophilic CBMA enhanced the rotational correlation time and water exchange rate based on Solomon-Bloembergen-Morgan (SBM) theory, and the other was that the multiple Gd^{3+} centres in the MoS_2@PZAC could also enhance the relaxivity. Meanwhile, the circulation time could be prolonged because MoS_2@PZAC had an appropriate and uniform size (28.5 ± 5.5 nm). Therefore, the PZAC in the spherical MoS_2 nanohybrid (MoS_2@PZAC) acted as a T1-weighted MRI contrast agent to effectively guide MRI imaging in Balb/c mice bearing 4T1 tumors (Fig. 8 g).

3.4. Multi-mode imaging

Single-mode imaging usually has its inherent limitations, such as FL imaging has high resolution but limited penetration, while CT/PET/MRI has strong penetration but low resolution. Multi-mode imaging can overcome the deficiency of single-mode imaging, increasing the accuracy of a cancer diagnosis. In the field of multi-mode imaging, nanocomposites based on MoS_2 have attracted extensive attention because of their unique physicochemical property [188–190].

The most common is to combine the two imaging modes to achieve highly sensitive cancer diagnosis. For instance, Gao et al. [191] prepared rod-shaped heterogeneous Bi_2S_3–MoS_2 nanoparticles (BMNPs) served for CT/PA dual-mode imaging contrast agents. The slope of the HU value against the Bi concentration (8.84 HU L/mmol) was twice higher than commercial I (4.47 HU L/mmol) and BMNPs had a stronger CT imaging brightness. In the meantime, the CT value in 4T1 tumor-bearing mice increased from 37.43 HU to 160.66 HU after injection of BMNPs, manifesting BMNPs possessed excellent CT imaging ability. Moreover, PA signals could be generated by BMNPs even at low aqueous solution concentration (6.25 mM) based on Bi and the intensity of PA signal is positively correlated with concentration of BMNPs within the linear range of 3.125–25 mM. BMNPs with CT/PA imaging capability could improve the precision in cancer diagnosis. Tang et al. [192] also constructed a micrometer-sized materials (mPEG-PLGA@DMF) that integrated MoS_2 nanosheets and Fe_3O_4 nanoparticles into methoxy poly (ethylene glycol) poly(lactic-co-glycolic acid) (mPEG-PLGA) microcapsules. T2-weighted intensity of Fe_3O_4 nanoparticles became gradually stronger and CT signal intensity of MoS_2 nanosheets was progressively enhanced with the increase of mPEG-PLGA@DMF concentration in

vitro. Meanwhile, the tumor site was markedly darken that observed by MRI and the CT signal was increased from 45 HU to 356 HU after injecting mPEG-PLGA@DMF into VX-2 liver orthotopic transplantation tumor, which proved that microcapsules could be successfully applied to MR/CT dual-modal imaging.

Triple-modal or Multi-modal imaging has also been designed to further increase the accuracy of cancer diagnosis. Liu et al. [194] obtained a multifunctional nanocomposites based on an aluminum phthalocyanine chloride (AlPc) loaded MoS_2 nanodot core/SiO_2 shell, which coated by chitosan (CS) to form AlPc-MoS_2@SiO_2-CS. AlPc used as the NIRF imaging contrast agent and MoS_2 nanodot served as PA and CT imaging contrast agent, realizing NIRF/PA/CT imaging in the 4T1 tumor-bearing mice and the signals of the three types of imaging all increasing with the concentration of AlPc-MoS_2@SiO_2-CS increased. NIRF imaging in vivo displayed that AlPc-MoS_2@SiO_2-CS widely distributed all over the body at the early stages after injection and subsequently the NIRF signal at tumor sites gradually increased and reached peak value at 8 h after injection, which implying that the nanocomposites could circulate in the bloodstream and quickly targeted tumors to achieve high precision imaging. MoS_2 nanosheets also have the ability of multispectral optoacoustic tomography (MSOT) imaging due to their strong NIR light absorbance. Yang et al. [193] synthesized mesoporous silica nanoparticles (MSNRs)@MoS_2-HSA/Ce6 nanocomposites for FL/MSOT/CT triple-modal imaging in 4T1 tumor-bearing nude mice. Human serum albumin (HSA) which used as tumor-targeting agents to increase the accumulation of MSNR@MoS_2-HSA/Ce6 in tumor cells via albumin receptor (gp60) and albumin-binding protein SPARC. The FL and MSOT imaging signals showed that the accumulation of MSNR@MoS_2-HSA/Ce6 in the tumor site was gradually increased after 8 h and the peaked at 12 h. Meanwhile, CT signals were positively correlated with the concentration of MSNR@MoS_2-HSA/Ce6 (Fig. 9).

4. Chemotherapy

Compared with surgery and radiotherapy, chemotherapy is a means of systemic treatment. However, chemotherapy usually produces significant side effects due to its low solubility, poor stability, and easy absorption by non-cancer tissues. Hence, it ought to be design effective drug delivery systems (DDSs) to enhance the stability and load rate of drugs, and control the drug release in the tumor tissue, enhancing the therapeutic effect [195–197]. MoS_2-nanomaterials have many merits, including effective load rate, good stability, excellent biocompatibility, and are easy to be functionalized, which can be used as carriers to deliver drugs. Meanwhile, the nanostructure will be destroyed to achieve the release of drugs under the NIR irradiation because MoS_2 can effectively convert the absorbed NIR light into heat energy. Therefore, MoS_2-nanomaterials are promising candidates for drug delivery (Table 2).

Traditional DDSs can successfully deliver drugs to the treatment site, such as ethyl cellulose/chitosan/g-C_3N_4/MoS_2 core-shell nanofibers could co-deliver folic acid and doxorubicin into MCF-7 and HeLa cells [198]. The latest researches focus on how to control drug release to reduce side effects. Drugs can be released accurately and controllably by increasing the sensitivity of DDS to the applied stimuli [199,200]. The pH value of tumor microenvironment (TME) is about 6.5, which is lower than that of normal cells, so pH can act as an excellent internal stimulus to promote the effective release of drugs at cancer sites [201]. Among various stimuli, NIR light with low cytotoxicity can penetrate deep tissues that make it have prominent advantages [202,203]. Local heating

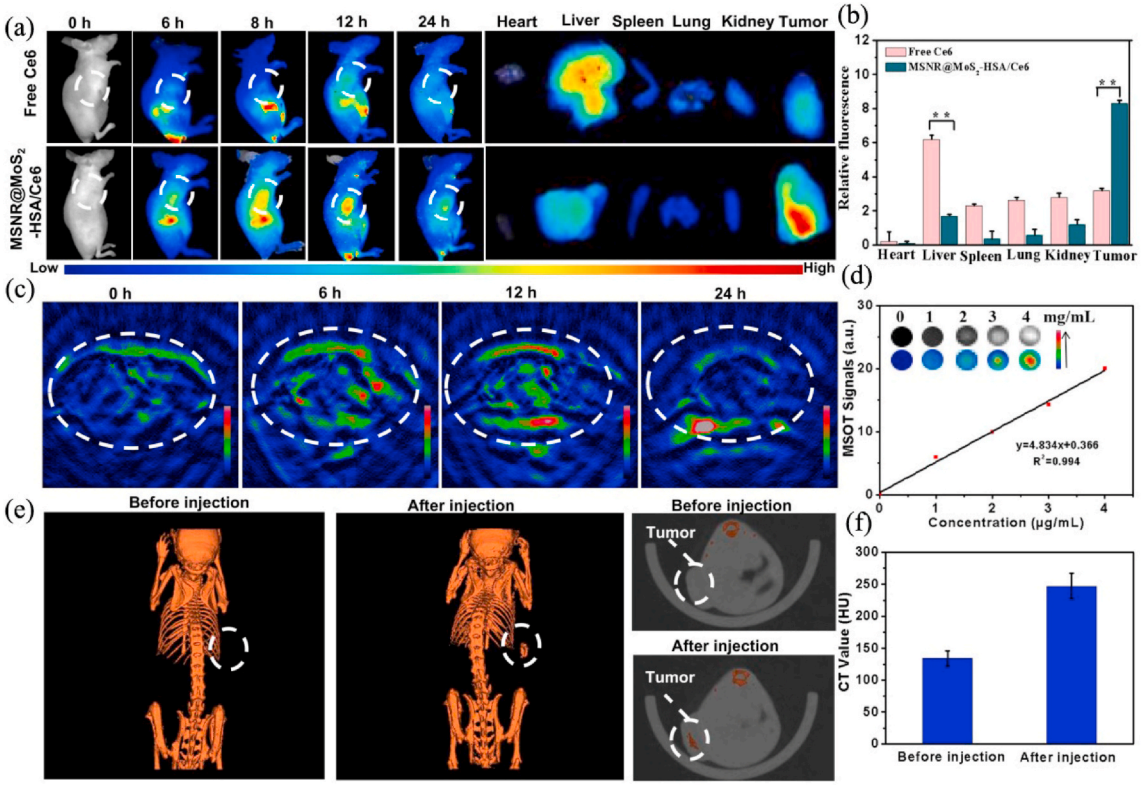

Fig. 9. (a) Fluorescence images of nude mice at different time points after administration of free Ce6 and MSNR@MoS_2-HSA/Ce6; the right panel shows the ex vivo images examined at 24 h. **(b)** Average fluorescence signals of Ce6 in major organs examined at 24 h. **(c)** MSOT images of 4T1 tumor-bearing mice after being intravenously injected with MSNR@MoS_2-HSA/Ce6. **(d)** Photoacoustic intensity linearly fit to the concentration of MSNR@MoS_2-HSA/Ce6 aqueous solutions; inset: the corresponding PA images. **(e)** CT images of tumor site before and after intratumor injection with MSNR@MoS_2-HSA/Ce6. **(f)** Corresponding HU value of MSNR@MoS_2-HSA/Ce6 nanocomposites in the tumor before injection and 12 h after injection. Reprinted with permission from Ref. [193]. Copyright 2019, Theranostics.

will destroy the stability of the endosomal membrane, promoting the escape of drugs and their carriers from the endosomal. The single-layered MoS_2 obtained by lithium intercalation is easily prepared into a dispersion in aqueous solution, which is appropriate for biomedical applications [19]. However, the newly synthesized single-layered MoS_2 has a strong aggregation in the aqueous solution, and thus further modification is needed to increase the stability of the dispersion [204,205]. Related studies showed that using polymer or silica to modify the MoS_2 surface can significantly improve drug loading and colloidal stability. Lee et al. [206] synthesized a photothermal controlled nanoplate to load anticancer drug DOX, which consisted of single-layered MoS_2 coated with porous silica and modified with polyethylene glycol (PEG). The modification of porous silica and PEG significantly enhanced the colloidal stability of the nanocomposite. Meanwhile, the escape of the carrier from the endosome and the release of DOX from nanoplatform were both achieved upon exposure to NIR light radiation. The corresponding half maximal inhibitory concentration (IC_{50}) values of the MoS_2-nanocarrier against HeLa, HepG2, and HCT-8 cell was 1.4-, 36-, and 12-fold that of free DOX respectively, suggesting that MoS_2-nanocarrier had a stronger anti-cancer effect (Fig. 10).

DDSs with a single stimulus-response can only release the drug under a specific stimulus. Therefore, DDSs sensitizing to double or multiple stimuli have attracted more concerns to further improve the therapeutic effect. Since GSH can reduce disulfide bonds (–S–S), it is possible to develop GSH-sensitive DDS by capping hollow mesoporous silica nanoparticles (HMSN) with disulfide cross-linkable polymers to achieve controlled release of drugs. Zhao et al. [207] prepared a dual-functional DDS (HMSN@MoS_2/Tf) that could effectively release DOX from HMSN when degraded by GSH and high temperature. Firstly, they used MoS_2 nanosheets to cap the pores of HMSNs via disulfide linkage after encapsulating DOX into HMSNs. Then transferrin (Tf) was covalently attached on the surface of HMSNs@MoS_2 by forming –S–S to improve the tumor-targeting of HMSN@MoS_2/Tf. MoS_2, a NIR light response element, could not only prevent the pre-release of DOX but also realize controlled drug release by NIR and intracellular reducing agents such as GSH, realizing more accurate release of DOX.

To reduce the absorption of non-cancer tissues during drug delivery and decrease the side effects of chemotherapy, it is essential to explore DDSs with good biocompatibility that can target cancer tissues. Graphene oxide (GO) is capable of localizing in the lung through various pathways (e.g., intravenous (iv) injection) [208–211] and has a high water-solubility [212]. Liu et al. [213] synthesized a MoS_2/GO nanocomposite with high dispersion and excellent biocompatibility that could selectively target the lung. Results showed that the accumulation of MoS_2/GO in the lung is 9-fold greater than bulk MoS_2 and 50-fold greater than Lys-MoS_2 and FA-MoS_2. Meanwhile, compared with GO, the MoS_2/GO possessed better biocompatibility, such as lessened pro-inflammatory effects, improved lung fibrosis and compromised macrophagic activation, which attributed to the decreased reactivity of MoS_2 in the complexes. Furthermore, the drug loading and the killing effect for cancer cells were both increased, and metastatic tumor growth of B16 cells in the lung of mice was also dramatically repressed by MoS_2/GO nanocomplexes.

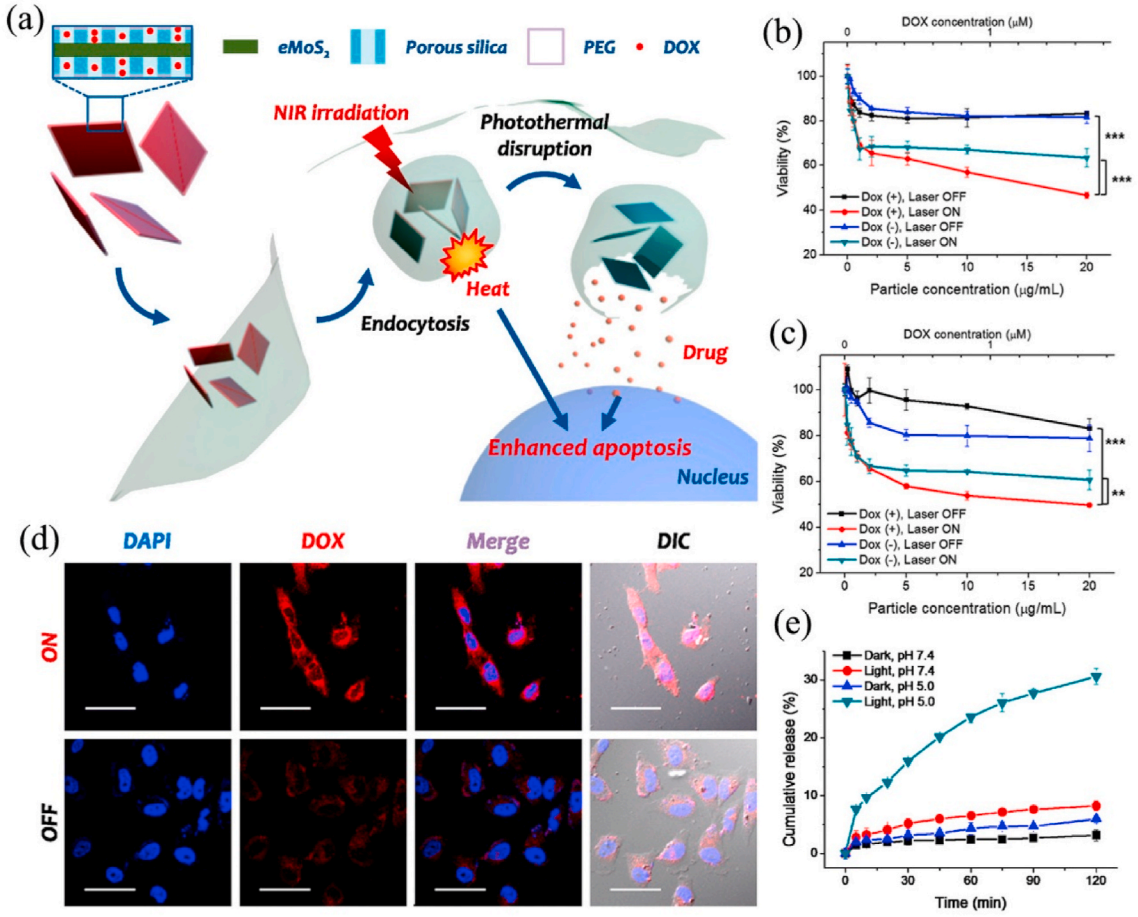

Fig. 10. (a) Schematic illustration of single-layered MoS_2-based nanoplate as a NIR-responsive system. NIR-induced cytotoxicity of DOX-PSMS-PEG or PSMS-PEG against **(b)** HeLa and **(c)** HCT-8 cell line (**p < 0.01, ***p < 0.001). **(d)** Confocal microscopic images of DOX-PSMS-PEG treated HeLa cells which were further irradiated or not irradiated by 808 nm laser (5 W/cm^2). Nucleus was stained by DAPI (blue) and DOX was false-imaged as red (scale bar = 50 μm). **(e)** Photo-responsive drug release of DOX from DOX-PSMS-PEG in vitro. Reprinted with permission from Ref. [206]. Copyright 2016, Chemistry of Materials.

Multidrug resistance (MDR) will reduce the accumulation of drugs in the tumor tissue, reducing the therapeutic effect during cancer chemotherapy [214,215]. Overexpression of p-glycoprotein (P-gp) is the main reason for MDR [216], inhibiting its expression can therefore enhance the therapeutic effect. Hyaluronic acid (HA) with excellent biocompatibility can specifically bind to the CD44 receptors that are highly expressed in drug-resistant cancer cells [217], and be degraded by hyaluronidase (HAase) overexpressing in the tumor microenvironment [218]. Dong et al. [219] designed polyethyleneimine (PEI) and HA-modified multifunctional MoS_2 nanofibers (MoS_2-PEI-HA) for actively targeting drug-resistant MCF-7-ADR cells with high expression of CD44. MoS_2-PEI-HA could be effectively absorbed by MCF-7-ADR, and then released DOX under stimulation of HAase and NIR laser. Importantly, the nanocarrier could significantly inhibit the expression of P-gp to improve sensitivity of chemotherapy, which attributed to the combination of HA targeting and mild NIR laser stimuli. The results indicate that DOX@MoS_2-PEI-HA + NIR groups had a stronger therapeutic effect than DOX@MoS_2-PEI-HA groups, MoS_2-PEI-HA + NIR groups and DOX groups in MCF-7-ADR tumor-bearing mice.

5. Phototherapy

Although nanomedicine and nanobiotechnology have made tremendous progress and promoted the early diagnosis and treatment of cancer [220], cancer still is the most serious and challenging illness and the leading cause of death [221–225]. Therefore, it is urgent to explore new strategies with high treatment efficiency and low toxic reaction. Phototherapy including photothermal therapy (PTT) and photodynamic therapy (PDT) is an emerging alternative therapy for traditional cancer treatments [226,227]. Different from traditional cancer therapy, phototherapy has its own unique advantages. On the one hand, phototherapy can precisely be controlled by selection of irradiation location, time and intensity. The limitation of phototherapy is the limited depth of tissue penetration. Nanomaterials with NIR absorption ability can improve the efficiency of phototherapy to a certain extent. The rich van Hove singularity peaks in the electronic density of states ensures the strong light-matter interactions in MoS_2, which leads to high NIR light absorption [228]. Meanwhile, MoS_2 also has a strong photothermal conversion capability that promotes its applications for phototherapy (Table 2).

5.1. Photothermal therapy

PTT is a strategy mediated by PTT agents [229,230] which can effectively turn absorbed NIR light into heat [231], killing cancer cells with minimal side effects because tumor cells are more sensitive to heat [232,233]. Compared with traditional methods, PTT has smaller invasiveness, higher accuracy and spatiotemporal selectivity, achieves a high degree of localization and can be applied to areas where surgery is difficult [234]. NIR light in the range of 700–1100 nm has high transparency in biological tissues, blood, and water, which can be used to induce photothermal therapy [235,236].

Previous studies have found that MoS_2 nanosheets modified with PEG, L-cysteine or chitosan could be used as PTT agents [68,237–239]. However, the process of obtaining MoS_2 through chemical exfoliation based on "top-down" strategy is time-consuming, and cannot control the thickness and morphology of the MoS_2 nanosheets. Besides, complicated surface modification is required to ensure its stability in the physiological environment. Therefore, the typical "bottom-up" strategy is the other choice to produce high-quality 2D MoS_2 nanosheets. Wang et al. [240] used the PEG-400 aqueous solution as the solvent, for the first time, to synthesize PEGylated MoS_2 nanosheets through the one-pot solvothermal reaction. Notably, the modification of PEG could promote the small-size MoS_2 to remain stable under physiological conditions and have strong photothermal conversion capacity. Meanwhile, the anti-cancer effect of PEGylated MoS_2 nanosheets could be further improved because surface-grafted PEG macromolecules could increase the blood circulation time to generate more heat (Fig. 11 a, b). Fu et al. developed interlayer-expanded MoS_2 (E-MoS_2) nanosheets through solvothermal reaction as PTT agents [241]. The photothermal conversion efficiency of E-MoS_2 nanosheets was as high as 62% thanks to their wide interlayer spacing (0.94 nm). The wide interlayer spacing could improve the accessibility of water, which conduced to increase the capacity of near-infrared light absorption and the ability of repeated light reflections. Furthermore, the heat storage and transport of E-MoS_2 nanosheets could be improved by the large interlayer spacing.

Although MoS_2 nanosheets with controllable size can increase the therapeutic effect of PTT, how to successfully construct tumor-targeted PPT agents is still a challenge. Studies have shown that adjusting the size of PTT agents to 50–300 nm can enhance their targeted delivery capabilities [243]. Feng et al. [244] synthesized a three-dimensional flower-shaped MoS_2 nanoflake with an average size of 90 nm, which had good colloidal stability after modifying with lipoic acid-terminated polyethylene glycol (LA-PEG). Compared to single modification with thiol PEG, the LA-PEG molecule with two S atoms has stronger binding force to MoS_2. The nanocomplexes could destroy the lysosomal membrane and reduce the adhesion of tumor cells when radiated by NIR light at 808 nm, promoting cancer cell death.

Although changing the size of the PPT agent can heighten its tumor targeting, most of them would be cleared by the reticuloendothelial system (RES), so only less than 5% of them could reach the cancer tissue after intravenous injection [245,246]. Notably, the PTT agents can arrive at tumor areas directly via transarterial administration (TA) [247]. Tan et al. [242] constructed layered MoS_2 hollow spheres (LMHSs), which had higher photothermal conversion efficiency (34.46%) than MoS_2 nanosheets (24.37%). At the same time, intra-arterial (i.a.) injection in New Zealand white rabbits with hepatic metastasis of VX 2 carcinoma demonstrated significantly improved the tumor-targeting efficiency of LMHSs. Studies showed that cancer cells could be ablated by single NIR light irradiation (Fig. 11 c, d).

With the deepening of research, the biodegradability of PTT agents has attracted more attention because most inorganic nanomaterials cannot be degraded by the body, significantly hindering their clinical application [248,249]. Nanomaterials can be quickly excreted from the body via the renal-clearance pathway when the hydrodynamic diameter of nanoparticles is less than the glomerular filtration threshold (less than 10 nm) [250,251]. Liu et al. [252] synthesized ultra-small MoS_2 nanodots by one-step solvothermal decomposition. The hydrodynamic diameter of the MoS_2-GSH nanodots was less than 10 nm and without aggregation in physiological buffers when being modified with GSH. The MoS_2-GSH nanodots could induce local high temperature to ablate tumor cells, and was almost completely cleared by the kidney within 7 days at the injected dose.

Although the retention time of ultra-small nanoparticles with a size smaller than the glomerular filtration threshold in normal organs is decreased [253,254], the accumulation concentration and retention time in tumor tissues will also be affected due to the relatively short cycle time and weakened enhanced permeability and retention (EPR) effect [255]. Therefore, biodegradable nanomaterials with large size can not only exert the advantage of inorganic nanoparticles but also avoid long-term biotoxicity [256,257]. Chen et al. [258] used polyacrylic acid (PAA) to synthesize biodegradable MoS_2 nanosheets. Amino-terminated PEG could conjugate with active carboxyl groups in PAA of MoS_2-PAA via the amide reaction to form PEGylated MoS_2 nanoflakes (MoS_2-P-PEG). PAA not only promoted the modification of PEG, but also made MoS_2 nanosheets degradable. Meanwhile, MoS_2-PPEG had excellent stability and photothermal properties in various media. Importantly, the degradation rate of MoS_2-PPEG was distinct under different pH conditions, probably because the concentration of hydroxide ions played an important role, and the primary Mo^{IV} in MoS_2-PPEG was ultimately oxidized to Mo^{VI} during the degradation process. MoS_2-PPEG degraded rapidly in neutral pH solution but slowly in the acidic

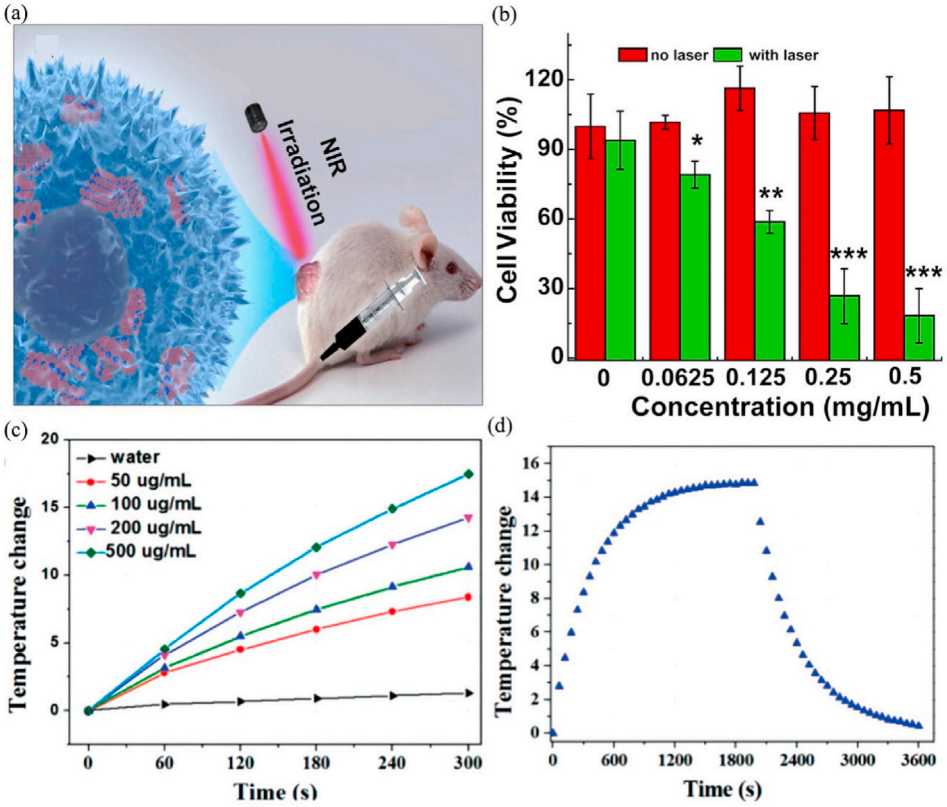

Fig. 11. (a) Schematic illustration of PTT, mouse was intravenously injected with MD_{80}-PEG dispersion and irradiated with NIR laser. **(b)** Cell viability assay of 4T1 cells after treated with or without 808 nm NIR laser (5 min, 1 W/cm^2), cells were pre-incubated with MD_{80}-PEG (0.5 mg/mL) for 4 h before laser irradiating (mean ± SD, n = 3). Reprinted with permission from Ref. [240]. Copyright 2015, Biomaterials. **(c)** The temperature elevation of LMHSs with different concentrations under the NIR laser irradiation. **(d)** The photothermal response of the LMHSs aqueous solution with NIR laser irradiation and then the laser was shut off. Reprinted with permission from Ref. [242]. Copyright 2016, Small.

microenvironment, promoting its accumulation in tumor tissues and enhancing the anti-cancer effect.

5.2. Photodynamic therapy

PDT is mediated by photosensitizer (PS) [259]. Under light irradiation, PS transitions to the excited singlet state and subsequently returns to the ground state, and transfer the energy released from the process to oxygen molecules in the medium to generate ROS. ROS with high reactivity can oxidize biomolecules such as lipids, proteins, and DNA, leading to cell death [260,261]. PDT has the characteristics of minimally invasive. It can also eliminate small recessive cancer nests

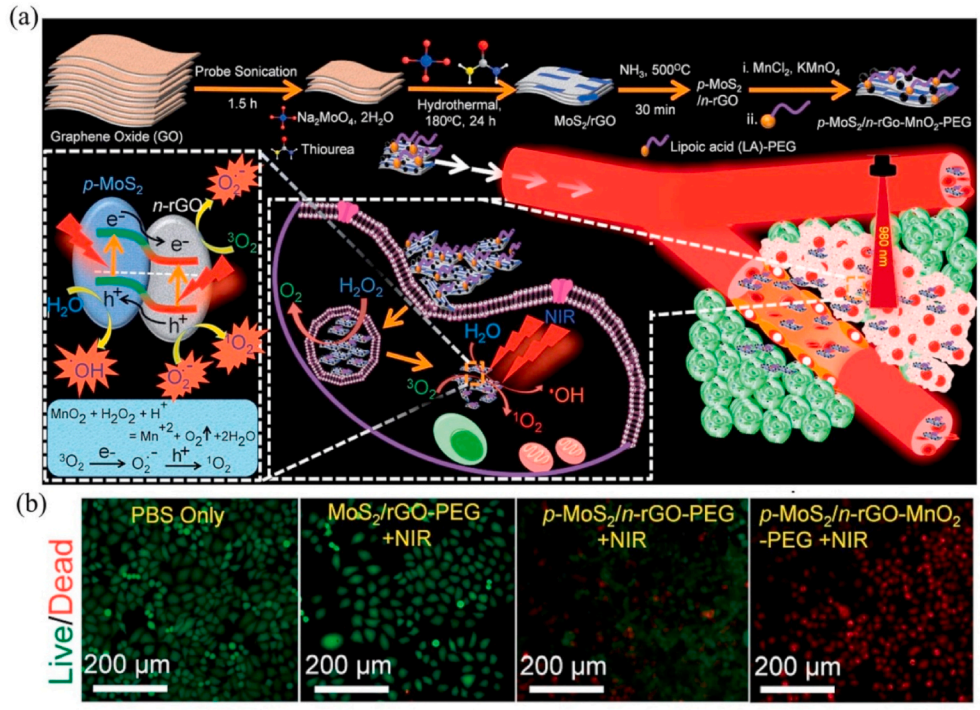

Fig. 12. (a) Schematic illustration of the fabrication of p-MoS_2/n-rGO-MnO_2-PEG nanosheets. While the hybrid nanosheets generate ROS via electron-hole separation under 980 nm laser irradiation, the MnO_2 NPs trigger the decomposition of endogenous H_2O_2 into O_2, simultaneously enhancing the PDT effect. **(b)** Merged epifluorescence microscopy images of HeLa cells co-stained with fluorescein diacetate (green emission for live cells) and PI (red emission for dead cells) under 0.4 W/cm^2 laser irradiation for 5 min. Reprinted with permission from Ref. [262]. Copyright 2018, Chemical Science.

and reduce the chance of tumor recurrence.

Local hypoxia of the tumor microenvironment can result in increased synthesis of lactic acid, promoting proliferation and migration of cancer cells. Photosensitive nanomaterials are capable of alleviating local hypoxia to improve the therapeutic effect of cancer. Kapri and Bhattacharyya [262] adopted the concept of p-n heterojunction to synthesize p-MoS_2/n-rGO nanosheets (p-MoS_2/n-rGO-MnO_2-PEG) as a PDT agent, which could obtain effective electron-hole separation to promote the generation of ROS in tumor tissues when irradiated by NIR (980 nm) light. Meanwhile, p-MoS_2/n-rGO-MnO_2-PEG could alleviate the hypoxic microenvironment because MnO_2 can reduce H_2O_2 to produce O_2 via the Fenton reaction. Therefore, the cell mortality rate of p-MoS_2/n-rGO-MnO_2-PEG was 3 times and more than 5 times that of MoS_2/rGO--PEG or p-MoS_2/n-rGO-PEG, respectively, at the same concentration (Fig. 12).

PTT and PDT have inherent limitations due to their distinct mechanisms. PTT usually requires high-power laser irradiation to generate sufficient heat [263]. Besides, the self-protective effect of cancer cells will cause a heat shock response, weakening the curative effect during PTT [264,265]. Meanwhile, the therapeutic effect of PDT will be suppressed by the hypoxic microenvironment, because of the strong dependence on the oxygen concentration [266,267]. Studies found that the photothermal effect may increase blood flow in the tumor area, subsequently increasing the tumor area's oxygen supply and improving the efficiency of PDT [268]. Therefore, the combination of PTT and PDT will provide new strategies for cancer treatment.

For example, Liu et al. [269] utilized PEGylated MoS_2 (MoS_2-PEG) to physically adsorb the photodynamic agent chlorin e6 (Ce6) for PDT treatment. Compared with free Ce6, MoS_2-PEG/Ce6 could enhance cell uptake and the curative effect of PDT via mild NIR light radiation, given the fact that moderate hyperthermia can increase cell membrane permeability. The synergistic effects of PDT and PTT could achieve more effective cancer cell killing when simultaneously irradiated at 808 nm and 660 nm. Peng et al. [270] designed a 2D MoS_2-based pH-responsive nanosystem that firstly used pH-responsive charge-switchable peptide (lipoic acid (LA)-K_{11}(DMA)) to modify MoS_2, then loaded the toluidine blue O (TBO, photosensitizer) on MoS_2 by physical adsorption. The negatively charged LA-K_{11}(DMA) peptides were turned into a positively charged peptide under acidic conditions, whose charge conversion reduced the binding force between positively charged TBO and MoS_2, resulting in the release of TBO and realizing fluorescence imaging. Besides, the positively charged nanoplatforms were easily endocytosed by cancer cells. The pH-responsive MoS_2 nanosystem combined PTT and PDT into a platform which possessed highly specific and effective anti-tumor effects. Multidrug resistance is one of the main obstacles to cancer treatment, and p-glycoprotein (P-gp) is the main protein to mediate multidrug resistance. Curcumin (Cur) can inhibit the effect of P-gp and reduce the efflux of nano-drugs by cancer cells. Li et al. [271] integrated indocyanine green (ICG), Cur and layered MoS_2 hollow spheres (LMHSs) into one nanoplatform for PTT-PDT. LMHSs and ICG could trigger PTT and PDT respectively under 808 nm NIR radiation. Meanwhile, Cur repressed the activity of P-gp to increase the accumulation of ICG&Cur@MoS_2. The LMHSs had a very good anti-cancer effect because it effectively overcomed multi-drug resistance. In their experiment, ICG&Cur@MoS_2 + NIR group exhibited the strongest anti-cancer ability than ICG@MoS_2 + NIR group and MoS_2 + NIR group.

6. Microwave hyperthermia

The microwave beam can be focused with a suitable shape to concentrate the energy. This feature makes it suitable for local minimally invasive treatment of tumors. Compared with other hyperthermia methods, the main advantages of microwave hyperthermia are longer penetration depth, quicker heat generation, larger ablation area. However, due to the irregular tumor or the large tumor volume, there is the possibility of incomplete microwave ablation. These surviving tumor cells will become a hidden danger of tumor recurrence and metastasis. Researchers have shown that the space between MoS_2 layers can retain molecules or ions [21,272,273]. Meanwhile, dipole polarization and ionic conduction are the two main causes of microwave hyperthermia [274]. The dipoles or ions would arrange in the oscillating electric field under MW irradiation, and generate heat through molecular friction and dielectric loss [275]. Besides, the sandwich structure of nanometer scale-spaces (NSSs) can markedly enhance the heating effect by changing the state of dipoles and ions [276–278], which promotes the application of MoS_2 in microwave hyperthermia (Table 2). Wang et al. [279] prepared layered MoS_2 nanoflowers and used them as the MW sensitizer for MW hyperthermia for the first time. BSA-MoS_2 nanoflower had low systemic toxicity and outstanding microwave sensitivity. MoS_2 nanoflowers were composed of many NSSs and the layered structure enhanced the microwave heating effect. There were two reasons that might result in enhancement of the MW heating effect of NSSs: (1) layered nanoflowers could efficiently recruit and enrich ions due to their large specific surface, enabling a high concentration of ions within BSA-MoS_2; and (2) the frictional collision frequency of dipoles or ions markedly increased because the small volume prolonged the contacting time by repressing the precursor diffusion. In vivo results showed that the tumor could be 100% eliminated after MW radiation at 1.8 W and 450 MHz.

However, microwave hyperthermia is still not feasible for treating large tumors due to insufficient heat accumulation around the whole tumor, owing to the heat-sink effect (HSE) [281–283]. Arterial embolism (TAE) and chemoembolization (TACE) are two common clinical treatments that can block tumor blood vessels to treat unresectable hepatocellular carcinoma (HCC). The means of combining TAE with a specific targeted embolization agent can be utilized for blocking the tumor blood vessels and alleviating the HSE [284,285]. Fu et al. [280] synthesized a microwave embolization agent (MSMC) by encapsulating MoS_2 nanosheets in sodium alginate microcapsules (MCs) for effectively treating large tumors. Compared with free ions participating in microwave hyperthermia, the microwave-heat conversion ability of ions confined in the MC is much higher due to the lamellar structures that could divide the microcapsule into smaller spaces, which would further raise the temperature surrounding solution. Besides, MSMC could be simultaneously used as an outstanding embolic and a microwave sensitizer for dual-enhanced microwave ablation therapy. MR imaging showed that the ablation area of MSMC was larger than that of the microwave treatment alone after injection of MSMC to the VX2 liver cancer tissue via hepatic artery. Meanwhile, persistent hyperthermia could nearly completely ablate the large tumor and prevent its recurrence (Fig. 13).

7. Multifunctional nanoplatforms for cancer therapy

Multifunctional nanoplatforms are mainly divided into two categories: cancer treatments combining different therapy methods and cancer theranostics. The combination of multiple treatment methods can improve the treatment effect, eliminate residual lesions, and prevent metastasis and recurrence for prolonged the survival time of patients. Cancer theranostics is a multifunctional nanoplatforms that combines cancer imaging and treatment. The multifunctional nano-platforms can accurately and timely provide diagnostic information and pharmacokinetics to doctors, which not only make doctors to design personalized treats according to the cancer patient's condition, but also accurately obtain the information of the therapeutic effect for prognosis. Compared with traditional treatment methods, the main advantage of cancer theranostics is that it can distinguish cancer lesions from healthy tissues, which minimize systematic toxicity of cancer treats and improve curative effects. However, multifunctional nanoplatforms need a key flexible platform material that can combine many different functional components together. MoS_2 nanomaterials is easy to functionalized with biomolecules and combined with other nanomaterials. Therefore, MoS_2

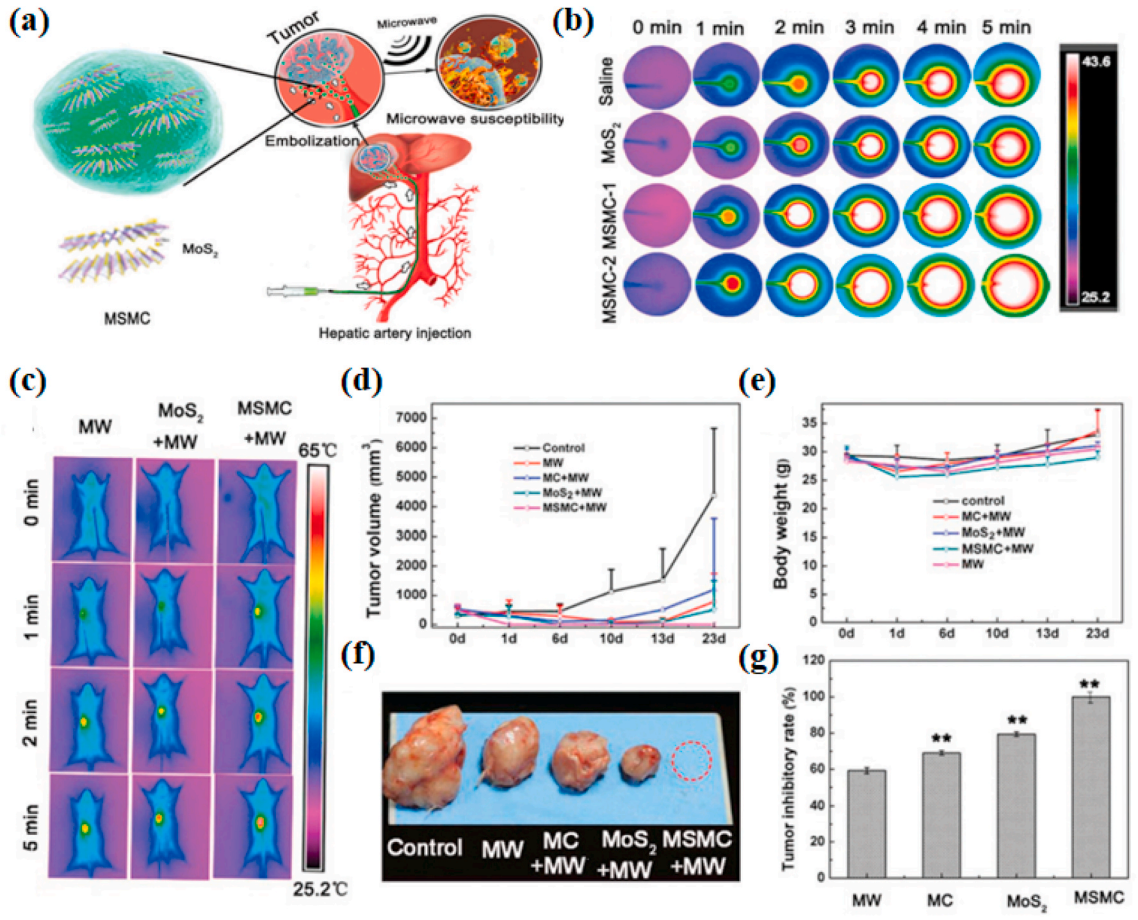

Fig. 13. (a) Schematic illustration of the MSMC used for the microwave ablation and the TAC therapy. **(b)** Near-infrared thermography images with different MW susceptible agents. **(c)** Infrared thermal imaging of mice bearing H22 cells after the intratumoral injection of MSMC, MoS_2 nanosheets, and saline at 50 mg/kg under the MW irradiation for 5 min at 5 W. **(d)** The changes of tumor volume and **(e)** body weight of the mice in different groups. **(f)** Tumor tissues removed from the mice and **(g)** tumor inhibition rate of different groups at 23 day. **p < 0.01. Reprinted with permission from Ref. [280]. Copyright 2017, Nanoscale.

nanomaterial can be used as a good platform material for building multifunctional nanoplatforms [286–288] (Table 2).

7.1. Near-infrared/PA imaging-guided cancer therapy

Han et al. [289] prepared a multifunctional nanocomplex MoS_2-UCNPs-FA/ZnPc by integrating PTT, PDT and up-conversion luminescence (UCL) imaging into one platform to strengthen the anti-cancer effect. First, chitosan-functionalized MoS_2 (MoS_2-CS) with good biocompatibility was covalently grafted with hydrophilic COOH-functionalized upconverted nanoparticles (UCNPs). Thereafter, MoS_2-UCNPs were conjugated with FA through a carbodiimide cross-linking reaction between the –COOH of MoS_2-UCNPs and the $–NH_2$ of FA. Finally, phthalocyanine (ZnPc), was loaded on the surface of MoS_2 to construct MoS_2-UCNPs-FA/ZnPc. Results showed that the nanoplatform could convert optical energy into heat by MoS_2 and generate ROS by ZnPc under NIR light irradiation at 808 nm and 980 nm, respectively. Meanwhile, the unique UCL emission afforded a significant method for cell bioimaging, achieving a more effective therapeutic effect of tumors.

However, the sensitivity and spatial resolution of UCL imaging are relatively lower than those of PA imaging. PA imaging possesses stronger penetration, higher contrast, and more sensitive spatial resolution on account of combining the advantages of optical imaging and acoustic imaging. Wang et al. [290] dissolved polylactic acid-glycolic acid copolymer (PLGA), MoS_2, and DOX into N-methylpyrrolidone (NMP) for preparing PLGA/MoS_2/DOX (PMD) oleosol with good injectability, which did not diffuse into the body fluid circulation and could be biodegraded in vivo. MoS_2 nanosheets serve as high-performance contrast agents to monitor the position of solid PMD implants via PA imaging. Besides, MoS_2 could also be used as PPT agent to control the release of DOX and generate heat, enhancing the anti-cancer effect in tumor-bearing nude mice. Compared with NIR-1, NIR-2 has a longer penetration depth and better image contrast. Zhou et al. [291] developed 1T-MoS_2 nanodots as effective nano-agents for PA imaging-guided PTT in the NIR-2 window. 1T-MoS_2 nanodots gave an extinction coefficient of 25.6 L g^{-1} cm^{-1} and photothermal power conversion efficiency (PCE) of 43.3% under 1064 nm laser irradiation. The strong NIR-2 absorption of 1T-MoS_2 could be attributed to the metallic properties. In an attempt to further enhance the sensitivity of imaging, Song et al. [292] designed the "four-in-one" nanoplatform consisting of fluorescent imaging, PA imaging, PTT, and PDT to achieve imaging-guided phototherapy. BSA-MoS_2 could simultaneously generate local high temperatures, singlet oxygen, and PAT signals after 808 nm NIR laser excitation. Besides, the biodistribution of nanocomplex at the tumor site could be detected by fluorescence imaging when MoS_2 conjugates with Cy5.5 fluorescent molecules, realizing multimode imaging-guided precision treatment.

Enhancing the tumor targeting of multifunctional nanomaterials can reduce the side effects on normal tissues. Shin et al. [293] reported a multifunctional HA-MoS_2 with the tumor-targeting capability as well as integrated fluorescence imaging, PAT, and PTT. Thiolated HA (HA-SH) was first prepared by chemically modification of hyaluronate (HA) with cystamine. The as prepared HA-SH was then conjugated with MoS_2 via the disulfide bond formation. HA promoted the accumulation of

HA-MoS_2 at the tumor site through HA receptor-mediated endocytosis. Meanwhile, the disulfide bond of HA-MoS_2 could be reduced by GSH in the cytoplasm, releasing MoS_2 sheets to strengthen the optical signal and photothermal conversion efficiency, realizing effective tumor ablation effect in Balb/c nude mice inoculated with HCT116 (Fig. 14 a-f).

The synergistic effect between MoS_2 and other photothermal conversion agents can increase the photothermal conversion efficiency and the therapeutic effect of PTT, also enhancing the sensitivity of PA imaging. Copper sulfide (CuS) is an excellent photothermal conversion material because of its good thermostability, photostability and high photothermal conversion efficiency [294]. For this reason, Meng et al. [295] prepared a multifunctional nanoplatform (ATPMC) through

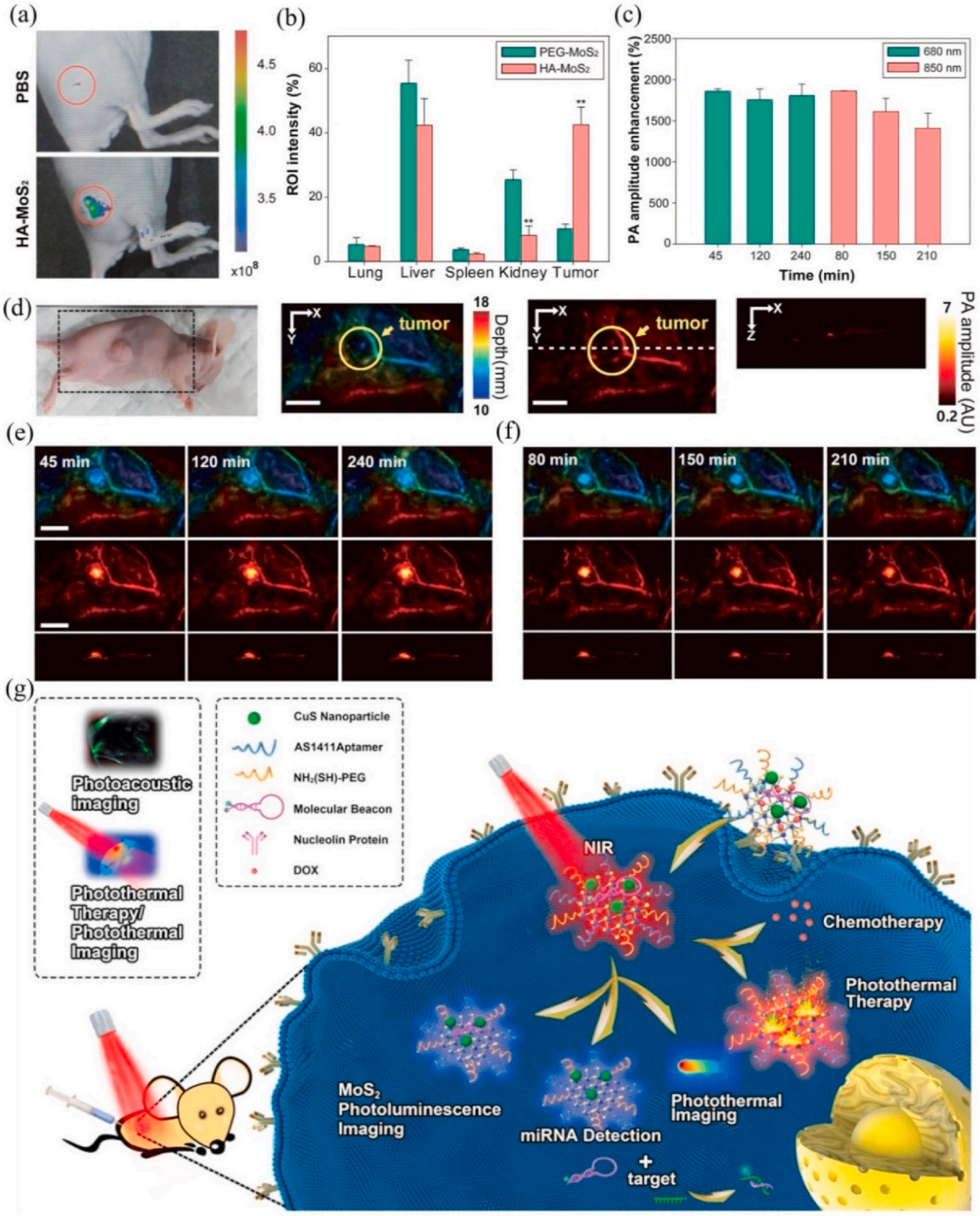

Fig. 14. In vivo fluorescence and PA imaging of HA-MoS_2 conjugates. **(a)** IVIS imaging of PBS and HA-MoS_2 conjugates after intradermal injection into the tumor (red circle) region. **(b)** Quantitative fluorescence analysis of PEG-MoS_2 and HA-MoS_2 conjugates in the organs for the assessment of tumor targeting affinity (**$p < 0.01$, PEG-MoS_2 vs HA-MoS_2 conjugates). **(c)** The PA amplitude enhancement of HA-MoS_2 conjugates compared to the control (PBS) image at both 680 and 850 nm wavelengths with the depth profile of the highest signals for 240 min. **(d)** A photo-image and PA MAP image of mouse in respect to depth (left) and amplitude (right) before injection of HA-MoS_2 conjugates. The PA signals at 30 and 240 min after intratumoral injection of HA-MoS_2 conjugates at **(e)** 680 and **(f)** 850 nm wavelengths in respect to depth (upper) and intensity (bottom). Reprinted with permission from Ref. [293]. Copyright 2019, Advanced Healthcare Materials. **g)** ATPMCD (ATPMC nanoplatform loaded with DOX) for multimodality bioimaging and NIR-laser irradiation-induced chemotherapy. Reprinted with permission from Ref. [295]. Copyright 2017, Advanced Functional Materials.

conjugating aptamer and PEG on the surface of MoS_2–$Cu_{1.8}S$, which not only served as photoluminescence/PA/photothermal imaging contrast agent but also used as carriers of DOX and miRNA-155 probe, realizing triple-modal bioimaging-guided diagnosis and synergistic therapy. The combined effect of MoS_2 and $Cu_{1.8}S$ made ATPMC have stronger heat conversion ability (32.5%) than MoS_2 or $Cu_{1.8}S$ alone, which indicated that ATPMC was a superb photothermal conversion agent. Meanwhile, ATPMC could selectively release DOX under NIR light radiation to kill lung cells (Fig. 14 g).

7.2. MRI-guided cancer therapy

Due to the different relaxation times of normal tissues and cancerous tissues, MRI can provide anatomical information. Conventional MRI cannot recognize the boundary and microstructure of tumor lesions due to its relatively low resolution [296]. Nanoparticle-based MRI contrast agents can provide high-quality and sensitive anatomical information [297,298]. For example, superparamagnetic Fe_3O_4 nanoparticles are commonly used as T2-weighted MRI contrast agents [299,300]. A novel multifunctional complex (Mo@Fe-ICg/Pt) was prepared by covalently grafting Fe_3O_4 nanoparticles (≈6 nm) on MoS_2 and then loading indocyanine green molecule (ICG, photosensitive agent) and platinum (IV) prodrug. The resulting multifunctional nanoparticles possessed remarkable bioimaging capacity of MRI ($r_2 = 71.8\ mM^{-1}\ s^{-1}$)/infrared thermal/PA and could trigger PTT, PDT, and chemotherapy under NIR light irradiation [301]. Notably, the T2-weighted contrast ability may be affected by the morphology and size of Fe_3O_4 nanoparticles [302]. Generally, the larger cubic iron oxide (IO) nanoparticles have lower r_2 value and higher imaging sensitivity. Xie et al. [303] combined MoS_2 (MS) film with IO nanocubes (≈100 nm) to form Fe_3O_4@MoS_2 nanocubes (IOMS NCs), which could easily load DOX for MRI-guided chemo-photothermal therapy. Compared with the nanomaterials containing small-size Fe_3O_4 nanoparticles ($r_2 = 71.8\ mM^{-1}\ s^{-1}$), the IOMS NCs containing large-size Fe_3O_4 nanoparticles displayed more sensitive MRI capabilities ($r_2 = 48.86/(mM{\cdot}s)$) (Fig. 15).

T1-weighted MRI contrast agents, as positive contrast agents, can enhance the signal in the affected area, thus making this area brighter than other areas. Nanoparticles containing Gd^{3+} are commonly used as

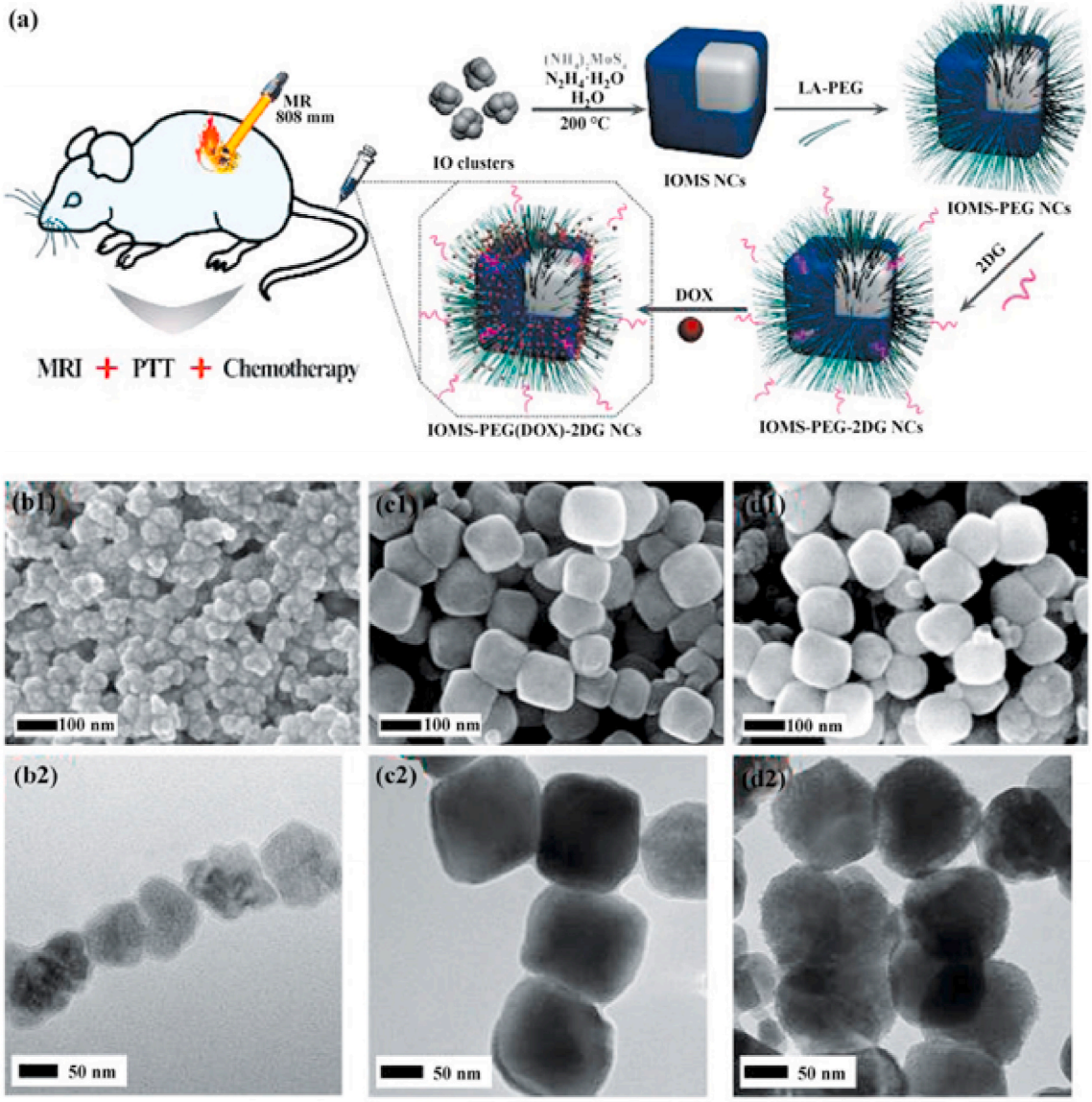

Fig. 15. **(a)** Schematic illustration of the fabrication process of IOMS-PEG(DOX)-2DG NCs for MRI-guided chemo-photothermal therapy of cancer. **(b1)** and **(b2)** SEM and TEM images of IO clusters. **(c1)** and **(c2)** SEM and TEM images of IOMS NCs. **(d1)** and **(d2)** SEM and TEM images of IOMS-PEG NCs. Reprinted with permission from Ref. [303]. Copyright 2018, Nano Research.

T1-weighted MRI contrast agents [304]. Chen et al. [305] synthesized the multifunctional MoS_2-Gd-BSA through conjugation of BSA-gadolinium (Gd) complexes with MoS_2 nanosheets via an amide bond. BSA-Gd complexes were served as MRI contrast agents, while MoS_2 nanosheets used for PTT agents and PA imaging contrast agents, realizing dual-mode MRI/PA imaging-guided PTT in tumor-bearing mice. Besides, Mn^{2+} also serves as T1-weighted MRI contrast agents [306]. The generated T1/T2-weighted MRI contrast agents have demonstrated a higher sensitivity than single-mode contrast agents in cancer identification. Therefore, Mn-doped Fe_3O_4 nanoparticles can be utilized for T1/T2-weighted MRI bimodal probes. Jing et al. [307] synthesized multifunctional nanosystems by loading chitosan (CS) and metformin (MET) on Mn-doped Fe_3O_4@MoS_2 nanoflowers. The Mn-doped Fe_3O_4@MoS_2 nanoflowers were applied to the T1/T2-weighted MRI with high sensitivity ($r_2 = 18.46\ mM^{-1}\ s^{-1}$, $r_2 = 63.75\ mM^{-1}\ s^{-1}$) and had a quick magnetic response. Meanwhile, it could suppress and kill hepatoma cells when MET was released from the nanosystems under NIR irradiation or weakly acidic tumor microenvironment. Therefore, T1/T2 MRI-guided chemo-photothermal combined therapy was realized in vitro. Furthermore, Researchers discovered that incorporating MoS_2 nanosheets and Fe_3O_4 into microcapsules can be used in MRI/CT-guided microwave hyperthermia for HCC [192].

7.3. Combination of phototherapy with chemotherapy

Studies have shown that PTT-induced hyperthermia can interfere with DNA repair [308] and increase membrane permeability [309,310], promoting the entry of drugs into the tumor cells and improving the sensitivity of tumor cells to drugs. Meanwhile, PDT can enhance the penetration of tumor blood vessels and increase the intake of nanoparticles, improving the anti-tumor efficacy of nanodrugs [311,312]. Overall, the combination of phototherapy and chemotherapy can achieve a better therapeutic effect [313–324].

Liu et al. [68] firstly discovered that MoS_2 could be used as a novel 2D nanocarrier to deliver drugs and also used for PTT. The PEGylated MoS_2 nanosheets with the large specific area could efficiently deliver DOX via hydrophobic action and had strong NIR light absorption efficiency. Results displayed that about 95% of cancer cells died when they co-incubated with MoS_2-PEG-FA/DOX and radiated by the 808 nm laser at 1.07 W/cm^2 for 5 min, which was much higher than DOX or PPT treatment alone (Fig. 16 b-f). Furthermore, studies demonstrated that MoS_2 nanosheets modified by chitosan [237], hyperbranched polyglycidyl (HPG) [325] or egg yolk phospholipids [326] could also serve as nanoplatforms with good colloidal stability and biocompatibility to realize the synergistic treatment of chemotherapy and PTT. Time-staggered administration of erlotinib (Er) and DOX can enhance the anticancer effect, but its clinical application is limited due to different administration routes and formulation parameters. Recently, Liu et al. [327] designed a MoS_2-based nanoplatform to co-deliver Er and DOX. Under NIR irradiation, the MoS_2-based nanoplatform could simultaneously release Er and DOX, and greatly improve the anti-cancer effect by synergistic treatment of Er and DOX.

Because MoS_2 with a large specific surface area is easy to modify, many molecules can be combined with MoS_2 to construct various types of multifunctional nanoplatforms for combined phototherapy and chemotherapy. Many outstanding characters, such as organic-group-doped frameworks, high surface area, and excellent blood compatibility, making periodic mesoporous organosilicas (PMOs) become ideal platforms for drug delivery [329–331]. MoS_2 nanosheets might efficiently wrap the PMOs due to its excellent flexibility in chemical reaction [332–334]. To this end, Shao et al. [322] designed PMO-DOX@MoS_2-PEG that has high DOX loading efficiency (160 μg/mg

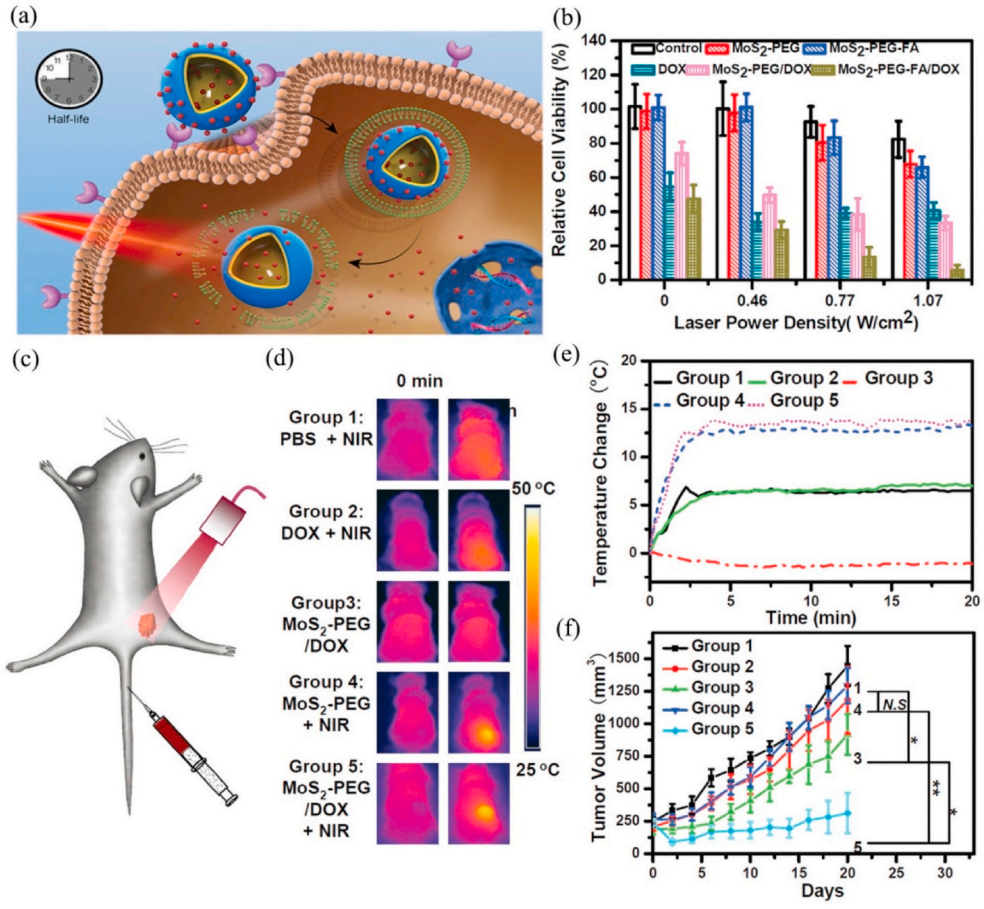

Fig. 16. (a) Schematic illustration of MoS_2/HSA-DOX nanocapsules targeting a cancer cell surface receptor (gp60) and their transcytosis into the cytoplasm. After irradiation, MoS_2 generates heat, and free DOX is released, achieving synergistic photothermal-chemotherapeutic efficacy. Reprinted with permission from Ref. [328]. Copyright 2018, Advanced Functional Materials. **(b)** Relative viabilities of KB cells after various treatments indicated. In this experiment, KB cells were incubated with MoS_2-PEG, MoS_2-PEG-FA, free DOX, MoS_2-PEG/DOX and MoS_2-PEG-FA/DOX for 1 h, and then irradiated with the 808-nm laser at different power densities for 5 min or kept dark as controls. Afterwards cells were washed with PBS, placed into fresh cell medium, re-incubated for additional 24 h before the MTT assay. Error bars were based on four parallel samples. **(c)** Scheme of combination therapy based on intratumorally injected MoS_2-PEG/DOX. **(d)** IR thermal images of 4T1 tumor-bearing mice recorded by an IR camera. The doses of DOX and MoS_2-PEG were 5 mg/kg and 3.4 mg/kg, respectively, in this experiment. Laser irradiation was conduced by using 808-nm NIR laser at the power density of 0.56 W/cm^2 for 20 min on the tumors. **(e)** Temperature change of tumors monitored by the IR thermal camera in different groups during laser. **(f)** Tumor volume growth curves of different groups of mice after various treatments (5 mice for each group). Reprinted with permission from Ref. [68]. Copyright 2014, Advanced Materials.

PMO) and outstanding photothermal conversion capacity, which could successfully release DOX with the irradiation of NIR laser. The release of DOX in PMO-DOX@MoS_2-PEG could be controlled by NIR laser. Benefiting from these properties, a combination therapy of chemotherapy and PTT in multiple cancer cells was achieved.

Researchers have found that improving the tumor targeting and specific response-ability of multifunctional nanomaterials to the tumor microenvironment can further enhance the anticancer effect. Yang et al. [320] prepared a novel type of cabbage-like Fe_3O_4@MoS_2@ZnO nanocomposite with magnetism, extensive pore structure, large surface area, and high DOX loading capacity, which could effectively deliver drugs to tumor lesion areas under magnetic targeting. Meanwhile, the efficient PTT could be realized because MoS_2 has strong photothermal conversion ability, and the controlled release of DOX in slightly acidic environments (pH 6.5) could be achieved by using the pH-dependent ZnO as an encapsulating component to cover the mesopores. Xu et al. [328] synthesized MoS_2/HSA with strong photothermal conversion ability which constructed with MoS_2 hollow nanocapsules and human serum albumin (HSA) by a layer-by-layer coating method. The MoS_2/HSA were uniform in size (280 nm), large in the cavity, low in Young's modulus (222 ± 20 MPa), and high in load rate of DOX (27 wt%). The uptake rate of MCF-7 cells was dramatically increased due to the targeting ability of HSA. Simultaneously, the longer mean retention time (170.9 h) of MoS_2/HSA made it has a higher tumor tissue accumulation (27%) than its solid counterpart, dramatically improving the treatment effect of breast cancer (Fig. 16 a). Melanin (Mel) is a biocompatible biopolymer that exists in human tissues and has the ability to absorb NIR light. Our groups developed dopamine-melanin colloidal nanospheres (Dpa-melanin CNSs) as efficient PTT agents for cancer therapy [335]. The combination of Mel and MoS_2 nanosheets would further strengthen the photothermal effect. Yang et al. [314] synthesized a multipurpose nanosystem based on MoS_2 and Mel nanocomposites (HPMP@(DOX/-Mel)) that could deliver DOX. They first prepared the multi-functional HA-PEI-LA-MoS_2-PEG (HPMP). HA could selectively bond with CD44 receptor which expresses highly in MCF-7 cells to enhance the targeting ability of HPMP, while PEI made HPMP to obtain the function of responding to pH. Subsequently, melanin and DOX were loaded into HPMP to prepare HPMP@(DOX/Mel). The efficiency of HPMP@(DOX/Mel) photothermal conversion could reach 55.3% due to the synergistic enhancement of Mel and MoS_2, which was higher than Mel and MoS_2. The DOX could be released from HPMP@(DOX/Mel) with the dual stimuli of weakly acidic environment and NIR light irradiation at 808 nm. Besides, experiments in vivo demonstrated that chemo-photothermal therapy had a better treatment effect than single therapy. Recently, Zhang et al. [336] constructed urchin-like MoS_2@C with high photothermal conversion ability (40.8%) and high DOX loading rate (52.34%), which could effectively release DOX under the mediation of pH and temperature. The cumulative release rate of DOX was as high as 64.59% when irradiated by NIR, which was about twice as high as that without laser irradiation, and the survival rate of MCF-7 cells was only 25.8%.

7.4. Combination of phototherapy with other therapy

In addition to the synergistic effect of chemotherapy and phototherapy, PTT can also be combined with radiation therapy, tissue regeneration, gene therapy, immunotherapy, and catalytic therapy to overcome the inherent limitations of monotherapy for enhancing anticancer effects and prolonging the survival period of patients.

Nevertheless, PTT alone hardly completely eliminates tumors due to its depth-dependent. Radiation therapy (RT) without depth restriction generally utilizes ionizing radiation to generate oxygen-centered radicals which can promote cancer cell death by causing the DNA damage [337,338]. But the hypoxic tumor microenvironment is the main barrier to RT. Moderate high temperature induced by PTT may increase the bloodstream within the tumor lesions and improve the tumor hypoxic microenvironment, making the cancer cells more sensitive to RT. MoS_2 with high Z value is expected to be a candidate of RT radiosensitizers [339]. Wang et al. [189] designed inorganic-organic nano-hybrid particles based on MoS_2 quantum dots@polyaniline (MoS_2@PANI), which not only enhanced PA/CT signals but also performed RT and PTT for cancer. Firstly, they dispersed MoS_2 QDs powder in the water when polyvinylpyrrolidone (PVP) existed and PVP served as a dispersing and stabilizing agent to control the size of MoS_2 QDs during the process. Subsequently, MoS_2 QDs could absorb aniline molecules onto its surface to form MoS_2@PANI-COOH via the electrostatic forces and then conjugated with PEG-NH_2 by forming the amide bond, constructing MoS_2@PANI nanohybrids. The MoS_2 QDs could be used as fluorescence probes and PANI could serve as a PTT agent due to its strong photothermal conversion efficiency capacity. Besides, MoS_2@PANI could also serve as CT imaging agents because the molybdenum has a high X-ray absorption coefficient. Results showed that oxygenation at the tumor site could be enhanced under moderate PTT. PTT/RT combination therapy guided by PA/CT images could nearly eliminate tumors in 4T1 tumor-bearing mice (Fig. 17 a, b). Besides, MoS_2 can also be combined with other nanoradiosensitive agents to form a PTT-RT combined treatment platform. Hafnium dioxide (HfO_2) nanoparticles have strong X-ray attenuation ability, and are regarded as potential radiosensitive agents. Recently, Fu et al. [340] integrated MoS_2, HfO_2 and dextran into new nanoplatforms (M/H-D) for CT/PA imaging-guided PTT/RT. HfO_2 produced ROS to kill cancer cells under X-ray irradiation. Meanwhile, local high temperature caused by MoS_2 could relieve the hypoxia of tumor cells and improve the therapeutic effect of RT under NIR irradiation. In addition, MoS_2 could catalyze H_2O_2 to produce hydroxyl radicals to further damage cancer cells. M/H-D could eliminate tumors in MMC-7721-fluc tumor-bearing mice after X-ray and NIR irradiation.

Malignant bone tumor is usually treated with a collaborative strategy of surgery, chemotherapy, and radiotherapy [233,341], but cannot thoroughly ablate cancer cells and lead to large bone defects which need bioactive graft materials to repair [342,343]. Fortunately, the osteogenesis and angiogenesis can be induced by three-dimensional (3D)-printed bioceramic scaffolds with bioactive elements [344,345], while these scaffolds gradually degrade with the formation of new bone tissue. Wang et al. [346] prepared new dual-function scaffolds (MS-AKT scaffolds) via the technology that combines a 3D printing technique and a hydrothermal method. First, they immersed AKT bioceramic scaffolds prepared by 3D printing into an aqueous precursor solution including $(NH_4)_6Mo_7O_{24}{\cdot}4H_2O$ and H_2NCSNH_2. Next, H_2NCSNH_2 would be decomposed and attach on the surface of AKT scaffolds under hydrothermal conditions. Finally, AKT scaffolds were used as templates to promote the nucleation and growth of the sheet-like MoS_2 in situ, producing MS-AKT scaffolds. MoS_2 nanosheets with photothermal properties and bifunctional three-dimensional (3D) scaffolds with osteogenic potential could be used to induce PTT and repair bone defects caused by large tumors, respectively. PTT significantly increased the death rate of osteosarcoma cells and breast cancer cells, and the MS-AKT scaffold could support the attachment, proliferation, and osteogenic differentiation of bone mesenchymal stem cells, inducing tissue regeneration in vivo (Fig. 17 c-k).

Gene therapy (GT) induced by small interfering RNA (siRNA) promises to be an alternative means for traditional treatment. It can selectively kill cancer cells by silencing specific genes [347]. However, the naked siRNA with negative charges is easily degraded by nuclease and difficult to cross the negatively charged cell membranes. Therefore, safe and effective carriers are highly needed [348]. MoS_2 can efficiently deliver genes to the target area for cancer therapy due to its flexible physicochemical properties. Polo-like kinase 1 (PLK1), a vital regulatory factor of cell cycle and overexpressed in various cancer. The proliferation of cancer cells will be inhibited by silencing PLK1 expression [349–351]. Kou et al. [352] developed a PLK1 siRNA nano-transport system based on MoS_2 (MoS_2-PEG-PEI nanosystem). In this nanosystem, PEG could prevent nonspecific binding of proteins and

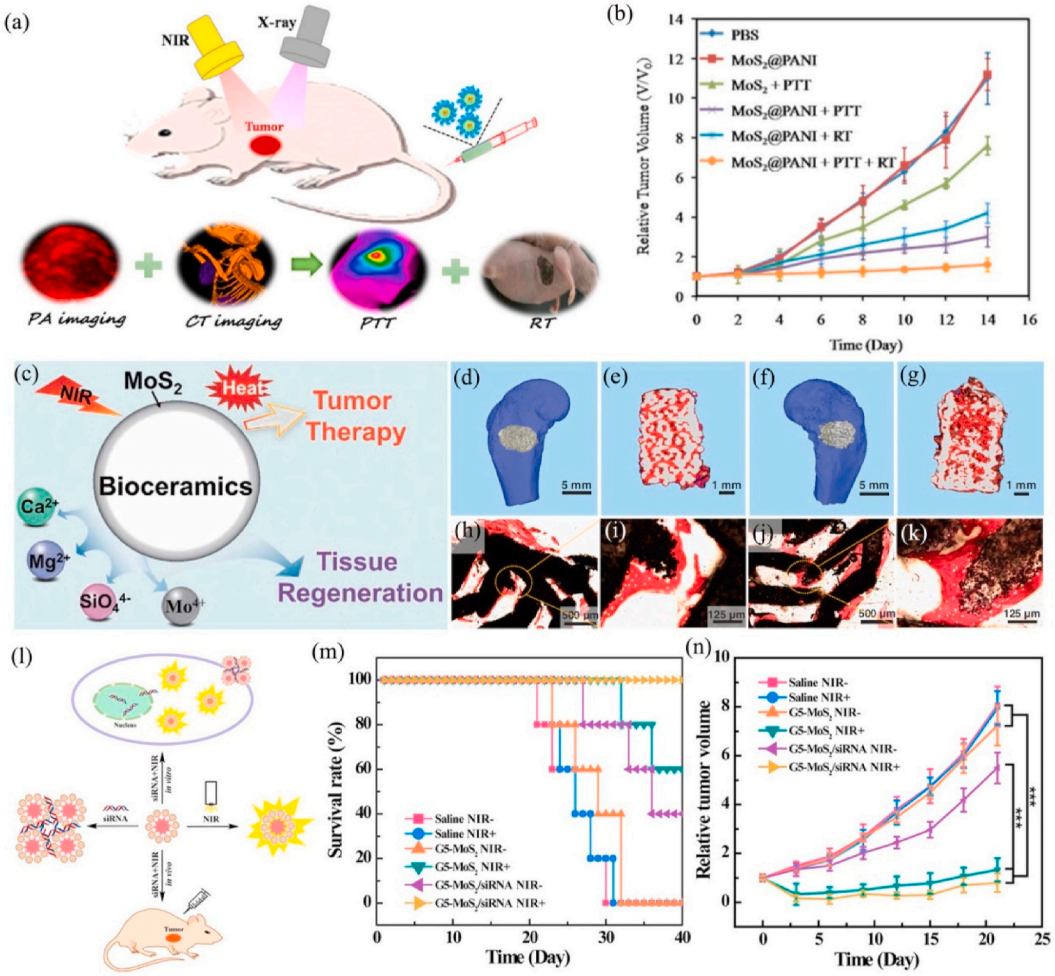

Fig. 17. (a) Scheme of MoS_2@PANI nanohybrids used for dual modal imaging and combined PTT and RT therapy. **(b)** Tumor growth in different groups of mice after various treatments. Reprinted with permission from Ref. [189]. Copyright 2016, ACS Applied Materials & Interfaces. **(c)** Schematic illustrations of the bifunctions of tumor therapy and tissue regeneration of MoS_2 nanosheets grew on 3D-printed bioceramic scaffolds. Micro-CT analysis for the bone regeneration after implanting with MoS_2-modified akermanite (MS-AKT) **(d), (e)** and AKT **(f), (g)** scaffolds in the critical-sized femoral defects of rabbits for 8 weeks. Red color stands for the formation of new bone **(e), (g)**. Histological analysis of MS-AKT **(h), (i)** and AKT **(j), (k)** scaffolds by Van Gieson staining after implanting for 8 weeks. Reprinted with permission from Ref. [346]. Copyright 2017, NPG Asia Materials. **(l)** Schematic illustrations of G5-MoS_2/Bcl-2 siRNA used for the gene therapy and PTT. **(m)** Survival rate of the tumor-bearing mice after different treatments at different time periods and **(n)** relative tumor volume. Reprinted with permission from Ref. [363]. Copyright 2017, ACS Applied Materials & Interfaces.

nanomaterial to strengthen the stability of MoS_2 in serum and positive charge amino end of PEI could promote the combination of MoS_2-PEG-PEI and siRNA due to the electrostatic interaction. The expression of PLK1 was significantly decreased and the flow cytometry analysis demonstrated that the number of apoptotic cells were increased markedly when HepG2 cells treated by MoS_2-PEG-PEI/siPLK1. Pancreatic carcinoma usually has properties including a very poor prognosis and a high mortality rate. Therapeutic effects of pancreatic carcinoma are mainly suppressed by the high molecular heterogeneity and surrounding stromal and inflammatory components [353–356]. Combination therapy of GT and PTT could improve the therapeutic effect and prolong survival of pancreatic cancer patients. Histone deacetylase 1 (HDAC1) and the mutational KRAS gene both promote the development of pancreatic cancers by regulating cell survival, transformation, invasion, and metastasis [357–360]. Yin et al. [361] designed a multi-gene delivery nanoplatform based on MoS_2 (MoS_2/LA/PEG/FA/PAH) for co-delivering HDAC1 and KRAS siRNAs into pancreatic tumor cells. FA-PEG polymers and polyallylamine hydrochloride (PAH) were used to functionalize the surface of MoS_2 nanosheets, which was conducive MoS_2/LA/PEG/FA/PAH to bond with siRNA and internalize by Panc-1 cells. The growth rate of Panc-1 cells and tumor volume was decreased by 70% and 80% respectively thanks to the synergistic effect of GT and PTT. By targeting antiapoptotic B-cell lymphoma-2 (Bcl-2) that overexpresses on tumor cells [362]. Kong et al. [363] synthesized dendrimer-modified MoS_2 nanosheets as carriers to condense Bcl-2 siRNA, realizing combination therapy of gene silencing and PTT. The results indicated that G5-MoS_2/siRNA polyplexes with the hydrodynamic size (300 nm) and positive surface potential could be used to deliver siRNA. Meanwhile, the inhibition rate of G5-MoS_2/Bcl-2 siRNA polyplexes on the expression of Bcl-2 gene was 47.3%. Under 808 nm NIR laser radiation, the survival rate of cells treated with G5-MoS_2/Bcl-2 siRNA complex was only 21.0%, which is much lower than PTT (45.8%) or GT (68.7%) alone (Fig. 17 l-n). In conclusion, MoS_2-based nanocomposites could effectively load siRNAs of specific genes which overexpressed in a variety of cancer cells and successfully delivered them to tumor cells, inhibiting the proliferation and migration of cancer cells to delay cancer progression through synergistic effect of GT and PTT.

Tumor immunotherapy aims to activate the immune system of the body and kill tumor cells via the immune reaction, and is emerging as a promising anti-tumor strategy [364]. Cytosine-phosphate-guanine (CpG) can be absorbed by lysosomes, inducing the generation of innate immune responses characterized by Th1 cells and

proinflammatory factors [365]. However, CpG is difficult to penetrate cell membranes and easily degraded by nucleases. Therefore, an ideal vector is needed to transport CpG to target cells and protect them from degradation. Han et al. [366] designed a uniform MoS_2-PEG-CpG for photothermal enhanced immunotherapy. First, the few-layered MoS_2 nanosheets obtained from bulk MoS_2 via Li ion intercalation and ultrasonication. Then SH-PEG and CpG modified MoS_2 nanosheets through the Mo–S bond. Importantly, MoS_2-PEG-CpG with uniform morphology had a mean diameter of 100 nm after probe sonication and modification, which more applicable to immune response. The enhanced immune response could be attributed to two aspects: (1) MoS_2-mediated photothermal effect enhanced the permeability of the cell membrane, promoting the endocytosis of MoS_2-PEG-CpG; (2) MoS_2-PEG-CpG could protect CpG from degradation by nucleases. Therefore, the production of pro-inflammatory factors and Th1 cells could be induced by increasing the uptake of CpG under near-infrared irradiation, realizing a stronger anti-cancer effect.

Chemodynamic therapy (CDT) uses the weakly acidic microenvironment of the tumor as the reaction conditions, H_2O_2 as the reaction raw material, and nanomaterials with enzyme-like activity as the catalyst. Therefore, it can induce Fenton or Fenton-like reactions in tumor cells to reduce H_2O_2 to ROS with strong oxidizing property, promoting cancer cell apoptosis [367]. MoS_2 nanosheets have a peroxidase-like activity (POD) that can detect H_2O_2 and glucose in serum [368]. Maji et al. [369] designed hybrid gold nanobipyramid nanocomposites coated with MoS_2 (AuNBPs@MoS_2) that possessed enzymes-like activity and could be used for anticancer treatment and TPF bioimaging. The AuNBPs@MoS_2 possessed significantly localized surface plasmon resonance (LSPR) performance under excitation ascribing to its anisotropic nature and the rich electron density in MoS_2. Meanwhile, the peroxidase-like activity of AuNBPs@MoS_2 could further heighten in the presence of TMB and H_2O_2 that due to LSPR speciality, leading to in situ photogeneration of ROS. TPF imaging demonstrated that AuNBPs@MoS_2 was endocytosed into tumor cells, and synergistic treatment of CDT and PTT was achieved in the presence of H_2O_2 and NIR laser irradiation, which promoted cancer cells death. Similarly, Mei et al. [370] synthesized MoS_2@CGTC NCR by co-loading tirapazamine (TPZ) and glucose oxidase (GOx) on the surface of MoS_2 for combination therapy of CDT and chemotherapy. First, GOx could catalyze glucose to generate H_2O_2 and gluconic acid, which could promote the reduction reaction between MoS_2 and H_2O_2 to produce a great deal of ·OH. MoS_2 also could react with GSH to decrease the consumption of ·OH. Second, TPZ could convert into toxic TPZ radical under hypoxia conditions to kill cancer cells. MoS_2@CGTC NCR could effectively ablate A549 cells in vivo and in vitro. Recently, copper ions and iron ions have been incorporated into MoS_2 to enhance the CDT effect of MoS_2 [371,372]. For example, Jiang et al. [373] prepared MoS_2–CuO heterostructures to promote the generation of ·OH by inducing Fenton or Fenton-like reactions.

To further strengthen the anticancer effect, Zhang et al. [374] integrated immunotherapy, CDT, and PTT into a platform ($FePt/MoS_2$--FA-CpG ODN), eliminating tumor and prevent tumor recurrence. The multipurpose $FePt/MoS_2$-FA nanocomplexes were constructed by immobilizing FePt nanoparticles (FPMF NCs) and FA on MoS_2 nanosheets. FePt nanoparticles used as competent iron death agents to catalyze Fenton reaction for generating ROS, and MoS_2 nanosheets could ablate primary tumor cells by PTT. Furthermore, oligodeoxynucleotides containing cytosine-guanine (CpG ODNs) anchored on the surface of MoS_2 nanosheets could strengthen the body's immune reaction to antigens, which combined with systemic checkpoint blockade therapy using an anti-CTLA4 antibody could effectively eliminate the metastatic tumor. At the same time, the combination of CpG ODNs and Toll-like receptor-9 (TLR9) could up-regulate the expression of co-stimulatory factors, promote the secretion of inflammatory factors, and enhance the immune response of $CD8^+$ T cells. Compared with FA receptor-negative L02 cells, FA receptor-positive 4T1 cells had a lower survival rate, indicating that $FePt/MoS_2$-FA-CpG ODN had a strong targeting ability, which could effectively kill cancer cells and inhibit tumor growth. What's more impressive was that this synergistic treatment had obtained a strong immune memory, thereby inhibiting cancer recurrence (Fig. 18). Phototherapy could trigger body's immune response to improve the effectiveness of cancer therapies [259,375–377]. Cancer cells were destroyed by phototherapy and then released tumor associated antigens which can be captured by antigen presenting cells (particularly dendritic cells, DCs) and presented to T cells, subsequently inducing immune reactions to kills tumor cells. Jin et al. [377] synthesized an injectable $PC_{10}A/DOX/MoS_2$ hydrogel that could be used for chemotherapy, phototherapy and immunotherapy of 4T1 tumor. MoS_2 nanosheet loaded with positively charged DOX and negatively charged $PC_{10}A$ to form hybrid $PC_{10}A/DOX/MoS_2$ nanoparticles by electrostatic interaction and then dispersed them in $PC_{10}A$ hydrogel to prepare the multifunctional $PC_{10}A/DOX/MoS_2$ hydrogel. MoS_2 nanosheets were used as efficient PTT agents and PDT agents to generate hyperthermia and ROS, respectively. Meanwhile, the secretion of immune-stimulatory cytokines would increase when PDT and PTT could promote the maturation of DCs, which was contributed to the activation of T cells. The result showed that the number of mDCs, $CD4^+$ T cell, $CD8^+$ T cell, and immune-stimulatory cytokines was significantly increased and the anti-cancer effect was remarkably enhanced due to the combination of chemotherapy, phototherapy and immunotherapy.

8. Conclusions and perspectives

Efficient and reliable cancer diagnosis and treatment methods can extend the survival period of patients and improve the quality of life [385]. Two-dimensional nanomaterials (MoS_2, $MoSe_2$, WS_2, WSe_2, and etc.) have attracted great interest in the biomedical field [8,18,386–397], especially MoS_2-based nanocomposites due to their outstanding physi-chemical properties and good biocompatibility. MoS_2 with a large specific surface area can load various biomolecules, drugs, fluorescent molecules, and other nanomaterials to improve its colloidal stability and tumor targeting, increase its sensitivity and accuracy in detecting specific biomarkers, and enhance its specific response to the stimulation of tumor microenvironment, which reduces side effects during treatment. At the same time, the strong photothermal conversion capacity and near-infrared light absorption ability of MoS_2 have promoted its application in phototherapy, PA imaging. Moreover, MoS_2--nanocomposites can be used for bioimaging, microwave hyperthermia, radiation therapy, immunotherapy, and combination therapy. However, most the research of MoS_2-nanocomposites for cancer diagnosis and treatment are still at an early stage, and there are still many problems to be solved [16].

Firstly, the long-term safety of MoS_2-nanocomposites in biomedical applications needs to be considered. Most experiments in vivo are limited to animal models, and only the short-term effects of these nanocomplexes on animal major organs, hematological indexes and blood biochemical indexes have been tested. Whether their long-term toxicity and efficacy in humans are consistent with the results of animal models has not been confirmed [398]. Quantum size effects and surface effects of MoS_2-nanocomposites may cause toxicity or enhance toxicity in organisms. MoS_2-nanocomposite may interact with channel proteins and various receptors on the surface of the cell membrane or inside the cell, resulting in conformational changes of proteins, changing of signal transduction pathways, and leading to dysfunction of the body. At present, there is no research to prove whether nanomaterials can interfere with the reproductive system and affect offspring [394]. In summary, the realization of clinical transformation of nanomaterials still faces great challenges, and more efforts are needed to fully demonstrate their long-term bio-safety.

Additionally, the bioavailability of MoS_2-nanocomposites in human tumor sites should be considered. It is very important to design MoS_2-nanomedicines that can specifically respond to the tumor

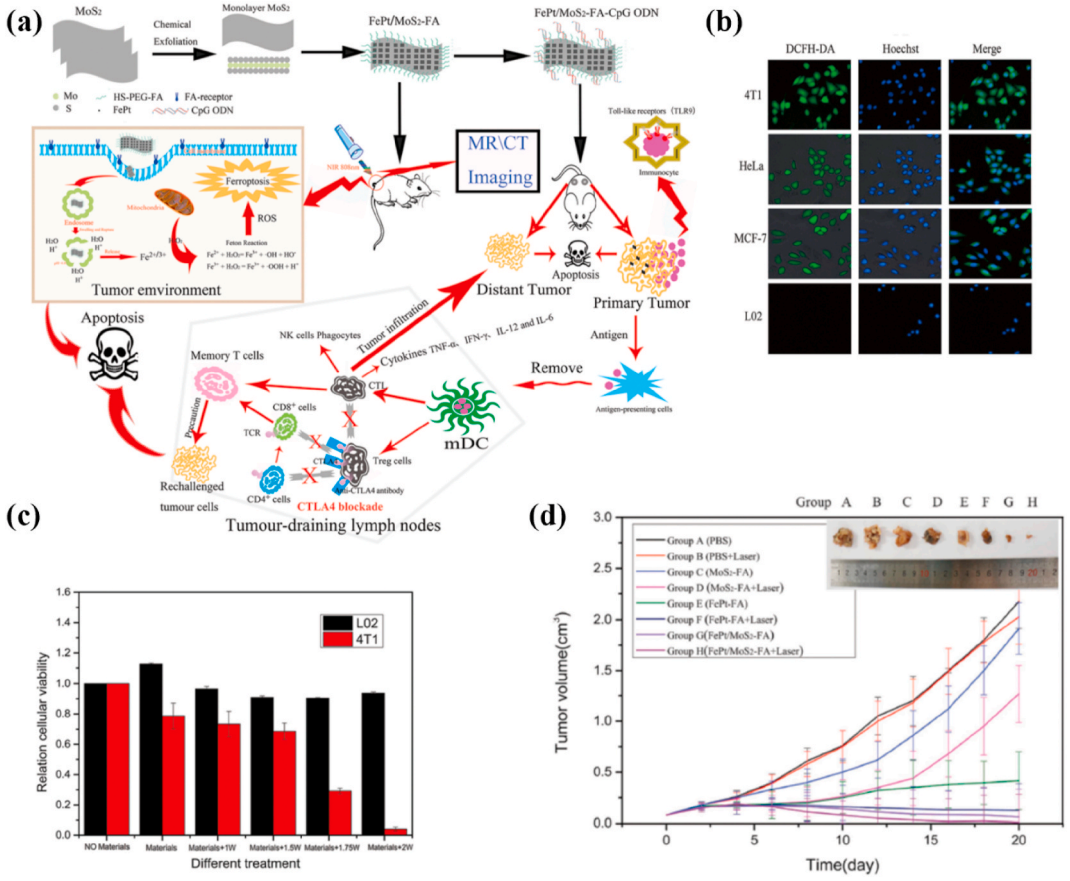

Fig. 18. (a) The fabrication process of FPMF nanocomposites and the mechanism of anti-tumor immune responses by FPMF@CpG ODN nanocomposites by combining immunotherapy, CDT, and PTT for anticancer therapeutic applications. **(b)** Fluorescence microscopy images of DCFH-DA labeled 4T1, HeLa, MCF-7 and L02 cells incubated with FPMF NPs for 6 h at the Fe concentration of 80 mg/mL. **(c)** Viabilities of 4T1 and L02 cells treated with different times at the same Fe concentration of 80 mg/mL. **(d)** The volume of tumors in tumor-bearing mice during different treatments. (Group: A: PBS, B: PBS + laser, C: MoS_2-FA, D: MoS_2-FA + laser, E: FePt-FA, F: FePt-FA + laser, G: FePt/MoS_2-FA, and H: FePt/MoS_2-FA + laser, n = 5). Reprinted with permission from Ref. [374]. Copyright 2019, Nanoscale.

microenvironment to enhance efficacy. For example, designing nanomaterials that can selectively bind to tumor cell-specific receptors to increase their accumulation in tumor sites and reduce the uptake of non-cancerous tissues. The rapidly established mouse orthotopic tumor model has an obvious EPR effect. However, the cancer progression and growth rate of many patients is much lower than that of mouse models, resulting in the patients' EPR effect is not obvious. Therefore, the uptake of nanomaterials through the EPR effect may not be suitable for the cancer patients. It is necessary to synthesize nanomaterials that can enter human tumor sites through other effects for improving their bioavailability in the human body.

Finally, synthesis of MoS_2-nanocomposites with stable performance is another challenge. On the one hand, the size and thickness are the key factors that affect the physicochemical property of MoS_2. Although there are existing methods to adjust the size and thickness of MoS_2, the cost is expensive, the operation steps are cumbersome and the morphology of MoS_2 will be affected. Therefore, exploring a simple and easy synthesis method can not only reduce costs, but also better optimize the properties of MoS_2 and improve its therapeutic effect. On the other hand, excellent stability is a necessary condition for nanomedicines to achieve clinical transformation. Therefore, it is urgent to optimize experimental methods to improve the stability of nanomaterials, prolonging their storage time and promoting clinical transformation.

Declaration of competing interest

The authors declare no conflict of interest, financial or otherwise.

Acknowledgements

This work was supported by the National Natural Science Foundation of China, China (No.21974134, 81974508, 81673492, 81873581) and Innovation-Driven Project of Central South University (No. 202045005), Changsha Science and Technology Project (No. kq2001048).

References

[1] F. Bray, J. Ferlay, I. Soerjomataram, R.L. Siegel, L.A. Torre, A. Jemal, Global cancer statistics 2018: GLOBOCAN estimates of incidence and mortality worldwide for 36 cancers in 185 countries, CA A Cancer J. Clin. 68 (6) (2018) 394–424.

[2] Z. Lu, Z. Peng, C. Liu, Z. Wang, Y. Wang, X. Jiao, J. Li, L. Shen, Current status and future perspective of immunotherapy in gastrointestinal cancers, Innovation 1 (2) (2020) 100041.

[3] J. Ferlay, M. Colombet, I. Soerjomataram, C. Mathers, D.M. Parkin, Estimating the global cancer incidence and mortality in 2018: GLOBOCAN sources and methods, 144, 2019, pp. 1941–1953, 8.

[4] Y. Hu, S. Mignani, J.P. Majoral, M. Shen, X. Shi, Construction of iron oxide nanoparticle-based hybrid platforms for tumor imaging and therapy, Chem. Soc. Rev. 47 (5) (2018) 1874–1900.

[5] Z. Wang, R. Qiao, N. Tang, Z. Lu, H. Wang, Z. Zhang, X. Xue, Z. Huang, S. Zhang, G. Zhang, Y. Li, Active targeting theranostic iron oxide nanoparticles for MRI and magnetic resonance-guided focused ultrasound ablation of lung cancer, Biomaterials 127 (2017) 25–35.

[6] T. Liu, Z. Liu, 2D MoS2 nanostructures for biomedical applications, Advanced healthcare materials 7 (8) (2018), e1701158.

[7] J. Lu, M. Chen, L. Dong, L. Cai, M. Zhao, Q. Wang, J. Li, Molybdenum disulfide nanosheets: from exfoliation preparation to biosensing and cancer therapy applications, Colloids Surf. B Biointerfaces 194 (2020) 111162.

[8] V. Yadav, S. Roy, P. Singh, Z. Khan, A. Jaiswal, 2D MoS(2) -based nanomaterials for therapeutic, Bioimaging, and Biosensing Applications 15 (1) (2019), e1803706.
[9] N. Dhas, R. Kudarha, A. Garkal, V. Ghate, S. Sharma, P. Panzade, S. Khot, P. Chaudhari, A. Singh, M. Paryani, S. Lewis, N. Garg, N. Singh, P. Bangar, T. Mehta, Molybdenum-based hetero-nanocomposites for cancer therapy, diagnosis and biosensing application: current advancement and future breakthroughs, J. Contr. Release : official journal of the Controlled Release Society 330 (2020) 257–283.
[10] G. Schwarz, A.A. Belaidi, Molybdenum in human health and disease, Metal ions in life sciences 13 (2013) 415–450.
[11] R.R. Mendel, Cell biology of molybdenum, Biofactors 35 (5) (2009) 429–434.
[12] E.S. Kadantsev, P. Hawrylak, Electronic structure of a single MoS2 monolayer, Solid State Commun. 152 (10) (2012) 909–913.
[13] K. Bazaka, I. Levchenko, J.W.M. Lim, O. Baranov, C. Corbella, S. Xu, M. Keidar, MoS2-based nanostructures: synthesis and applications in medicine, J. Phys. Appl. Phys. 52 (18) (2019) 183001.
[14] B. Radisavljevic, A. Radenovic, J. Brivio, V. Giacometti, A. Kis, Single-layer MoS2 transistors, Nat. Nanotechnol. 6 (3) (2011) 147–150.
[15] Q.H. Wang, K. Kalantar-Zadeh, A. Kis, J.N. Coleman, M.S. Strano, Electronics and optoelectronics of two-dimensional transition metal dichalcogenides, Nat. Nanotechnol. 7 (11) (2012) 699–712.
[16] Y. Chen, C. Tan, H. Zhang, L. Wang, Two-dimensional graphene analogues for biomedical applications, Chem. Soc. Rev. 44 (9) (2015) 2681–2701.
[17] H. Peng, W. Dang, J. Cao, Y. Chen, D. Wu, W. Zheng, H. Li, Z.X. Shen, Z. Liu, Topological insulator nanostructures for near-infrared transparent flexible electrodes, Nat. Chem. 4 (4) (2012) 281–286.
[18] D.K. Ji, C. Ménard-Moyon, A. Bianco, Physically-triggered nanosystems based on two-dimensional materials for cancer theranostics, Adv. Drug Deliv. Rev. 138 (2019) 211–232.
[19] S.S. Chou, B. Kaehr, J. Kim, B.M. Foley, M. De, P.E. Hopkins, J. Huang, C. J. Brinker, V.P. Dravid, Chemically exfoliated MoS2 as near-infrared photothermal agents, Angew. Chem. 52 (15) (2013) 4160–4164.
[20] C. Zhu, Z. Zeng, H. Li, F. Li, C. Fan, H. Zhang, Single-layer MoS2-based nanoprobes for homogeneous detection of biomolecules, J. Am. Chem. Soc. 135 (16) (2013) 5998–6001.
[21] J.Z. Ou, A.F. Chrimes, Y. Wang, S.Y. Tang, M.S. Strano, K. Kalantar-zadeh, Ion-driven photoluminescence modulation of quasi-two-dimensional MoS2 nanoflakes for applications in biological systems, Nano Lett. 14 (2) (2014) 857–863.
[22] W.Z. Teo, E.L. Chng, Z. Sofer, M. Pumera, Cytotoxicity of exfoliated transition-metal dichalcogenides (MoS2 , WS2 , and WSe2) is lower than that of graphene and its analogues, Chemistry 20 (31) (2014) 9627–9632.
[23] A. Splendiani, L. Sun, Y. Zhang, T. Li, J. Kim, C.Y. Chim, G. Galli, F. Wang, Emerging photoluminescence in monolayer MoS2, Nano Lett. 10 (4) (2010) 1271–1275.
[24] D. Deng, K.S. Novoselov, Q. Fu, N. Zheng, Z. Tian, X. Bao, Catalysis with two-dimensional materials and their heterostructures, Nat. Nanotechnol. 11 (3) (2016) 218–230.
[25] A. Jayakumar, A. Surendranath, M. Pv, 2D materials for next generation healthcare applications, Int. J. Pharm. 551 (1–2) (2018) 309–321.
[26] P. Chen, D. Pan, C. Fan, J. Chen, K. Huang, D. Wang, H. Zhang, Y. Li, G. Feng, P. Liang, L. He, Y. Shi, Gold nanoparticles for high-throughput genotyping of long-range haplotypes, Nat. Nanotechnol. 6 (10) (2011) 639–644.
[27] Y. Wen, H. Pei, Y. Shen, J. Xi, M. Lin, N. Lu, X. Shen, J. Li, C. Fan, DNA Nanostructure-based Interfacial engineering for PCR-free ultrasensitive electrochemical analysis of microRNA, Sci. Rep. 2 (2012) 867.
[28] A.S. Krishna Kumar, W.B. Tseng, M.J. Wu, Y.Y. Huang, W.L. Tseng, L-cystine-linked BODIPY-adsorbed monolayer MoS2 quantum dots for ratiometric fluorescent sensing of biothiols based on the inner filter effect, Anal. Chim. Acta 1113 (2020) 43–51.
[29] Y. Wan, W. Deng, Y. Su, X. Zhu, C. Peng, H. Hu, H. Peng, S. Song, C. Fan, Carbon nanotube-based ultrasensitive multiplexing electrochemical immunosensor for cancer biomarkers, Biosens. Bioelectron. 30 (1) (2011) 93–99.
[30] D.R. Thévenot, K. Toth, R.A. Durst, G.S. Wilson, Electrochemical biosensors: recommended definitions and classification, Biosens. Bioelectron. 16 (1–2) (2001) 121–131.
[31] A.M. Ward, J.W. Catto, F.C. Hamdy, Prostate specific antigen: biology, biochemistry and available commercial assays, Ann. Clin. Biochem. 38 (Pt 6) (2001) 633–651.
[32] B.E. Rapp, F.J. Gruhl, K. Länge, Biosensors with label-free detection designed for diagnostic applications, Anal. Bioanal. Chem. 398 (6) (2010) 2403–2412.
[33] W. Yang, K.R. Ratinac, S.P. Ringer, P. Thordarson, J.J. Gooding, F. Braet, Carbon nanomaterials in biosensors: should you use nanotubes or graphene? Angew. Chem. 49 (12) (2010) 2114–2138.
[34] Y. Cui, Q. Wei, H. Park, C.M. Lieber, Nanowire nanosensors for highly sensitive and selective detection of biological and chemical species, Science (New York, N. Y.). 293 (5533) (2001) 1289–1292.
[35] K. Lee, P.R. Nair, A. Scott, M.A. Alam, D.B. Janes, Device considerations for development of conductance-based biosensors, J. Appl. Phys. 105 (10) (2009) 102046.
[36] R. Coehoorn, C. Haas, J. Dijkstra, C.J. Flipse, R.A. de Groot, A. Wold, Electronic structure of MoSe2, MoS2, and WSe2. I. Band-structure calculations and photoelectron spectroscopy, Phys. Rev. B 35 (12) (1987) 6195–6202.
[37] D. Sarkar, W. Liu, X. Xie, A.C. Anselmo, S. Mitragotri, K. Banerjee, MoS_2 field-effect transistor for next-generation label-free biosensors, ACS Nano 8 (4) (2014) 3992–4003.
[38] L. Wang, Y. Wang, J.I. Wong, T. Palacios, J. Kong, H.Y. Yang, Functionalized MoS (2) nanosheet-based field-effect biosensor for label-free sensitive detection of cancer marker proteins in solution, Small 10 (6) (2014) 1101–1105.
[39] J. Zheng, H. Zhang, S. Dong, Y. Liu, C.T. Nai, H.S. Shin, H.Y. Jeong, B. Liu, K. P. Loh, High yield exfoliation of two-dimensional chalcogenides using sodium naphthalenide, Nat. Commun. 5 (2014) 2995.
[40] H. Feng, Z. Hu, X. Liu, Facile and efficient exfoliation of inorganic layered materials using liquid alkali metal alloys, Chem. Commun. 51 (54) (2015) 10961–10964.
[41] M. Kukkar, S.K. Tuteja, A.L. Sharma, V. Kumar, A.K. Paul, K.H. Kim, P. Sabherwal, A. Deep, A new electrolytic synthesis method for few-layered MoS2 nanosheets and their robust biointerfacing with reduced antibodies, ACS Appl. Mater. Interfaces 8 (26) (2016) 16555–16563.
[42] H. Park, G. Han, S.W. Lee, H. Lee, S.H. Jeong, M. Naqi, A. AlMutairi, Y.J. Kim, J. Lee, W.J. Kim, S. Kim, Y. Yoon, G. Yoo, Label-free and recalibrated multilayer MoS2 biosensor for point-of-care diagnostics, ACS Appl. Mater. Interfaces 9 (50) (2017) 43490–43497.
[43] J. Wang, Electrochemical biosensors: towards point-of-care cancer diagnostics, Biosens. Bioelectron. 21 (10) (2006) 1887–1892.
[44] G. Yoo, H. Park, M. Kim, W.G. Song, S. Jeong, M.H. Kim, H. Lee, S.W. Lee, Y. K. Hong, M.G. Lee, S. Lee, S. Kim, Real-time electrical detection of epidermal skin MoS2 biosensor for point-of-care diagnostics, Nano Research 10 (3) (2016) 767–775.
[45] Y. Yang, B. Zeng, Y. Li, H. Liang, Y. Yang, Q. Yuan, Construction of MoS2 field effect transistor sensor array for the detection of bladder cancer biomarkers, Sci. China Chem. 63 (7) (2020) 997–1003.
[46] F. Ma, Y. Li, B. Tang, C.Y. Zhang, Fluorescent biosensors based on single-molecule counting, Accounts Chem. Res. 49 (9) (2016) 1722–1730.
[47] M.K. Tsang, W. Ye, G. Wang, J. Li, M. Yang, J. Hao, Ultrasensitive detection of ebola virus oligonucleotide based on upconversion nanoprobe/nanoporous membrane system, ACS Nano 10 (1) (2016) 598–605.
[48] F. Tian, J. Lyu, J. Shi, M. Yang, Graphene and graphene-like two-denominational materials based fluorescence resonance energy transfer (FRET) assays for biological applications, Biosens. Bioelectron. 89 (Pt 1) (2017) 123–135.
[49] D.W. Hwang, H.Y. Kim, F. Li, J.Y. Park, D. Kim, J.H. Park, H.S. Han, J.W. Byun, Y. S. Lee, J.M. Jeong, K. Char, D.S. Lee, In vivo visualization of endogenous miR-21 using hyaluronic acid-coated graphene oxide for targeted cancer therapy, Biomaterials 121 (2017) 144–154.
[50] H. Dong, J. Lei, L. Ding, Y. Wen, H. Ju, X. Zhang, MicroRNA: function, detection, and bioanalysis, Chem. Rev. 113 (8) (2013) 6207–6233.
[51] R.M. Graybill, R.C. Bailey, Emerging biosensing approaches for microRNA analysis, Anal. Chem. 88 (1) (2016) 431–450.
[52] S.W. Kim, Z. Li, P.S. Moore, A.P. Monaghan, Y. Chang, M. Nichols, B. John, A sensitive non-radioactive northern blot method to detect small RNAs, Nucleic Acids Res. 38 (7) (2010) e98.
[53] T. Tian, J. Wang, X. Zhou, A review: microRNA detection methods, Org. Biomol. Chem. 13 (8) (2015) 2226–2238.
[54] Z. Gao, H. Yuan, Y. Mao, L. Ding, C.Y. Effah, S. He, L. He, L.E. Liu, S. Yu, Y. Wang, J. Wang, Y. Tian, F. Yu, H. Guo, L. Miao, L. Qu, Y. Wu, In situ detection of plasma exosomal microRNA for lung cancer diagnosis using duplex-specific nuclease and MoS2 nanosheets, Analyst 146 (6) (2021) 1924–1931.
[55] R. Zhang, C. Xia, X. Zhou, Y. Guo, W. Li, Molybdenum disulfide nanomaterial sensor-based detection of breast cancer microRNA, Materials Express 10 (6) (2020) 915–921.
[56] M. Xiao, A.R. Chandrasekaran, W. Ji, F. Li, T. Man, C. Zhu, X. Shen, H. Pei, Q. Li, L. Li, Affinity-Modulated molecular beacons on MoS2 nanosheets for MicroRNA detection, ACS Appl. Mater. Interfaces 10 (42) (2018) 35794–35800.
[57] C. Lu, Y. Liu, Y. Ying, Comparison of MoS(2), WS(2), and Graphene Oxide for DNA Adsorption and Sensing, 33, 2017, pp. 630–637, 2.
[58] X. Qu, D. Zhu, G. Yao, S. Su, J. Chao, H. Liu, X. Zuo, L. Wang, J. Shi, L. Wang, W. Huang, H. Pei, C. Fan, An exonuclease III-powered, On-Particle Stochastic DNA Walker 56 (7) (2017) 1855–1858.
[59] G. Oudeng, M. Au, J. Shi, C. Wen, M. Yang, One-step in situ detection of miRNA-21 expression in single cancer cells based on biofunctionalized MoS2 nanosheets, ACS Appl. Mater. Interfaces 10 (1) (2018) 350–360.
[60] R. Deng, K. Zhang, J. Li, Isothermal amplification for MicroRNA detection: from the test tube to the, Cell 50 (4) (2017) 1059–1068.
[61] Z.M. Ying, Z. Wu, B. Tu, W. Tan, Genetically encoded fluorescent RNA sensor for ratiometric imaging of MicroRNA in living tumor cells 139 (29) (2017) 9779–9782.
[62] D. Zhu, J. Huang, B. Lu, Y. Zhu, Y. Wei, Q. Zhang, X. Guo, L. Yuwen, S. Su, J. Chao, L. Wang, Intracellular MicroRNA imaging with MoS2-supported nonenzymatic catassembly of DNA hairpins, ACS Appl. Mater. Interfaces 11 (23) (2019) 20725–20733.
[63] C.H. Park, S. Lee, G. Pornnoppadol, Y.S. Nam, S.H. Kim, B.J. Kim, Microcapsules containing pH-responsive, fluorescent polymer-integrated MoS2: an effective platform for in situ pH sensing and photothermal heating, ACS Appl. Mater. Interfaces 10 (10) (2018) 9023–9031.
[64] L.E. Gerweck, K. Seetharaman, Cellular pH gradient in tumor versus normal tissue: potential exploitation for the treatment of cancer, Canc. Res. 56 (6) (1996) 1194–1198.
[65] F. Su, S. Agarwal, T. Pan, Y. Qiao, L. Zhang, Z. Shi, X. Kong, K. Day, M. Chen, D. Meldrum, V.D. Kodibagkar, Y. Tian, Multifunctional PHPMA-derived polymer

for ratiometric pH sensing, Fluorescence Imaging, and Magnetic Resonance Imaging 10 (2) (2018) 1556–1565.
[66] K. Paek, H. Yang, J. Lee, J. Park, B.J. Kim, Efficient colorimetric pH sensor based on responsive polymer-quantum dot integrated graphene oxide, ACS Nano 8 (3) (2014) 2848–2856.
[67] C. Li, Y. Zhang, J. Hu, J. Cheng, S. Liu, Reversible three-state switching of multicolor fluorescence emission by multiple stimuli modulated FRET processes within thermoresponsive polymeric micelles, Angew. Chem. 49 (30) (2010) 5120–5124.
[68] T. Liu, C. Wang, X. Gu, H. Gong, L. Cheng, X. Shi, L. Feng, B. Sun, Z. Liu, Drug delivery with PEGylated MoS2 nano-sheets for combined photothermal and chemotherapy of cancer, Adv. Mater. 26 (21) (2014) 3433–3440.
[69] X. Chen, A.R. McDonald, Functionalization of two-dimensional transition-metal dichalcogenides, Adv. Mater. 28 (27) (2016) 5738–5746.
[70] P.A. Baeuerle, O. Gires, EpCAM (CD326) finding its role in cancer, Br. J. Canc. 96 (3) (2007) 417–423.
[71] P. Dalerba, S.J. Dylla, I.K. Park, R. Liu, X. Wang, R.W. Cho, T. Hoey, A. Gurney, E. H. Huang, D.M. Simeone, A.A. Shelton, G. Parmiani, C. Castelli, M.F. Clarke, Phenotypic characterization of human colorectal cancer stem cells, Proc. Natl. Acad. Sci. U. S. A 104 (24) (2007) 10158–10163.
[72] T. Yamashita, J. Ji, A. Budhu, M. Forgues, W. Yang, H.Y. Wang, H. Jia, Q. Ye, L. X. Qin, E. Wauthier, L.M. Reid, H. Minato, M. Honda, S. Kaneko, Z.Y. Tang, X. W. Wang, EpCAM-positive hepatocellular carcinoma cells are tumor-initiating cells with stem/progenitor cell features, Gastroenterology 136 (3) (2009) 1012–1024.
[73] A. Armstrong, S.L. Eck, EpCAM: a new therapeutic target for an old cancer antigen, Canc. Biol. Ther. 2 (4) (2003) 320–326.
[74] L.S. Schwartzberg, Clinical experience with edrecolomab: a monoclonal antibody therapy for colorectal carcinoma, Crit. Rev. Oncol.-Hematol. 40 (1) (2001) 17–24.
[75] Y. Song, Z. Zhu, Y. An, W. Zhang, H. Zhang, D. Liu, C. Yu, W. Duan, C.J. Yang, Selection of DNA aptamers against epithelial cell adhesion molecule for cancer cell imaging and circulating tumor cell capture, Anal. Chem. 85 (8) (2013) 4141–4149.
[76] D. Bhatnagar, V. Kumar, A. Kumar, I. Kaur, Graphene quantum dots FRET based sensor for early detection of heart attack in human, Biosens. Bioelectron. 79 (2016) 495–499.
[77] J. Shi, J. Lyu, F. Tian, M. Yang, A fluorescence turn-on biosensor based on graphene quantum dots (GQDs) and molybdenum disulfide (MoS2) nanosheets for epithelial cell adhesion molecule (EpCAM) detection, Biosens. Bioelectron. 93 (2017) 182–188.
[78] Y. Xu, Q. Kang, B. Yang, B. Chen, M. He, B. Hu, A nanoprobe based on molybdenum disulfide nanosheets and silver nanoclusters for imaging and quantification of intracellular adenosine triphosphate, Anal. Chim. Acta 1134 (2020) 75–83.
[79] L. Zhao, D. Kong, Z. Wu, G. Liu, Y. Gao, X. Yan, F. Liu, X. Liu, C. Wang, J. Cui, G. Lu, Interface interaction of MoS2 nanosheets with DNA based aptameric biosensor for carbohydrate antigen 15–3 detection, Microchem. J. 155 (2020) 104675.
[80] T. Wang, H. Zhu, J. Zhuo, Z. Zhu, P. Papakonstantinou, G. Lubarsky, J. Lin, M. Li, Biosensor based on ultrasmall MoS2 nanoparticles for electrochemical detection of H2O2 released by cells at the nanomolar level, Anal. Chem. 85 (21) (2013) 10289–10295.
[81] P. Zhang, R. Li, Y. Huang, Q. Chen, A novel approach for the in situ synthesis of Pt-Pd nanoalloys supported on Fe3O4@C core-shell nanoparticles with enhanced catalytic activity for reduction reactions, ACS Appl. Mater. Interfaces 6 (4) (2014) 2671–2678.
[82] D.P. Li, X.Y. Liu, R. Yi, J.X. Zhang, Z.Q. Su, G. Wei, Electrochemical sensor based on novel two-dimensional nanohybrids: MoS2 nanosheets conjugated with organic copper nanowires for simultaneous detection of hydrogen peroxide and ascorbic acid, Inorg. Chem. Front. 5 (1) (2018) 112–119.
[83] D.M. Lin, Y. Li, P.P. Zhang, W.S. Zhang, J.W. Ding, J.F. Li, G. Wei, Z.Q. Su, Fast preparation of MoS2 nanoflowers decorated with platinum nanoparticles for electrochemical detection of hydrogen peroxide, RSC Adv. 6 (58) (2016) 52739–52745.
[84] T. Zhang, Y. Gu, C. Li, X. Yan, N. Lu, H. Liu, Z. Zhang, Fabrication of novel electrochemical biosensor based on graphene nanohybrid to detect H(2)O(2) released from living cells with ultrahigh Performance, 9, 2017, pp. 37991–37999, 43.
[85] J.G. Roberts, M.A. Voinov, A.C. Schmidt, T.I. Smirnova, L.A. Sombers, The hydroxyl radical is a critical intermediate in the voltammetric detection of hydrogen peroxide, J. Am. Chem. Soc. 138 (8) (2016) 2516–2519.
[86] B. Dou, J. Yang, R. Yuan, Y. Xiang, Trimetallic hybrid nanoflower-decorated MoS2 nanosheet sensor for direct in situ monitoring of H2O2 secreted from live cancer cells, Anal. Chem. 90 (9) (2018) 5945–5950.
[87] Y. Shu, W. Zhang, H. Cai, Y. Yang, X. Yu, Q. Gao, Expanding the interlayers of molybdenum disulfide toward the highly sensitive sensing of hydrogen peroxide, Nanoscale 11 (14) (2019) 6644–6653.
[88] Y. Shu, L. Zhang, H. Cai, Y. Yang, J. Zeng, D. Ma, Q. Gao, Hierarchical Mo2C@MoS2 nanorods as electrochemical sensors for highly sensitive detection of hydrogen peroxide and cancer cells, Sensor. Actuator. B Chem. 311 (2020) 127863.
[89] Y. Gou, Q. Liu, X. Shi, A.M. Asiri, J. Hu, X. Sun, CaMoO(4) nanosheet arrays for efficient and durable water oxidation electrocatalysis under alkaline conditions, Chem. Commun. 54 (40) (2018) 5066–5069.
[90] H. Du, X. Zhang, Z. Liu, F. Qu, A supersensitive biosensor based on MoS2 nanosheet arrays for the real-time detection of H2O2 secreted from living cells, Chem. Commun. 55 (65) (2019) 9653–9656.
[91] H. Yang, J. Zhou, J. Bao, Y. Ma, J. Zhou, C. Shen, H. Luo, M. Yang, C. Hou, D. Huo, A simple hydrothermal one-step synthesis of 3D-MoS2/rGO for the construction of sensitive enzyme-free hydrogen peroxide sensor, Microchem. J. 162 (2021) 105746.
[92] X. Wang, C. Chu, L. Shen, W. Deng, M. Yan, S. Ge, J. Yu, X. Song, An ultrasensitive electrochemical immunosensor based on the catalytical activity of MoS2-Au composite using Ag nanospheres as labels, Sensor. Actuator. B Chem. 206 (2015) 30–36.
[93] E. Ma, P. Wang, Q. Yang, H. Yu, F. Pei, Y. Li, Q. Liu, Y. Dong, Electrochemical immunosensor based on MoS2 NFs/Au@AgPt YNCs as signal amplification label for sensitive detection of CEA, Biosens. Bioelectron. 142 (2019) 111580.
[94] Y. Jia, Y. Li, S. Zhang, P. Wang, Q. Liu, Y. Dong, Mulberry-like Au@PtPd porous nanorods composites as signal amplifiers for sensitive detection of CEA, Biosens. Bioelectron. 149 (2020) 111842.
[95] Z. Farka, T. Jurík, D. Kovář, Nanoparticle-based immunochemical biosensors and assays, Recent Advances and Challenges 117 (15) (2017) 9973–10042.
[96] G. Peng, X. Li, F. Cui, Q. Qiu, X. Chen, Aflatoxin B1 electrochemical aptasensor based on tetrahedral DNA nanostructures functionalized three dimensionally ordered macroporous MoS(2)-AuNPs Film, 10, 2018, pp. 17551–17559, 21.
[97] Y. Song, W. Li, C. Ma, J. Qiao, H. Li, C. Hong, The synergistic effect of ferrocene and Cu2O to construct a sandwich-type multi-signal amplification ultra-sensitive immunosensor for carcinoembryonic antigen detection, J. Electrochem. Soc. 167 (2) (2020), 027538.
[98] T. Chen, A. Sheng, Y. Hu, D. Mao, L. Ning, J. Zhang, Modularization of three-dimensional gold nanoparticles/ferrocene/liposome cluster for electrochemical biosensor, Biosens. Bioelectron. 124–125 (2019) 115–121.
[99] Y. Yang, Q. Yan, Q. Liu, Y. Li, H. Liu, P. Wang, L. Chen, D. Zhang, Y. Li, Y. Dong, An ultrasensitive sandwich-type electrochemical immunosensor based on the signal amplification strategy of echinoidea-shaped Au@Ag-Cu(2)O nanoparticles for prostate specific antigen detection, Biosens. Bioelectron. 99 (2018) 450–457.
[100] S. Su, Q. Sun, L. Wan, X. Gu, D. Zhu, Y. Zhou, J. Chao, L. Wang, Ultrasensitive analysis of carcinoembryonic antigen based on MoS2-based electrochemical immunosensor with triple signal amplification, Biosens. Bioelectron. 140 (2019) 111353.
[101] C.B. Buck, D.R. Lowy, Immune readouts may have prognostic value for the course of merkel cell carcinoma, a virally associated disease, J. Clin. Oncol. : official journal of the American Society of Clinical Oncology 29 (12) (2011) 1506–1508.
[102] H.J. Yoon, M. Kozminsky, S. Nagrath, Emerging role of nanomaterials in circulating tumor cell isolation and analysis, ACS Nano 8 (3) (2014) 1995–2017.
[103] C.H. Wu, Y.Y. Huang, P. Chen, K. Hoshino, H. Liu, E.P. Frenkel, J.X. Zhang, K. V. Sokolov, Versatile immunomagnetic nanocarrier platform for capturing cancer cells, ACS Nano 7 (10) (2013) 8816–8823.
[104] S. Nagrath, L.V. Sequist, S. Maheswaran, D.W. Bell, D. Irimia, L. Ulkus, M. R. Smith, E.L. Kwak, S. Digumarthy, A. Muzikansky, P. Ryan, U.J. Balis, R. G. Tompkins, D.A. Haber, M. Toner, Isolation of rare circulating tumour cells in cancer patients by microchip technology, Nature 450 (7173) (2007) 1235–1239.
[105] W. He, H. Wang, L.C. Hartmann, J.X. Cheng, P.S. Low, In Vivo quantitation of rare circulating tumor cells by multiphoton intravital flow cytometry, Proc. Natl. Acad. Sci. U. S. A 104 (28) (2007) 11760–11765.
[106] J. Cao, X.P. Zhao, M.R. Younis, Z.Q. Li, X.H. Xia, Ultrasensitive capture, detection, and release of circulating tumor cells using a nanochannel-ion channel hybrid coupled with electrochemical detection technique, 89, 2017, pp. 10957–10964, 20.
[107] S. Guo, J. Xu, M. Xie, W. Huang, E. Yuan, Y. Liu, L. Fan, S. Cheng, S. Liu, F. Wang, B. Yuan, W. Dong, X. Zhang, W. Huang, X. Zhou, Degradable zinc-phosphate-based hierarchical nanosubstrates for capture and release of circulating tumor cells, ACS Appl. Mater. Interfaces 8 (25) (2016) 15917–15925.
[108] S.W. Lv, Y. Liu, M. Xie, J. Wang, X.W. Yan, Z. Li, W.G. Dong, W.H. Huang, Near-infrared light-responsive hydrogel for specific recognition and photothermal site-release of circulating tumor cells, ACS Nano 10 (6) (2016) 6201–6210.
[109] H.J. Hwang, M.Y. Ryu, C.Y. Park, J. Ahn, H.G. Park, C. Choi, S.D. Ha, T.J. Park, J. P. Park, High sensitive and selective electrochemical biosensor: label-free detection of human norovirus using affinity peptide as molecular binder, Biosens. Bioelectron. 87 (2017) 164–170.
[110] Y. Xu, X. Xie, Y. Duan, L. Wang, Z. Cheng, J. Cheng, A review of impedance measurements of whole cells, Biosens. Bioelectron. 77 (2016) 824–836.
[111] Y. Chen, J. Peng, Y. Lai, B. Wu, L. Sun, J. Weng, Ultrasensitive label-free detection of circulating tumor cells using conductivity matching of two-dimensional semiconductor with cancer cell, Biosens. Bioelectron. 142 (2019) 111520.
[112] W. Li, Z. Chen, L. Zhou, Z. Li, J. Ren, X. Qu, Noninvasive and reversible cell adhesion and detachment via single-wavelength near-infrared laser mediated photoisomerization, J. Am. Chem. Soc. 137 (25) (2015) 8199–8205.
[113] X. Wang, X. Wang, S. Cheng, M. Ye, C. Zhang, Y. Xian, Near-infrared light-switched MoS2 Nanoflakes@Gelatin bioplatform for capture, detection, and nondestructive release of circulating tumor cells, Anal. Chem. 92 (4) (2020) 3111–3117.
[114] M.K. Yazdi, E. Ghazizadeh, M. Noroozi, A. Neshastehriz, Design of a DOPC-MoS2/AuNP hybrid as an organic bed with higher amplification for miR detection in electrochemical biosensors, Anal. Bioanal. Chem. 412 (13) (2020) 3209–3219.
[115] L. Liu, K. Ma, X. Xu, C. Shangguan, J. Lv, S. Zhu, S. Jiao, J. Wang, MoS2-ReS2 heterojunctions from a bimetallic Co-chamber feeding atomic layer deposition for ultrasensitive MiRNA-21 detection, ACS Appl. Mater. Interfaces 12 (26) (2020) 29074–29084.

[116] A.K. Yagati, A. Go, N.H. Vu, M.-H. Lee, A MoS2–Au nanoparticle-modified immunosensor for T3 biomarker detection in clinical serum samples, Electrochim. Acta 342 (2020) 136065.
[117] M.L. Yola, N. Atar, N. Ozcan, A novel electrochemical lung cancer biomarker cytokeratin 19 fragment antigen 21-1 immunosensor based on Si3N4/MoS2 incorporated MWCNTs and core-shell type magnetic nanoparticles, Nanoscale 13 (8) (2021) 4660–4669.
[118] O. Jalil, C.M. Pandey, D. Kumar, Highly sensitive electrochemical detection of cancer biomarker based on anti-EpCAM conjugated molybdenum disulfide grafted reduced graphene oxide nanohybrid, Bioelectrochemistry 138 (2021) 107733.
[119] Z. Ying, L. Feng, D. Ji, Y. Zhang, W. Chen, Y. Dai, M. Janyasupab, X. Li, W. Wen, C.C. Liu, Phase-regulated sensing mechanism of MoS2 based nanohybrids toward point-of-care prostate cancer diagnosis, Small 16 (18) (2020), e2000307.
[120] S. Su, Q. Sun, J. Ma, D. Zhu, F. Wang, J. Chao, C. Fan, Q. Li, L. Wang, Ultrasensitive analysis of microRNAs with gold nanoparticle-decorated molybdenum disulfide nanohybrid-based multilayer nanoprobes, Chem. Commun. 56 (63) (2020) 9012–9015.
[121] S. Schlücker, Surface-enhanced Raman spectroscopy: concepts and chemical applications, Angew. Chem. 53 (19) (2014) 4756–4795.
[122] D. Radziuk, H. Moehwald, Prospects for plasmonic hot spots in single molecule SERS towards the chemical imaging of live cells, Phys. Chem. Chem. Phys. : Phys. Chem. Chem. Phys. 17 (33) (2015) 21072–21093.
[123] L. Liu, C. Shangguan, J. Guo, K. Ma, S. Jiao, Y. Yao, J. Wang, Ultrasensitive SERS detection of cancer-related miRNA-182 by MXene/MoS 2 @AuNPs with controllable morphology and optimized self-internal standards, Advanced Optical Materials 8 (23) (2020) 2001214.
[124] H. Sun, Y. Gao, N. Hu, Y. Zhang, C. Guo, G. Gao, Z. Ma, K. Ivan Ivanovich, Y. Qiu, Electronic coupling between molybdenum disulfide and gold nanoparticles to enhance the peroxidase activity for the colorimetric immunoassays of hydrogen peroxide and cancer cells, J. Colloid Interface Sci. 578 (2020) 366–378.
[125] S. Zhang, Y. Chen, Y. Huang, H. Dai, Y. Lin, Design and application of proximity hybridization-based multiple stimuli-responsive immunosensing platform for ovarian cancer biomarker detection, Biosens. Bioelectron. 159 (2020) 112201.
[126] S. Mohandoss, R. Atchudan, T.N.J.I. Edison, K. Mishra, R.J.I. Tamargo, S. Palanisamy, K. Yelithao, S. You, Y.R. Lee, Rapid response and highly selective sensing of adenosine based on novel photoluminescent vanadium nanoclusters anchored on MoS2 nanosheets, Sensor. Actuator. B Chem. 306 (2020) 127581.
[127] D. Bahari, B. Babamiri, A. Salimi, R. Hallaj, S.M. Amininasab, A self-enhanced ECL-RET immunosensor for the detection of CA19-9 antigen based on Ru(bpy)2 (phen-NH2)(2+) - amine-rich nitrogen-doped carbon nanodots as probe and graphene oxide grafted hyperbranched aromatic polyamide as platform, Anal. Chim. Acta 1132 (2020) 55–65.
[128] Q. Chen, C. Liang, X. Wang, J. He, Y. Li, Z. Liu, An albumin-based theranostic nano-agent for dual-modal imaging guided photothermal therapy to inhibit lymphatic metastasis of cancer post surgery, Biomaterials 35 (34) (2014) 9355–9362.
[129] X. Mu, Y. Lu, Supramolecular nanodiscs self-assembled from non-ionic heptamethine cyanine for imaging-guided cancer photothermal Therapy, 32, 2020, e1906711, 2.
[130] F. Zhou, T. Fu, Q. Huang, H. Kuai, L. Mo, H. Liu, Hypoxia-activated PEGylated conditional aptamer/antibody for cancer imaging with improved Specificity, 141, 2019, pp. 18421–18427, 46.
[131] K. Pant, C. Neuber, K. Zarschler, Active targeting of dendritic polyglycerols for diagnostic cancer imaging, 16, 2020, e1905013, 7.
[132] R.D. Chitalia, J. Rowland, E.S. McDonald, L. Pantalone, E.A. Cohen, Imaging phenotypes of breast cancer heterogeneity in preoperative breast dynamic contrast enhanced magnetic resonance imaging (DCE-MRI) scans predict 10-year recurrence, 26, 2020, pp. 862–869, 4.
[133] X. Zhang, W. Liu, H. Wang, X. Zhao, Z. Zhang, G.U. Nienhaus, L. Shang, Z. Su, Self-assembled thermosensitive luminescent nanoparticles with peptide-Au conjugates for cellular imaging and drug delivery, Chin. Chem. Lett. 31 (3) (2020) 859–864.
[134] J.Y. Zeng, X.S. Wang, B.R. Xie, M.J. Li, X.Z. Zhang, Covalent organic framework for improving near-infrared light induced fluorescence imaging through two-photon Induction, 59, 2020, pp. 10087–10094, 25.
[135] J.B. Li, H.W. Liu, T. Fu, R. Wang, X.B. Zhang, W. Tan, Recent progress in small-molecule near-IR probes for bioimaging, Trends in chemistry 1 (2) (2019) 224–234.
[136] A.N. Bashkatov, E.A. Genina, V.I. Kochubey, V.V. Tuchin, Optical properties of human skin, subcutaneous and mucous tissues in the wavelength range from 400 to 2000 nm, J. Phys. Appl. Phys. 38 (15) (2005) 2543–2555.
[137] X. Michalet, F.F. Pinaud, L.A. Bentolila, J.M. Tsay, S. Doose, J.J. Li, G. Sundaresan, A.M. Wu, S.S. Gambhir, S. Weiss, Quantum dots for live cells, in vivo imaging, and diagnostics, Science (New York, N.Y.). 307 (5709) (2005) 538–544.
[138] E.B. Voura, J.K. Jaiswal, H. Mattoussi, S.M. Simon, Tracking metastatic tumor cell extravasation with quantum dot nanocrystals and fluorescence emission-scanning microscopy, Nat. Med. 10 (9) (2004) 993–998.
[139] Y. Zhang, W. Xiu, Y. Sun, D. Zhu, Q. Zhang, L. Yuwen, L. Weng, Z. Teng, L. Wang, RGD-QD-MoS2 nanosheets for targeted fluorescent imaging and photothermal therapy of cancer, Nanoscale 9 (41) (2017) 15835–15845.
[140] W. Dai, H. Dong, B. Fugetsu, Y. Cao, H. Lu, X. Ma, X. Zhang, Tunable fabrication of molybdenum disulfide quantum dots for intracellular MicroRNA detection and multiphoton bioimaging, Small 11 (33) (2015) 4158–4164.
[141] C. Sweet, A. Pramanik, S. Jones, P.C. Ray, Two-photon fluorescent molybdenum disulfide dots for targeted prostate cancer imaging in the biological II window, ACS Omega 2 (5) (2017) 1826–1835.
[142] J.-Y. Wu, X.-Y. Zhang, X.-D. Ma, Y.-P. Qiu, T. Zhang, High quantum-yield luminescent MoS2 quantum dots with variable light emission created via direct ultrasonic exfoliation of MoS2 nanosheets, RSC Adv. 5 (115) (2015) 95178–95182.
[143] Q. Liu, C. Hu, X. Wang, A facile one-step method to produce MoS2quantum dots as promising bio-imaging materials, RSC Adv. 6 (30) (2016) 25605–25610.
[144] H.J. Kim, J.H. Han, M.K. Kim, C.S. Lim, H.M. Kim, B.R. Cho, Dual-color imaging of sodium/calcium ion activities with two-photon fluorescent probes, Angew. Chem. 49 (38) (2010) 6786–6789.
[145] H.M. Kim, B.R. Kim, J.H. Hong, J.S. Park, K.J. Lee, B.R. Cho, A two-photon fluorescent probe for calcium waves in living tissue, Angew. Chem. 46 (39) (2007) 7445–7448.
[146] E. Cassette, R.D. Pensack, B. Mahler, G.D. Scholes, Room-temperature exciton coherence and dephasing in two-dimensional nanostructures, Nat. Commun. 6 (2015) 6086.
[147] P.D. Howes, R. Chandrawati, M.M. Stevens, Bionanotechnology. Colloidal nanoparticles as advanced biological sensors, Science (New York, N.Y.). 346 (6205) (2014) 1247390.
[148] W. Wu, L. Wang, Y. Li, F. Zhang, L. Lin, S. Niu, D. Chenet, X. Zhang, Y. Hao, T. F. Heinz, J. Hone, Z.L. Wang, Piezoelectricity of single-atomic-layer MoS2 for energy conversion and piezotronics, Nature 514 (7523) (2014) 470–474.
[149] C. Tan, H. Zhang, Two-dimensional transition metal dichalcogenide nanosheet-based composites, Chem. Soc. Rev. 44 (9) (2015) 2713–2731.
[150] H. Dong, S. Tang, Y. Hao, H. Yu, W. Dai, G. Zhao, Y. Cao, H. Lu, X. Zhang, H. Ju, Fluorescent MoS2 quantum dots: ultrasonic preparation, up-conversion and down-conversion bioimaging, and photodynamic therapy, ACS Appl. Mater. Interfaces 8 (5) (2016) 3107–3114.
[151] M. Amani, D.H. Lien, D. Kiriya, J. Xiao, A. Azcatl, J. Noh, S.R. Madhvapathy, R. Addou, S. Kc, M. Dubey, K. Cho, R.M. Wallace, S.C. Lee, J.H. He, J.W. Ager 3rd, X. Zhang, E. Yablonovitch, A. Javey, Near-unity photoluminescence quantum yield in MoS_2, Science (New York, N.Y.) 350 (6264) (2015) 1065–1068.
[152] K. Zhou, Y. Zhang, Z. Xia, W. Wei, As-prepared MoS2 quantum dot as a facile fluorescent probe for long-term tracing of live cells, Nanotechnology 27 (27) (2016) 275101.
[153] S. Zheng, M. Zhang, H. Bai, M. He, L. Dong, L. Cai, M. Zhao, Q. Wang, K. Xu, J. Li, Preparation of AS1411 aptamer modified Mn-MoS(2) QDs for targeted MR imaging and fluorescence labelling of renal cell carcinoma, Int. J. Nanomed. 14 (2019) 9513–9524.
[154] W. Gu, Y. Yan, X. Cao, C. Zhang, C. Ding, Y. Xian, A facile and one-step ethanol-thermal synthesis of MoS(2) quantum dots for two-photon fluorescence imaging, J. Mater. Chem. B. 4 (1) (2016) 27–31.
[155] A. Sharma, T. Gadly, A. Gupta, A. Ballal, S.K. Ghosh, M. Kumbhakar, Origin of excitation dependent fluorescence in carbon nanodots, J. Phys. Chem. Lett. 7 (18) (2016) 3695–3702.
[156] S.S. Sinha, D.K. Paul, R. Kanchanapally, A. Pramanik, S.R. Chavva, B.P. Viraka Nellore, S.J. Jones, P.C. Ray, Long-range two-photon scattering spectroscopy ruler for screening prostate cancer cells, Chem. Sci. 6 (4) (2015) 2411–2418.
[157] A. Pramanik, S.R. Chavva, Z. Fan, S.S. Sinha, B.P. Nellore, P.C. Ray, Extremely high two-photon absorbing graphene oxide for imaging of tumor cells in the second biological window, J. Phys. Chem. Lett. 5 (12) (2014) 2150–2154.
[158] A.B. Chinen, C.M. Guan, J.R. Ferrer, S.N. Barnaby, T.J. Merkel, C.A. Mirkin, Nanoparticle probes for the detection of cancer biomarkers, cells, and tissues by fluorescence, Chem. Rev. 115 (19) (2015) 10530–10574.
[159] S. Khan, A. Gupta, N.C. Verma, C.K. Nandi, Time-resolved emission reveals ensemble of emissive states as the origin of multicolor fluorescence in carbon dots, Nano Lett. 15 (12) (2015) 8300–8305.
[160] H. Dai, Q. Shen, J. Shao, W. Wang, F. Gao, X. Dong, Small molecular NIR-II fluorophores for cancer phototheranostics, Innovation (2021) 100082.
[161] C. Kim, C. Favazza, L.V. Wang, In vivo photoacoustic tomography of chemicals: high-resolution functional and molecular optical imaging at new depths, Chem. Rev. 110 (5) (2010) 2756–2782.
[162] V. Ntziachristos, D. Razansky, Molecular imaging by means of multispectral optoacoustic tomography (MSOT), Chem. Rev. 110 (5) (2010) 2783–2794.
[163] G. Liu, J. Zhu, H. Guo, A. Sun, P. Chen, L. Xi, W. Huang, X. Song, X. Dong, Mo(2) C-Derived polyoxometalate for NIR-II photoacoustic imaging-guided chemodynamic/photothermal synergistic Therapy, 58, 2019, pp. 18641–18646, 51.
[164] S.P. Johnson, O. Ogunlade, M.F. Lythgoe, P. Beard, R.B. Pedley, Longitudinal photoacoustic imaging of the pharmacodynamic effect of vascular targeted therapy on tumors, Clin. Canc. Res. : an official journal of the American Association for Cancer Research 25 (24) (2019) 7436–7447.
[165] J. Jo, In vivo photoacoustic lifetime based oxygen imaging with tumor targeted G2 polyacrylamide, Nanosonophores 13 (12) (2019) 14024–14032.
[166] J. Yu, W. Yin, X. Zheng, G. Tian, X. Zhang, T. Bao, X. Dong, Z. Wang, Z. Gu, X. Ma, Y. Zhao, Smart MoS2/Fe3O4 nanotheranostic for magnetically targeted photothermal therapy guided by magnetic resonance/photoacoustic imaging, Theranostics 5 (9) (2015) 931–945.
[167] H. Jiang, Y. Du, L. Chen, M. Qian, Y. Yang, T. Huo, X. Yan, T. Ye, B. Han, Y. Wang, R. Huang, Multimodal theranostics augmented by transmembrane polymer-sealed nano-enzymatic porous MoS(2) nanoflowers, Int. J. Pharm. 586 (2020) 119606.
[168] G. Ku, M. Zhou, S. Song, Q. Huang, J. Hazle, C. Li, Copper sulfide nanoparticles as a new class of photoacoustic contrast agent for deep tissue imaging at 1064 nm, ACS Nano 6 (8) (2012) 7489–7496.

[169] W. Lu, Q. Huang, G. Ku, X. Wen, M. Zhou, D. Guzatov, P. Brecht, R. Su, A. Oraevsky, L.V. Wang, C. Li, Photoacoustic imaging of living mouse brain vasculature using hollow gold nanospheres, Biomaterials 31 (9) (2010) 2617–2626.
[170] J. Chen, C. Liu, D. Hu, F. Wang, H. Wu, X. Gong, X. Liu, L. Song, Z. Sheng, H. Zheng, Single-layer MoS2Nanosheets with amplified photoacoustic effect for highly sensitive photoacoustic imaging of orthotopic brain tumors, Adv. Funct. Mater. 26 (47) (2016) 8715–8725.
[171] J. Shi, H. Zhang, Z. Chen, L. Xu, Z. Zhang, A multi-functional nanoplatform for efficacy tumor theranostic applications, Asian J. Pharm. Sci. 12 (3) (2017) 235–249.
[172] J. Liu, X. Zheng, L. Yan, L. Zhou, G. Tian, W. Yin, L. Wang, Y. Liu, Z. Hu, Z. Gu, C. Chen, Y. Zhao, Bismuth sulfide nanorods as a precision nanomedicine for in vivo multimodal imaging-guided photothermal therapy of tumor, ACS Nano 9 (1) (2015) 696–707.
[173] H. Li, X. Qi, J. Wu, Z. Zeng, J. Wei, H. Zhang, Investigation of MoS_2 and graphene nanosheets by magnetic force microscopy, ACS Nano 7 (3) (2013) 2842–2849.
[174] N. Liu, P. Kim, J.H. Kim, J.H. Ye, S. Kim, C.J. Lee, Large-area atomically thin MoS2 nanosheets prepared using electrochemical exfoliation, ACS Nano 8 (7) (2014) 6902–6910.
[175] L. Liu, J. Wang, X. Tan, X. Pang, Q. You, Q. Sun, F. Tan, N. Li, Photosensitizer loaded PEG-MoS(2)-Au hybrids for CT/NIRF imaging-guided stepwise photothermal and photodynamic therapy, J. Mater. Chem. B. 5 (12) (2017) 2286–2296.
[176] B. Geng, H. Qin, F. Zheng, W. Shen, P. Li, K. Wu, X. Wang, X. Li, D. Pan, L. Shen, Carbon dot-sensitized MoS(2) nanosheet heterojunctions as highly efficient NIR photothermal agents for complete tumor ablation at an ultralow laser exposure, Nanoscale 11 (15) (2019) 7209–7220.
[177] T. Liu, S. Shi, C. Liang, S. Shen, L. Cheng, C. Wang, X. Song, S. Goel, T.E. Barnhart, W. Cai, Z. Liu, Iron oxide decorated MoS2 nanosheets with double PEGylation for chelator-free radiolabeling and multimodal imaging guided photothermal therapy, ACS Nano 9 (1) (2015) 950–960.
[178] Y. Yu, B. Chi, L. Lin, Z. Yang, Q. He, Z. Xu, C. Yi, J. Wang, Microwave-assisted preparation of paramagnetic zwitterionic amphiphilic copolymer hybrid molybdenum disulfide for T1-weighted magnetic resonance imaging-guided photothermal therapy, J. Mater. Chem. B. 6 (40) (2018) 6391–6398.
[179] J.M. Hooker, R.E. Carson, Human positron emission tomography neuroimaging, Annu. Rev. Biomed. Eng. 21 (2019) 551–581.
[180] D. Ni, E.B. Ehlerding, W. Cai, Multimodality imaging agents with PET as the fundamental pillar, 58, 2019, pp. 2570–2579, 9.
[181] X. Dong, W. Yin, Intelligent MoS(2) nanotheranostic for targeted and enzyme-/pH-/NIR-responsive drug delivery to overcome cancer chemotherapy resistance guided by PET Imaging, 10, 2018, pp. 4271–4284, 4.
[182] M. Iima, D. Le Bihan, Clinical intravoxel incoherent motion and diffusion MR imaging: past, present, and future, Radiology 278 (1) (2016) 13–32.
[183] A. Gizzatov, V. Keshishian, A. Guven, A.M. Dimiev, F. Qu, R. Muthupillai, P. Decuzzi, R.G. Bryant, J.M. Tour, L.J. Wilson, Enhanced MRI relaxivity of aquated Gd3+ ions by carboxyphenylated water-dispersed graphene nanoribbons, Nanoscale 6 (6) (2014) 3059–3063.
[184] J. Zhang, G. Hao, C. Yao, J. Yu, J. Wang, W. Yang, C. Hu, B. Zhang, Albumin-mediated biomineralization of paramagnetic NIR Ag2S QDs for tiny tumor bimodal targeted imaging in vivo, ACS Appl. Mater. Interfaces 8 (26) (2016) 16612–16621.
[185] G. Cheng, G. Li, H. Xue, S. Chen, J.D. Bryers, S. Jiang, Zwitterionic carboxybetaine polymer surfaces and their resistance to long-term biofilm formation, Biomaterials 30 (28) (2009) 5234–5240.
[186] H. Vaisocherová, Z. Zhang, W. Yang, Z. Cao, G. Cheng, A.D. Taylor, M. Piliarik, J. Homola, S. Jiang, Functionalizable surface platform with reduced nonspecific protein adsorption from full blood plasma–material selection and protein immobilization optimization, Biosens. Bioelectron. 24 (7) (2009) 1924–1930.
[187] S. Jiang, Z. Cao, Ultralow-fouling, functionalizable, and hydrolyzable zwitterionic materials and their derivatives for biological applications, Adv. Mater. 22 (9) (2010) 920–932.
[188] Y. Cheng, T. Lu, Y. Wang, Y. Song, S. Wang, Q. Lu, L. Yang, F. Tan, J. Li, N. Li, Glutathione-mediated clearable nanoparticles based on ultrasmall Gd(2)O(3) for MSOT/CT/MR imaging guided photothermal/radio combination cancer, Therapy 16 (8) (2019) 3489–3501.
[189] J. Wang, X. Tan, X. Pang, L. Liu, F. Tan, N. Li, MoS2 quantum Dot@Polyaniline inorganic-organic nanohybrids for in vivo dual-modal imaging guided synergistic photothermal/radiation therapy, ACS Appl. Mater. Interfaces 8 (37) (2016) 24331–24338.
[190] P. Li, L. Liu, Q. Lu, S. Yang, L. Yang, Y. Cheng, Y. Wang, S. Wang, Y. Song, F. Tan, N. Li, Ultrasmall MoS(2) nanodots-doped biodegradable SiO(2) nanoparticles for clearable FL/CT/MSOT imaging-guided PTT/PDT combination, Tumor Therapy 11 (6) (2019) 5771–5781.
[191] F. Gao, D. Wang, T. Zhang, A. Ghosal, Z. Guo, Y. Miao, G. Li, X. Liu, J. Lu, J. Yu, H. Fan, L. Zhao, Facile synthesis of Bi2S3-MoS2 heterogeneous nanoagent as dual functional radiosensitizer for triple negative breast cancer theranostics, Chem. Eng. J. 395 (2020) 125032.
[192] S. Tang, C. Fu, L. Tan, T. Liu, J. Mao, X. Ren, H. Su, D. Long, Q. Chai, Z. Huang, X. Chen, J. Wang, J. Ren, X. Meng, Imaging-guided synergetic therapy of orthotopic transplantation tumor by superselectively arterial administration of microwave-induced microcapsules, Biomaterials 133 (2017) 144–153.
[193] L. Yang, J. Wang, S. Yang, Q. Lu, P. Li, N. Li, Rod-shape MSN@MoS(2) nanoplatform for FL/MSOT/CT imaging-guided photothermal and photodynamic therapy, Theranostics 9 (14) (2019) 3992–4005.
[194] L. Liu, J. Wang, Q. You, Q. Sun, Y. Song, Y. Wang, Y. Cheng, S. Wang, F. Tan, N. Li, NIRF/PA/CT multi-modality imaging guided combined photothermal and photodynamic therapy based on tumor microenvironment-responsive nanocomposites, J. Mater. Chem. B. 6 (25) (2018) 4239–4250.
[195] T.M. Allen, P.R. Cullis, Liposomal drug delivery systems: from concept to clinical applications, Adv. Drug Deliv. Rev. 65 (1) (2013) 36–48.
[196] S. Mignani, S. El Kazzouli, M. Bousmina, J.P. Majoral, Expand classical drug administration ways by emerging routes using dendrimer drug delivery systems: a concise overview, Adv. Drug Deliv. Rev. 65 (10) (2013) 1316–1330.
[197] W. Zhang, Y. Wang, X. Sun, W. Wang, L. Chen, Mesoporous titania based yolk-shell nanoparticles as multifunctional theranostic platforms for SERS imaging and chemo-photothermal treatment, Nanoscale 6 (23) (2014) 14514–14522.
[198] A. Nouri, B. Faraji Dizaji, N. Kianinejad, A. Jafari Rad, S. Rahimi, M. Irani, F. Sharifian Jazi, Simultaneous linear release of folic acid and doxorubicin from ethyl cellulose/chitosan/g-C3 N4/MoS2 core-shell nanofibers and its anticancer properties, J. Biomed. Mater. Res. 109 (9) (2020) 903–914.
[199] E. Fleige, M.A. Quadir, R. Haag, Stimuli-responsive polymeric nanocarriers for the controlled transport of active compounds: concepts and applications, Adv. Drug Deliv. Rev. 64 (9) (2012) 866–884.
[200] S. Ganta, H. Devalapally, A. Shahiwala, M. Amiji, A review of stimuli-responsive nanocarriers for drug and gene delivery, J. Contr. Release : official journal of the Controlled Release Society 126 (3) (2008) 187–204.
[201] W. Long, H. Ouyang, C. Zhou, W. Wan, S. Yu, K. Qian, M. Liu, X. Zhang, Y. Feng, Y. Wei, A novel one-pot strategy for fabrication of PEGylated MoS2 composites for pH responsive controlled drug delivery, J. Mol. Liq. 307 (2020) 112962.
[202] M. Meinhardt, R. Krebs, A. Anders, U. Heinrich, H. Tronnier, Wavelength-dependent penetration depths of ultraviolet radiation in human skin, J. Biomed. Opt. 13 (4) (2008), 044030.
[203] X. Huang, I.H. El-Sayed, W. Qian, M.A. El-Sayed, Cancer cell imaging and photothermal therapy in the near-infrared region by using gold nanorods, J. Am. Chem. Soc. 128 (6) (2006) 2115–2120.
[204] S.S. Chou, M. De, J. Kim, S. Byun, C. Dykstra, J. Yu, J. Huang, V.P. Dravid, Ligand conjugation of chemically exfoliated MoS2, J. Am. Chem. Soc. 135 (12) (2013) 4584–4587.
[205] J. Lee, H. Park, W.J. Kim, Nano "Chocolate Waffle" for near-IR responsive drug releasing system, Small 11 (39) (2015) 5315–5323.
[206] J. Lee, J. Kim, W.J. Kim, Photothermally controllable cytosolic drug delivery based on core–shell MoS2-porous silica nanoplates, Chem. Mater. 28 (17) (2016) 6417–6424.
[207] W. Zhao, A. Li, C. Chen, F. Quan, L. Sun, A. Zhang, Y. Zheng, J. Liu, Transferrin-decorated, MoS2-capped hollow mesoporous silica nanospheres as a self-guided chemo-photothermal nanoplatform for controlled drug release and thermotherapy, J. Mater. Chem. B. 5 (35) (2017) 7403–7414.
[208] J. Ma, R. Liu, X. Wang, Q. Liu, Y. Chen, R.P. Valle, Y.Y. Zuo, T. Xia, S. Liu, Crucial role of lateral size for graphene oxide in activating macrophages and stimulating pro-inflammatory responses in cells and animals, ACS Nano 9 (10) (2015) 10498–10515.
[209] M. Xu, J. Zhu, F. Wang, Y. Xiong, Y. Wu, Q. Wang, J. Weng, Z. Zhang, W. Chen, S. Liu, Improved in vitro and in vivo biocompatibility of graphene oxide through surface modification: poly(acrylic acid)-functionalization is superior to PEGylation, ACS Nano 10 (3) (2016) 3267–3281.
[210] S. Chen, C. Xiong, H. Liu, Q. Wan, J. Hou, Q. He, A. Badu-Tawiah, Z. Nie, Mass spectrometry imaging reveals the sub-organ distribution of carbon nanomaterials, Nat. Nanotechnol. 10 (2) (2015) 176–182.
[211] M. Nurunnabi, Z. Khatun, K.M. Huh, S.Y. Park, D.Y. Lee, K.J. Cho, Y.K. Lee, In vivo biodistribution and toxicology of carboxylated graphene quantum dots, ACS Nano 7 (8) (2013) 6858–6867.
[212] K. Yang, L. Feng, X. Shi, Z. Liu, Nano-graphene in biomedicine: theranostic applications, Chem. Soc. Rev. 42 (2) (2013) 530–547.
[213] Y. Liu, J. Peng, S. Wang, M. Xu, M. Gao, T. Xia, J. Weng, A. Xu, S. Liu, Molybdenum disulfide/graphene oxide nanocomposites show favorable lung targeting and enhanced drug loading/tumor-killing efficacy with improved biocompatibility, NPG Asia Mater. 10 (1) (2018) e458-e458.
[214] C. Holohan, S. Van Schaeybroeck, D.B. Longley, P.G. Johnston, Cancer drug resistance: an evolving paradigm, Nat. Rev. Canc. 13 (10) (2013) 714–726.
[215] D. Jiao, S. Yang, Overcoming resistance to drugs targeting KRAS(G12C) mutation, innovation (New York, N.Y.), 1, 2020, 2.
[216] F. Thiebaut, T. Tsuruo, H. Hamada, M.M. Gottesman, I. Pastan, M.C. Willingham, Cellular localization of the multidrug-resistance gene product P-glycoprotein in normal human tissues, Proc. Natl. Acad. Sci. U. S. A 84 (21) (1987) 7735–7738.
[217] Y. Zhong, J. Zhang, R. Cheng, C. Deng, F. Meng, F. Xie, Z. Zhong, Reversibly crosslinked hyaluronic acid nanoparticles for active targeting and intelligent delivery of doxorubicin to drug resistant CD44+ human breast tumor xenografts, J. Contr. Release : official journal of the Controlled Release Society 205 (2015) 144–154.
[218] J. Wang, J. Liu, Y. Liu, L. Wang, M. Cao, Y. Ji, X. Wu, Y. Xu, B. Bai, Q. Miao, C. Chen, Y. Zhao, Gd-hybridized plasmonic Au-nanocomposites enhanced tumor-interior drug permeability in multimodal imaging-guided therapy, Adv. Mater. 28 (40) (2016) 8950–8958.
[219] X. Dong, W. Yin, X. Zhang, S. Zhu, X. He, J. Yu, J. Xie, Z. Guo, L. Yan, X. Liu, Q. Wang, Z. Gu, Y. Zhao, Intelligent MoS2 nanotheranostic for targeted and enzyme-/pH-/NIR-responsive drug delivery to overcome cancer chemotherapy resistance guided by PET imaging, ACS Appl. Mater. Interfaces 10 (4) (2018) 4271–4284.
[220] B. Sumer, J. Gao, Theranostic nanomedicine for cancer, Nanomedicine 3 (2) (2008) 137–140.

[221] A. Jemal, F. Bray, M.M. Center, J. Ferlay, E. Ward, D. Forman, Global cancer statistics, CA A Cancer J. Clin. 61 (2) (2011) 69–90.
[222] A. Jemal, R. Siegel, J. Xu, E. Ward, Cancer statistics, 2010, CA A Cancer J. Clin. 60 (5) (2010) 277–300.
[223] R. Siegel, D. Naishadham, A. Jemal, Cancer statistics, 2012, CA A Cancer J. Clin. 62 (1) (2012) 10–29.
[224] R. Siegel, D. Naishadham, A. Jemal, Cancer statistics, 2013, CA A Cancer J. Clin. 63 (1) (2013) 11–30.
[225] M. Feng, Y. Pan, R. Kong, S. Shu, Therapy of primary liver cancer, Innovation 1 (2) (2020) 100032.
[226] J.P. Celli, B.Q. Spring, I. Rizvi, C.L. Evans, K.S. Samkoe, S. Verma, B.W. Pogue, T. Hasan, Imaging and photodynamic therapy: mechanisms, monitoring, and optimization, Chem. Rev. 110 (5) (2010) 2795–2838.
[227] M.P. Melancon, M. Zhou, C. Li, Cancer theranostics with near-infrared light-activatable multimodal nanoparticles, Accounts Chem. Res. 44 (10) (2011) 947–956.
[228] H.I. Karunadasa, E. Montalvo, Y. Sun, M. Majda, J.R. Long, C.J. Chang, A molecular MoS_2 edge site mimic for catalytic hydrogen generation, Science (New York, N.Y.). 335 (6069) (2012) 698–702.
[229] Z. Chen, Q. Wang, H. Wang, L. Zhang, G. Song, L. Song, J. Hu, H. Wang, J. Liu, M. Zhu, D. Zhao, Ultrathin PEGylated W18O49 nanowires as a new 980 nm-laser-driven photothermal agent for efficient ablation of cancer cells in vivo, Adv. Mater. 25 (14) (2013) 2095–2100.
[230] K. Yang, G. Yang, L. Chen, L. Cheng, L. Wang, C. Ge, Z. Liu, FeS nanoplates as a multifunctional nano-theranostic for magnetic resonance imaging guided photothermal therapy, Biomaterials 38 (2015) 1–9.
[231] K. Yang, H. Xu, L. Cheng, C. Sun, J. Wang, Z. Liu, In vitro and in vivo near-infrared photothermal therapy of cancer using polypyrrole organic nanoparticles, Adv. Mater. 24 (41) (2012) 5586–5592.
[232] C. He, X. Duan, N. Guo, C. Chan, C. Poon, R.R. Weichselbaum, W. Lin, Core-shell nanoscale coordination polymers combine chemotherapy and photodynamic therapy to potentiate checkpoint blockade cancer immunotherapy, Nat. Commun. 7 (2016) 12499.
[233] L. Cheng, C. Wang, L. Feng, K. Yang, Z. Liu, Functional nanomaterials for phototherapies of cancer, Chem. Rev. 114 (21) (2014) 10869–10939.
[234] L. Zou, H. Wang, B. He, L. Zeng, T. Tan, H. Cao, X. He, Z. Zhang, S. Guo, Y. Li, Current approaches of photothermal therapy in treating cancer metastasis with nanotherapeutics, Theranostics 6 (6) (2016) 762–772.
[235] Z. Zha, X. Yue, Q. Ren, Z. Dai, Uniform polypyrrole nanoparticles with high photothermal conversion efficiency for photothermal ablation of cancer cells, Adv. Mater. 25 (5) (2013) 777–782.
[236] Z.M. Markovic, L.M. Harhaji-Trajkovic, B.M. Todorovic-Markovic, D.P. Kepić, K. M. Arsikin, S.P. Jovanović, A.C. Pantovic, M.D. Dramićanin, V.S. Trajkovic, In vitro comparison of the photothermal anticancer activity of graphene nanoparticles and carbon nanotubes, Biomaterials 32 (4) (2011) 1121–1129.
[237] W. Yin, L. Yan, J. Yu, G. Tian, L. Zhou, X. Zheng, X. Zhang, Y. Yong, J. Li, Z. Gu, Y. Zhao, High-throughput synthesis of single-layer MoS2 nanosheets as a near-infrared photothermal-triggered drug delivery for effective cancer therapy, ACS Nano 8 (7) (2014) 6922–6933.
[238] L. Ding, Y. Chang, P. Yang, W. Gao, M. Sun, Y. Bie, L. Yang, X. Ma, Y. Guo, Facile synthesis of biocompatible L-cysteine-modified MoS2 nanospheres with high photothermal conversion efficiency for photothermal therapy of tumor, Materials science & engineering. C, Materials for biological applications 117 (2020) 111371.
[239] S. Rajasekar, E.M. Martin, S. Kuppusamy, C. Vetrivel, Chitosan coated molybdenum sulphide nanosheet incorporated with tantalum oxide nanomaterials for improving cancer photothermal therapy, Arabian Journal of Chemistry 13 (3) (2020) 4741–4750.
[240] S. Wang, K. Li, Y. Chen, H. Chen, M. Ma, J. Feng, Q. Zhao, J. Shi, Biocompatible PEGylated MoS2 nanosheets: controllable bottom-up synthesis and highly efficient photothermal regression of tumor, Biomaterials 39 (2015) 206–217.
[241] C. Fu, L. Tan, X. Ren, Q. Wu, H. Shao, J. Ren, Y. Zhao, X. Meng, Interlayer expansion of 2D MoS(2) nanosheets for highly improved photothermal therapy of tumors in vitro and in vivo, Chem. Commun. 54 (99) (2018) 13989–13992.
[242] L. Tan, S. Wang, K. Xu, T. Liu, P. Liang, M. Niu, C. Fu, H. Shao, J. Yu, T. Ma, X. Ren, H. Li, J. Dou, J. Ren, X. Meng, Layered MoS2 hollow spheres for highly-efficient photothermal therapy of rabbit liver orthotopic transplantation tumors, Small 12 (15) (2016) 2046–2055.
[243] W. Zhao, M. Lang, Y. Li, L. Li, J. Shi, Fabrication of uniform hollow mesoporous silica spheres and ellipsoids of tunable size through a facile hard-templating route, J. Mater. Chem. 19 (18) (2009) 2778.
[244] W. Feng, L. Chen, M. Qin, X. Zhou, Q. Zhang, Y. Miao, K. Qiu, Y. Zhang, C. He, Flower-like PEGylated MoS2 nanoflakes for near-infrared photothermal cancer therapy, Sci. Rep. 5 (2015) 17422.
[245] M. Hong, S. Zhu, Y. Jiang, G. Tang, Y. Pei, Efficient tumor targeting of hydroxycamptothecin loaded PEGylated niosomes modified with transferrin, J. Contr. Release : official journal of the Controlled Release Society 133 (2) (2009) 96–102.
[246] K.J. Harrington, S. Mohammadtaghi, P.S. Uster, D. Glass, A.M. Peters, R.G. Vile, J. S. Stewart, Effective targeting of solid tumors in patients with locally advanced cancers by radiolabeled pegylated liposomes, Clin. Canc. Res. : an official journal of the American Association for Cancer Research 7 (2) (2001) 243–254.
[247] Y.X. Wang, X.M. Zhu, Q. Liang, C.H. Cheng, W. Wang, K.C. Leung, In vivo chemoembolization and magnetic resonance imaging of liver tumors by using iron oxide nanoshell/doxorubicin/poly(vinyl alcohol) hybrid composites, Angew. Chem. 53 (19) (2014) 4812–4815.
[248] A. Nel, T. Xia, L. Mädler, N. Li, Toxic potential of materials at the nanolevel, Science (New York, N.Y.). 311 (5761) (2006) 622–627.
[249] X. Song, Q. Chen, Z. Liu, Recent advances in the development of organic photothermal nano-agents, Nano Research 8 (2) (2014) 340–354.
[250] J. Liu, M. Yu, C. Zhou, S. Yang, X. Ning, J. Zheng, Passive tumor targeting of renal-clearable luminescent gold nanoparticles: long tumor retention and fast normal tissue clearance, J. Am. Chem. Soc. 135 (13) (2013) 4978–4981.
[251] M. Longmire, P.L. Choyke, H. Kobayashi, Clearance properties of nano-sized particles and molecules as imaging agents: considerations and caveats, Nanomedicine 3 (5) (2008) 703–717.
[252] T. Liu, Y. Chao, M. Gao, C. Liang, Q. Chen, G. Song, L. Cheng, Z. Liu, Ultra-small MoS2 nanodots with rapid body clearance for photothermal cancer therapy, Nano Research 9 (10) (2016) 3003–3017.
[253] M. Zhou, J. Li, S. Liang, A.K. Sood, D. Liang, C. Li, CuS nanodots with ultrahigh efficient renal clearance for positron emission tomography imaging and image-guided photothermal therapy, ACS Nano 9 (7) (2015) 7085–7096.
[254] C. Zhang, W. Bu, D. Ni, C. Zuo, C. Cheng, Q. Li, L. Zhang, Z. Wang, J. Shi, A polyoxometalate cluster paradigm with self-adaptive electronic structure for acidity/reducibility-specific photothermal conversion, J. Am. Chem. Soc. 138 (26) (2016) 8156–8164.
[255] G. Song, J. Hao, C. Liang, T. Liu, M. Gao, L. Cheng, J. Hu, Z. Liu, Degradable molybdenum oxide nanosheets with rapid clearance and efficient tumor homing capabilities as a therapeutic nanoplatform, Angew. Chem. 55 (6) (2016) 2122–2126.
[256] J.G. Croissant, Y. Fatieiev, N.M. Khashab, Degradability and clearance of silicon, organosilica, silsesquioxane, silica mixed oxide, and mesoporous silica nanoparticles, Adv. Mater. 29 (9) (2017).
[257] S. Maher, T. Kumeria, Y. Wang, G. Kaur, D. Fathalla, G. Fetih, A. Santos, F. Habib, A. Evdokiou, D. Losic, From the mine to cancer therapy: natural and biodegradable theranostic silicon nanocarriers from diatoms for sustained delivery of chemotherapeutics, Advanced healthcare materials 5 (20) (2016) 2667–2678.
[258] L. Chen, Y. Feng, X. Zhou, Q. Zhang, W. Nie, W. Wang, Y. Zhang, C. He, One-pot synthesis of MoS2 nanoflakes with desirable degradability for photothermal cancer therapy, ACS Appl. Mater. Interfaces 9 (20) (2017) 17347–17358.
[259] D.E. Dolmans, D. Fukumura, R.K. Jain, Photodynamic therapy for cancer, Nat. Rev. Canc. 3 (5) (2003) 380–387.
[260] H. Kamata, S. Honda, S. Maeda, L. Chang, H. Hirata, M. Karin, Reactive oxygen species promote TNFalpha-induced death and sustained JNK activation by inhibiting MAP kinase phosphatases, Cell 120 (5) (2005) 649–661.
[261] H.U. Simon, A. Haj-Yehia, F. Levi-Schaffer, Role of reactive oxygen species (ROS) in apoptosis induction, Apoptosis : an international journal on programmed cell death 5 (5) (2000) 415–418.
[262] S. Kapri, S. Bhattacharyya, Molybdenum sulfide-reduced graphene oxide p-n heterojunction nanosheets with anchored oxygen generating manganese dioxide nanoparticles for enhanced photodynamic therapy, Chem. Sci. 9 (48) (2018) 8982–8989.
[263] J. van der Zee, Heating the patient: a promising approach? Ann. Oncol. : official journal of the European Society for Medical Oncology 13 (8) (2002) 1173–1184.
[264] S. Wang, P. Huang, L. Nie, R. Xing, D. Liu, Z. Wang, J. Lin, S. Chen, G. Niu, G. Lu, X. Chen, Single continuous wave laser induced photodynamic/plasmonic photothermal therapy using photosensitizer-functionalized gold nanostars, Adv. Mater. 25 (22) (2013) 3055–3061.
[265] W.H. Chen, G.F. Luo, Q. Lei, S. Hong, W.X. Qiu, L.H. Liu, S.X. Cheng, X.Z. Zhang, Overcoming the heat endurance of tumor cells by interfering with the anaerobic glycolysis metabolism for improved, Photothermal Therapy 11 (2) (2017) 1419–1431.
[266] T.M. Busch, S.M. Hahn, S.M. Evans, C.J. Koch, Depletion of tumor oxygenation during photodynamic therapy: detection by the hypoxia marker EF3 [2-(2-nitroimidazol-1[H]-yl)-N-(3,3,3-trifluoropropyl)acetamide], Canc. Res. 60 (10) (2000) 2636–2642.
[267] C. McEwan, J. Owen, E. Stride, C. Fowley, H. Nesbitt, D. Cochrane, C.C. Coussios, M. Borden, N. Nomikou, A.P. McHale, J.F. Callan, Oxygen carrying microbubbles for enhanced sonodynamic therapy of hypoxic tumours, J. Contr. Release : official journal of the Controlled Release Society 203 (2015) 51–56.
[268] C.T. Lee, T. Mace, E.A. Repasky, Hypoxia-driven immunosuppression: a new reason to use thermal therapy in the treatment of cancer? Int. J. Hyperther. : the official journal of European Society for Hyperthermic Oncology, North American Hyperthermia Group 26 (3) (2010) 232–246.
[269] T. Liu, C. Wang, W. Cui, H. Gong, C. Liang, X. Shi, Z. Li, B. Sun, Z. Liu, Combined photothermal and photodynamic therapy delivered by PEGylated MoS2 nanosheets, Nanoscale 6 (19) (2014) 11219–11225.
[270] M.Y. Peng, D.W. Zheng, S.B. Wang, S.X. Cheng, X.Z. Zhang, Multifunctional nanosystem for synergistic tumor therapy delivered by two-dimensional MoS2, ACS Appl. Mater. Interfaces 9 (16) (2017) 13965–13975.
[271] S. Li, S. Yang, C. Liu, J. He, T. Li, C. Fu, X. Meng, H. Shao, Enhanced photothermal-photodynamic therapy by indocyanine green and curcumin-loaded layered MoS2 hollow spheres via inhibition of P-glycoprotein, Int. J. Nanomed. 16 (2021) 433–442.
[272] B. Mahler, V. Hoepfner, K. Liao, G.A. Ozin, Colloidal synthesis of 1T-WS2 and 2H-WS2 nanosheets: applications for photocatalytic hydrogen evolution, J. Am. Chem. Soc. 136 (40) (2014) 14121–14127.
[273] J. Wang, J. Liu, D. Chao, J. Yan, J. Lin, Z.X. Shen, Self-assembly of honeycomb-like MoS2 nanoarchitectures anchored into graphene foam for enhanced lithium-ion storage, Adv. Mater. 26 (42) (2014) 7162–7169.

[274] C. Oliver Kappe, Microwave dielectric heating in synthetic organic chemistry, Chem. Soc. Rev. 37 (6) (2008) 1127–1139.
[275] C.O. Kappe, Controlled microwave heating in modern organic synthesis, Angew. Chem. 43 (46) (2004) 6250–6284.
[276] K. Motokura, M. Tada, Y. Iwasawa, Layered materials with coexisting acidic and basic sites for catalytic one-pot reaction sequences, J. Am. Chem. Soc. 131 (23) (2009) 7944–7945.
[277] J. Sun, H. Liu, X. Chen, D.G. Evans, W. Yang, X. Duan, Carbon nanorings and their enhanced lithium storage properties, Adv. Mater. 25 (8) (2013) 1125–1130, 1124.
[278] W. Chen, Z. Fan, X. Pan, X. Bao, Effect of confinement in carbon nanotubes on the activity of Fischer-Tropsch iron catalyst, J. Am. Chem. Soc. 130 (29) (2008) 9414–9419.
[279] S. Wang, L. Tan, P. Liang, T. Liu, J. Wang, C. Fu, J. Yu, J. Dou, H. Li, X. Meng, Layered MoS2 nanoflowers for microwave thermal therapy, J. Mater. Chem. B 4 (12) (2016) 2133–2141.
[280] C. Fu, F. He, L. Tan, X. Ren, W. Zhang, T. Liu, J. Wang, J. Ren, X. Chen, X. Meng, MoS2 nanosheets encapsulated in sodium alginate microcapsules as microwave embolization agents for large orthotopic transplantation tumor therapy, Nanoscale 9 (39) (2017) 14846–14853.
[281] R.L. Manthe, S.P. Foy, N. Krishnamurthy, B. Sharma, V. Labhasetwar, Tumor ablation and nanotechnology, Mol. Pharm. 7 (6) (2010) 1880–1898.
[282] D.S. Lu, S.S. Raman, D.J. Vodopich, M. Wang, J. Sayre, C. Lassman, Effect of vessel size on creation of hepatic radiofrequency lesions in pigs: assessment of the "heat sink" effect, AJR. American journal of roentgenology. 178 (1) (2002) 47–51.
[283] C. Audigier, T. Mansi, H. Delingette, S. Rapaka, V. Mihalef, D. Carnegie, E. Boctor, M. Choti, A. Kamen, N. Ayache, D. Comaniciu, Efficient lattice Boltzmann solver for patient-specific radiofrequency ablation of hepatic tumors, IEEE Trans. Med. Imag. 34 (7) (2015) 1576–1589.
[284] C. Liu, P. Liang, F. Liu, Y. Wang, X. Li, Z. Han, C. Liu, MWA combined with TACE as a combined therapy for unresectable large-sized hepatocellular carcinoma, Int. J. Hyperther. : the official journal of European Society for Hyperthermic Oncology, North American Hyperthermia Group 27 (7) (2011) 654–662.
[285] D.H. Kim, J. Chen, R.A. Omary, A.C. Larson, MRI visible drug eluting magnetic microspheres for transcatheter intra-arterial delivery to liver tumors, Theranostics 5 (5) (2015) 477–488.
[286] H. Chen, T. Liu, Z. Su, L. Shang, G. Wei, 2D transition metal dichalcogenide nanosheets for photo/thermo-based tumor imaging and therapy, Nanoscale horizons 3 (2) (2018) 74–89.
[287] L.L. Chen, J. Xu, Y. Wang, R.Q. Huang, Ultra-small MoS2 nanodots-incorporated mesoporous silica nanospheres for pH-sensitive drug delivery and CT imaging, J. Mater. Sci. Technol. 63 (2021) 91–96.
[288] J. Wang, Z. Li, Y. Yin, H. Liu, G. Tang, Y. Ma, X. Feng, H. Mei, J. Bi, K. Wang, Z. Chen, Mesoporous silica nanoparticles combined with MoS2 and FITC for fluorescence imaging and photothermal therapy of cancer cells, J. Mater. Sci. 55 (31) (2020) 15263–15274.
[289] J. Han, H. Xia, Y. Wu, S.N. Kong, A. Deivasigamani, R. Xu, K.M. Hui, Y. Kang, Single-layer MoS2 nanosheet grafted upconversion nanoparticles for near-infrared fluorescence imaging-guided deep tissue cancer phototherapy, Nanoscale 8 (15) (2016) 7861–7865.
[290] S. Wang, Y. Chen, X. Li, W. Gao, L. Zhang, J. Liu, Y. Zheng, H. Chen, J. Shi, Injectable 2D MoS2 -integrated drug delivering implant for highly efficient NIR-triggered synergistic tumor hyperthermia, Adv. Mater. 27 (44) (2015) 7117–7122.
[291] Z. Zhou, B. Li, C. Shen, D. Wu, H. Fan, J. Zhao, H. Li, Z. Zeng, Z. Luo, L. Ma, C. Tan, Metallic 1T phase enabling MoS2 nanodots as an efficient agent for photoacoustic imaging guided photothermal therapy in the near-infrared-II window, Small 16 (43) (2020), e2004173.
[292] C. Song, C. Yang, F. Wang, D. Ding, Y. Gao, W. Guo, M. Yan, S. Liu, C. Guo, MoS2-Based multipurpose theranostic nanoplatform: realizing dual-imaging-guided combination phototherapy to eliminate solid tumor via a liquefaction necrosis process, J. Mater. Chem. B. 5 (45) (2017) 9015–9024.
[293] M.H. Shin, E.Y. Park, S. Han, H.S. Jung, D.H. Keum, G.H. Lee, T. Kim, C. Kim, K. S. Kim, S.H. Yun, S.K. Hahn, Multimodal cancer theranosis using hyaluronate-conjugated molybdenum disulfide, Advanced healthcare materials 8 (1) (2019), e1801036.
[294] Q. Tian, J. Hu, Y. Zhu, R. Zou, Z. Chen, S. Yang, R. Li, Q. Su, Y. Han, X. Liu, Sub-10 nm Fe3O4@Cu(2-x)S core-shell nanoparticles for dual-modal imaging and photothermal therapy, J. Am. Chem. Soc. 135 (23) (2013) 8571–8577.
[295] X. Meng, Z. Liu, Y. Cao, W. Dai, K. Zhang, H. Dong, X. Feng, X. Zhang, Fabricating aptamer-conjugated PEGylated-MoS2/Cu1.8 S theranostic nanoplatform for multiplexed imaging diagnosis and chemo-photothermal therapy of cancer, Adv. Funct. Mater. 27 (16) (2017) 1605592.
[296] L.S. Bouchard, M.S. Anwar, G.L. Liu, B. Hann, Z.H. Xie, J.W. Gray, X. Wang, A. Pines, F.F. Chen, Picomolar sensitivity MRI and photoacoustic imaging of cobalt nanoparticles, Proc. Natl. Acad. Sci. U. S. A 106 (11) (2009) 4085–4089.
[297] J.W. Bulte, D.L. Kraitchman, Iron oxide MR contrast agents for molecular and cellular imaging, NMR Biomed. 17 (7) (2004) 484–499.
[298] H.B. Na, J.H. Lee, K. An, Y.I. Park, M. Park, I.S. Lee, D.H. Nam, S.T. Kim, S.H. Kim, S.W. Kim, K.H. Lim, K.S. Kim, S.O. Kim, T. Hyeon, Development of a T1 contrast agent for magnetic resonance imaging using MnO nanoparticles, Angew. Chem. 46 (28) (2007) 5397–5401.
[299] C.T. Yavuz, J.T. Mayo, W.W. Yu, A. Prakash, J.C. Falkner, S. Yean, L. Cong, H. J. Shipley, A. Kan, M. Tomson, D. Natelson, V.L. Colvin, Low-field magnetic separation of monodisperse Fe3O4 nanocrystals, Science (New York, N.Y.). 314 (5801) (2006) 964–967.
[300] F. Hu, K.W. Macrenaris, E.A. Waters, E.A. Schultz-Sikma, A.L. Eckermann, T. J. Meade, Highly dispersible, superparamagnetic magnetite nanoflowers for magnetic resonance imaging, Chem. Commun. 46 (1) (2010) 73–75.
[301] B. Liu, C. Li, G. Chen, B. Liu, X. Deng, Y. Wei, J. Xia, B. Xing, P. Ma, J. Lin, Synthesis and optimization of MoS2@Fe3O4-ICG/Pt(IV) nanoflowers for MR/IR/PA bioimaging and combined PTT/PDT/chemotherapy triggered by 808 nm laser, Advanced science 4 (8) (2017) 1600540.
[302] Z. Zhao, Z. Zhou, J. Bao, Z. Wang, J. Hu, X. Chi, K. Ni, R. Wang, X. Chen, Z. Chen, J. Gao, Octapod iron oxide nanoparticles as high-performance T_2 contrast agents for magnetic resonance imaging, Nat. Commun. 4 (2013) 2266.
[303] W. Xie, Q. Gao, D. Wang, Z. Guo, F. Gao, X. Wang, Q. Cai, S.-s. Feng, H. Fan, X. Sun, L. Zhao, Doxorubicin-loaded Fe3O4@MoS2-PEG-2DG nanocubes as a theranostic platform for magnetic resonance imaging-guided chemo-photothermal therapy of breast cancer, Nano Research 11 (5) (2018) 2470–2487.
[304] N.J.J. Johnson, W. Oakden, G.J. Stanisz, R.S. Prosser, F.C.J.M. van Veggel, Size-tunable, ultrasmall NaGdF4Nanoparticles: insights into their T1MRI contrast enhancement, Chem. Mater. 23 (21) (2011), 4877-4877.
[305] L. Chen, X. Zhou, W. Nie, W. Feng, Q. Zhang, W. Wang, Y. Zhang, Z. Chen, P. Huang, C. He, Marriage of albumin-gadolinium complexes and MoS2 nanoflakes as cancer theranostics for dual-modality magnetic resonance/photoacoustic imaging and photothermal therapy, ACS Appl. Mater. Interfaces 9 (21) (2017) 17786–17798.
[306] Y. Zhang, J.D. Lin, V. Vijayaragavan, K.K. Bhakoo, T.T. Tan, Tuning sub-10 nm single-phase NaMnF3 nanocrystals as ultrasensitive hosts for pure intense fluorescence and excellent T1 magnetic resonance imaging, Chem. Commun. 48 (83) (2012) 10322–10324.
[307] X. Jing, Z. Zhi, D. Wang, J. Liu, Y. Shao, L. Meng, Multifunctional nanoflowers for simultaneous multimodal imaging and high-sensitivity chemo-photothermal treatment, Bioconjugate Chem. 29 (2) (2018) 559–570.
[308] Y. Liu, P. Bhattarai, Z. Dai, X. Chen, Photothermal therapy and photoacoustic imaging via nanotheranostics in fighting cancer, Chem. Soc. Rev. 48 (7) (2019) 2053–2108.
[309] J. Jin, M. Guo, J. Liu, Graphdiyne nanosheet-based drug delivery platform for photothermal/chemotherapy combination Treatment of Cancer, 10, 2018, pp. 8436–8442, 10.
[310] C. Xing, S. Chen, X. Liang, Q. Liu, M. Qu, Q. Zou, J. Li, H. Tan, L. Liu, D. Fan, H. Zhang, Two-dimensional MXene (Ti(3)C(2))-integrated cellulose hydrogels: toward smart three-dimensional network nanoplatforms exhibiting light-induced swelling and bimodal photothermal/chemotherapy, Anticancer Activity 10 (33) (2018) 27631–27643.
[311] T. Araki, K. Ogawara, H. Suzuki, R. Kawai, T. Watanabe, T. Ono, K. Higaki, Augmented EPR effect by photo-triggered tumor vascular treatment improved therapeutic efficacy of liposomal paclitaxel in mice bearing tumors with low permeable vasculature, J. Contr. Release : official journal of the Controlled Release Society 200 (2015) 106–114.
[312] E. Debefve, F. Mithieux, J.Y. Perentes, Y. Wang, C. Cheng, S.C. Schaefer, C. Ruffieux, J.P. Ballini, M. Gonzalez, H. van den Bergh, H.B. Ris, H.A. Lehr, T. Krueger, Leukocyte-endothelial cell interaction is necessary for photodynamic therapy induced vascular permeabilization, Laser Surg. Med. 43 (7) (2011) 696–704.
[313] X. Wang, F. Li, X. Yan, Y. Ma, Z.H. Miao, L. Dong, H. Chen, Y. Lu, Z. Zha, Ambient aqueous synthesis of ultrasmall Ni(0.85)Se nanoparticles for noninvasive photoacoustic imaging and combined, Photothermal-Chemotherapy of Cancer 9 (48) (2017) 41782–41793.
[314] Y. Yang, J. Wu, D.H. Bremner, S. Niu, Y. Li, X. Zhang, X. Xie, L.M. Zhu, A multifunctional nanoplatform based on MoS2-nanosheets for targeted drug delivery and chemo-photothermal therapy, Colloids Surf. B Biointerfaces 185 (2020) 110585.
[315] X. Zhang, J. Wu, G.R. Williams, S. Niu, Q. Qian, L.M. Zhu, Functionalized MoS(2)-nanosheets for targeted drug delivery and chemo-photothermal therapy, Colloids Surf. B Biointerfaces 173 (2019) 101–108.
[316] X. Zhang, J. Wu, G.R. Williams, Y. Yang, S. Niu, Q. Qian, L.M. Zhu, Dual-responsive molybdenum disulfide/copper sulfide-based delivery systems for enhanced chemo-photothermal therapy, J. Colloid Interface Sci. 539 (2019) 433–441.
[317] M. Xu, K. Zhang, Y. Liu, J. Wang, K. Wang, Y. Zhang, Multifunctional MoS(2) nanosheets with Au NPs grown in situ for synergistic chemo-photothermal therapy, Colloids Surf. B Biointerfaces 184 (2019) 110551.
[318] Y. Liu, A. Lin, J. Liu, X. Chen, X. Zhu, Y. Gong, G. Yuan, L. Chen, J. Liu, Enzyme-Responsive Mesoporous Ruthenium for Combined Chemo-Photothermal Therapy of Drug-Resistant Bacteria, 11, 2019, pp. 26590–26606, 30.
[319] C. Zhang, D. Zhang, J. Liu, J. Wang, Y. Lu, J. Zheng, B. Li, L. Jia, Functionalized MoS(2)-erlotinib produces hyperthermia under NIR, J. Nanobiotechnol. 17 (1) (2019) 76.
[320] Y. Yang, B. Gong, Y. Yang, A. Xie, Y. Shen, M. Zhu, Construction and synergistic anticancer efficacy of magnetic targeting cabbage-like Fe3O4@MoS2@ZnO drug carriers, J. Mater. Chem. B. 6 (22) (2018) 3792–3799.
[321] S. Cai, J. Yan, H. Xiong, Q. Wu, H. Xing, Y. Liu, S. Liu, Z. Liu, Aptamer-functionalized molybdenum disulfide nanosheets for tumor cell targeting and lysosomal acidic environment/NIR laser responsive drug delivery to realize synergetic chemo-photothermal therapeutic effects, Int. J. Pharm. 590 (2020) 119948.
[322] T. Shao, J. Wen, Q. Zhang, Y. Zhou, L. Liu, L. Yuwen, Y. Tian, Y. Zhang, W. Tian, Y. Su, Z. Teng, G. Lu, J. Xu, NIR photoresponsive drug delivery and synergistic chemo-photothermal therapy by monodispersed-MoS2-nanosheets wrapped periodic mesoporous organosilicas, J. Mater. Chem. B. 4 (47) (2016) 7708–7717.

[323] A. Zhang, A. Li, W. Tian, Z. Li, C. Wei, Y. Sun, W. Zhao, M. Liu, J. Liu, A target-directed chemo-photothermal system based on transferrin and copolymer-modified MoS(2) nanoplates with pH-activated drug release, Chemistry 23 (47) (2017) 11346–11356.
[324] J. Zhao, Y. Zhu, C. Ye, Y. Chen, S. Wang, D. Zou, Z. Li, Photothermal transforming agent and chemotherapeutic co-loaded electrospun nanofibers for tumor treatment, Int. J. Nanomed. 14 (2019) 3893–3909.
[325] K. Wang, Q. Chen, W. Xue, S. Li, Z. Liu, Combined chemo-photothermal antitumor therapy using molybdenum disulfide modified with hyperbranched polyglycidyl, ACS Biomater. Sci. Eng. 3 (10) (2017) 2325–2335.
[326] M. Xie, N. Yang, J. Cheng, M. Yang, T. Deng, Y. Li, C. Feng, Layered MoS(2) nanosheets modified by biomimetic phospholipids: enhanced stability and its synergistic treatment of cancer with chemo-photothermal therapy, Colloids Surf. B Biointerfaces 187 (2020) 110631.
[327] J. Liu, J. Zheng, H. Nie, H. Chen, B. Li, L. Jia, Co-delivery of erlotinib and doxorubicin by MoS2 nanosheets for synergetic photothermal chemotherapy of cancer, Chem. Eng. J. 381 (2020) 122541.
[328] C. Xu, Z. Teng, Y. Zhang, L. Yuwen, Q. Zhang, X. Su, M. Dang, Y. Tian, J. Tao, L. Bao, B. Yang, G. Lu, J. Zhu, Flexible MoS2 -embedded human serum albumin hollow nanocapsules with long circulation times and high targeting ability for efficient tumor ablation, Adv. Funct. Mater. 28 (45) (2018) 1804081.
[329] Y. Yang, Y. Niu, J. Zhang, A.K. Meka, H. Zhang, C. Xu, C.X. Lin, M. Yu, C. Yu, Biphasic synthesis of large-pore and well-dispersed benzene bridged mesoporous organosilica nanoparticles for intracellular protein delivery, Small 11 (23) (2015) 2743–2749.
[330] Z. Teng, S. Wang, X. Su, G. Chen, Y. Liu, Z. Luo, W. Luo, Y. Tang, H. Ju, D. Zhao, G. Lu, Facile synthesis of yolk-shell structured inorganic-organic hybrid spheres with ordered radial mesochannels, Adv. Mater. 26 (22) (2014) 3741–3747.
[331] J. Croissant, X. Cattoën, M.W. Man, A. Gallud, L. Raehm, P. Trens, M. Maynadier, J.O. Durand, Biodegradable ethylene-bis(propyl)disulfide-based periodic mesoporous organosilica nanorods and nanospheres for efficient in-vitro drug delivery, Adv. Mater. 26 (35) (2014) 6174–6180.
[332] G. Casillas, U. Santiago, H. Barrón, D. Alducin, A. Ponce, M. José-Yacamán, Elasticity of MoS(2) sheets by mechanical deformation observed by in situ electron microscopy, The journal of physical chemistry. C, Nanomaterials and interfaces 119 (1) (2015) 710–715.
[333] X. Duan, C. Wang, A. Pan, R. Yu, X. Duan, Two-dimensional transition metal dichalcogenides as atomically thin semiconductors: opportunities and challenges, Chem. Soc. Rev. 44 (24) (2015) 8859–8876.
[334] X. Su, J. Wang, J. Zhang, L. Yuwen, Q. Zhang, M. Dang, J. Tao, X. Ma, S. Wang, Z. Teng, Synthesis of sandwich-like molybdenum sulfide/mesoporous organosilica nanosheets for photo-thermal conversion and stimuli-responsive drug release, J. Colloid Interface Sci. 496 (2017) 261–266.
[335] Y. Liu, K. Ai, J. Liu, M. Deng, Y. He, L. Lu, Dopamine-melanin colloidal nanospheres: an efficient near-infrared photothermal therapeutic agent for in vivo cancer therapy, Adv. Mater. 25 (9) (2013) 1353–1359.
[336] X. Zhang, Z. Zhao, P. Yang, W. Liu, J. Fan, B. Zhang, S. Yin, MoS2@C nanosphere as near infrared/pH dual response platform for chemical photothermal combination treatment, Colloids Surf. B Biointerfaces 192 (2020) 111054.
[337] M. Ma, Y. Huang, H. Chen, X. Jia, S. Wang, Z. Wang, J. Shi, Bi2S3-embedded mesoporous silica nanoparticles for efficient drug delivery and interstitial radiotherapy sensitization, Biomaterials 37 (2015) 447–455.
[338] Y. Huang, Y. Luo, W. Zheng, T. Chen, Rational design of cancer-targeted BSA protein nanoparticles as radiosensitizer to overcome cancer radioresistance, ACS Appl. Mater. Interfaces 6 (21) (2014) 19217–19228.
[339] C.W. Hsiao, E.Y. Chuang, H.L. Chen, D. Wan, C. Korupalli, Z.X. Liao, Y.L. Chiu, W. T. Chia, K.J. Lin, H.W. Sung, Photothermal tumor ablation in mice with repeated therapy sessions using NIR-absorbing micellar hydrogels formed in situ, Biomaterials 56 (2015) 26–35.
[340] W. Fu, X. Zhang, L. Mei, R. Zhou, W. Yin, Q. Wang, Z. Gu, Y. Zhao, Stimuli-responsive small-on-large nanoradiosensitizer for enhanced tumor penetration and radiotherapy sensitization, ACS Nano 14 (8) (2020) 10001–10017.
[341] E. Verron, H. Schmid-Antomarchi, H. Pascal-Mousselard, A. Schmid-Alliana, J. C. Scimeca, J.M. Bouler, Therapeutic strategies for treating osteolytic bone metastases, Drug Discov. Today 19 (9) (2014) 1419–1426.
[342] H. Ma, C. Jiang, D. Zhai, Y. Luo, Y. Chen, F. Lv, Z. Yi, Y. Deng, J. Wang, J. Chang, C. Wu, A bifunctional biomaterial with photothermal effect for tumor therapy and bone regeneration, Adv. Funct. Mater. 26 (8) (2016) 1197–1208.
[343] C. Marques, J.M. Ferreira, E. Andronescu, D. Ficai, M. Sonmez, A. Ficai, Multifunctional materials for bone cancer treatment, Int. J. Nanomed. 9 (2014) 2713–2725.
[344] M. Xu, H. Li, D. Zhai, J. Chang, S. Chen, C. Wu, Hierarchically porous nagelschmidtite bioceramic-silk scaffolds for bone tissue engineering, J. Mater. Chem. B. 3 (18) (2015) 3799–3809.
[345] A.V. Do, B. Khorsand, S.M. Geary, A.K. Salem, 3D printing of scaffolds for tissue regeneration applications, Advanced healthcare materials 4 (12) (2015) 1742–1762.
[346] X. Wang, T. Li, H. Ma, D. Zhai, C. Jiang, J. Chang, J. Wang, C. Wu, A 3D-printed scaffold with MoS2 nanosheets for tumor therapy and tissue regeneration, NPG Asia Mater. 9 (4) (2017) e376-e376.
[347] W. Hou, P. Wei, L. Kong, R. Guo, S. Wang, X. Shi, Partially PEGylated dendrimer-entrapped gold nanoparticles: a promising nanoplatform for highly efficient DNA and siRNA delivery, J. Mater. Chem. B. 4 (17) (2016) 2933–2943.
[348] J. Kim, H. Kim, W.J. Kim, Single-layered MoS2-PEI-PEG nanocomposite-mediated gene delivery controlled by photo and redox stimuli, Small 12 (9) (2016) 1184–1192.
[349] R. Mandal, K. Strebhardt, Plk1: unexpected roles in DNA replication, Cell Res. 23 (11) (2013) 1251–1253.
[350] K.E. Mundt, R.M. Golsteyn, H.A. Lane, E.A. Nigg, On the regulation and function of human polo-like kinase 1 (PLK1): effects of overexpression on cell cycle progression, Biochem. Biophys. Res. Commun. 239 (2) (1997) 377–385.
[351] R. Pellegrino, D.F. Calvisi, S. Ladu, V. Ehemann, T. Staniscia, M. Evert, F. Dombrowski, P. Schirmacher, T. Longerich, Oncogenic and tumor suppressive roles of polo-like kinases in human hepatocellular carcinoma, Hepatology (Baltimore, Md.) 51 (3) (2010) 857–868.
[352] Z. Kou, X. Wang, R. Yuan, H. Chen, Q. Zhi, L. Gao, B. Wang, Z. Guo, X. Xue, W. Cao, L. Guo, A promising gene delivery system developed from PEGylated MoS2 nanosheets for gene therapy, Nanoscale research letters 9 (1) (2014) 587.
[353] A. Vincent, J. Herman, R. Schulick, R.H. Hruban, M. Goggins, Pancreatic cancer, Lancet (London, England) 378 (9791) (2011) 607–620.
[354] M. Goggins, K.A. Overbeek, Management of patients with increased risk for familial pancreatic cancer: updated recommendations from the International Cancer of the Pancreas Screening (CAPS) Consortium, 69, 2020, pp. 7–17, 1.
[355] F. McAllister, M.A.W. Khan, B. Helmink, J.A. Wargo, The tumor microbiome in pancreatic cancer: bacteria and beyond, Canc. Cell 36 (6) (2019) 577–579.
[356] C. Nevala-Plagemann, M. Hidalgo, I. Garrido-Laguna, From state-of-the-art treatments to novel therapies for advanced-stage pancreatic cancer, Nature reviews. Clin. Oncol. 17 (2) (2020) 108–123.
[357] M.A. Glozak, E. Seto, Histone deacetylases and cancer, Oncogene 26 (37) (2007) 5420–5432.
[358] G. Lin, R. Hu, W.C. Law, C.K. Chen, Y. Wang, H. Li Chin, Q.T. Nguyen, C.K. Lai, H. S. Yoon, X. Wang, G. Xu, L. Ye, C. Cheng, K.T. Yong, Biodegradable nanocapsules as siRNA carriers for mutant K-Ras gene silencing of human pancreatic carcinoma cells, Small 9 (16) (2013) 2757–2763.
[359] H.J. Xie, J.H. Noh, J.K. Kim, K.H. Jung, J.W. Eun, H.J. Bae, M.G. Kim, Y.G. Chang, J.Y. Lee, H. Park, S.W. Nam, HDAC1 inactivation induces mitotic defect and caspase-independent autophagic cell death in liver cancer, PloS One 7 (4) (2012), e34265.
[360] F.L. Delarue, J. Adnane, B. Joshi, M.A. Blaskovich, D.A. Wang, J. Hawker, F. Bizouarn, J. Ohkanda, K. Zhu, A.D. Hamilton, S. Chellappan, S.M. Sebti, Farnesyltransferase and geranylgeranyltransferase I inhibitors upregulate RhoB expression by HDAC1 dissociation, HAT association and histone acetylation of the RhoB promoter, Oncogene 26 (5) (2007) 633–640.
[361] F. Yin, T. Anderson, N. Panwar, K. Zhang, S.C. Tjin, B.K. Ng, H.S. Yoon, J. Qu, K. T. Yong, Functionalized MoS2 nanosheets as multi-gene delivery vehicles for in vivo pancreatic cancer therapy, Nanotheranostics 2 (4) (2018) 371–386.
[362] J.E. Chipuk, T. Moldoveanu, F. Llambi, M.J. Parsons, D.R. Green, The BCL-2 family reunion, Mol. Cell 37 (3) (2010) 299–310.
[363] L. Kong, L. Xing, B. Zhou, L. Du, X. Shi, Dendrimer-modified MoS2 nanoflakes as a platform for combinational gene silencing and photothermal therapy of tumors, ACS Appl. Mater. Interfaces 9 (19) (2017) 15995–16005.
[364] Y. Yang, Cancer immunotherapy: harnessing the immune system to battle cancer, J. Clin. Invest. 125 (9) (2015) 3335–3337.
[365] C. Bode, G. Zhao, F. Steinhagen, T. Kinjo, D.M. Klinman, CpG DNA as a vaccine adjuvant, Expet Rev. Vaccine 10 (4) (2011) 499–511.
[366] Q. Han, X. Wang, X. Jia, S. Cai, W. Liang, Y. Qin, R. Yang, C. Wang, CpG loaded MoS2 nanosheets as multifunctional agents for photothermal enhanced cancer immunotherapy, Nanoscale 9 (18) (2017) 5927–5934.
[367] C. Zhang, W. Bu, D. Ni, S. Zhang, Q. Li, Z. Yao, J. Zhang, H. Yao, Z. Wang, J. Shi, Synthesis of iron nanometallic glasses and their application in cancer therapy by a localized Fenton reaction, Angew. Chem. 55 (6) (2016) 2101–2106.
[368] J. Yu, D. Ma, L. Mei, Q. Gao, W. Yin, X. Zhang, L. Yan, Z. Gu, X. Ma, Y. Zhao, Peroxidase-like activity of MoS(2) nanoflakes with different modifications and their application for H(2)O(2) and glucose detection, J. Mater. Chem. B. 6 (3) (2018) 487–498.
[369] S.K. Maji, S. Yu, K. Chung, M. Sekkarapatti Ramasamy, J.W. Lim, J. Wang, H. Lee, D.H. Kim, Synergistic nanozymetic activity of hybrid gold bipyramid-molybdenum disulfide Core@Shell nanostructures for two-photon imaging and anticancer therapy, ACS Appl. Mater. Interfaces 10 (49) (2018) 42068–42076.
[370] L. Mei, D. Ma, Q. Gao, X. Zhang, W. Fu, X. Dong, G. Xing, W. Yin, Z. Gu, Y. Zhao, Glucose-responsive cascaded nanocatalytic reactor with self-modulation of the tumor microenvironment for enhanced chemo-catalytic therapy, Materials Horizons 7 (7) (2020) 1834–1844.
[371] H. Zheng, S. Wang, L. Zhou, X. He, Z. Cheng, F. Cheng, Z. Liu, X. Wang, Y. Chen, Q. Zhang, Injectable multi-responsive micelle/nanocomposite hybrid hydrogel for bioenzyme and photothermal augmented chemodynamic therapy of skin cancer and bacterial infection, Chem. Eng. J. 404 (2021) 126439.
[372] S. Zhang, L. Jin, J. Liu, Y. Liu, T. Zhang, Y. Zhao, N. Yin, R. Niu, X. Li, D. Xue, S. Song, Y. Wang, H. Zhang, Boosting chemodynamic therapy by the synergistic effect of Co-catalyze and photothermal effect triggered by the second near-infrared light, Nano-Micro Lett. 12 (1) (2020).
[373] F. Jiang, B. Ding, S. Liang, Y. Zhao, Z. Cheng, B. Xing, P. Ma, J. Lin, Intelligent MoS2-CuO heterostructures with multiplexed imaging and remarkably enhanced antitumor efficacy via synergetic photothermal therapy/chemodynamic therapy/immunotherapy, Biomaterials 268 (2021) 120545.
[374] D. Zhang, P. Cui, Z. Dai, B. Yang, X. Yao, Q. Liu, Z. Hu, X. Zheng, Tumor microenvironment responsive FePt/MoS2 nanocomposites with chemotherapy and photothermal therapy for enhancing cancer immunotherapy, Nanoscale 11 (42) (2019) 19912–19922.
[375] Z. Wang, B. Guo, Microfluidics-prepared uniform conjugated polymer nanoparticles for photo-triggered immune microenvironment modulation and cancer Therapy, 11, 2019, pp. 11167–11176, 12.

[376] X. Yu, D. Gao, L. Gao, J. Lai, C. Zhang, Y. Zhao, L. Zhong, B. Jia, F. Wang, X. Chen, Inhibiting metastasis and preventing tumor relapse by triggering host immunity with tumor-targeted photodynamic therapy using photosensitizer-loaded, Functional Nanographenes 11 (10) (2017) 10147–10158.
[377] R. Jin, J. Yang, P. Ding, C. Li, B. Zhang, W. Chen, Y.D. Zhao, Y. Cao, B. Liu, Antitumor immunity triggered by photothermal therapy and photodynamic therapy of a 2D MoS(2) nanosheet-incorporated injectable polypeptide-engineered hydrogel combinated with chemotherapy for 4T1 breast tumor therapy, Nanotechnology 31 (20) (2020) 205102.
[378] V.V. Singh, K. Kaufmann, B.E.-F. de Ávila, E. Karshalev, J. Wang, Molybdenum disulfide-based tubular microengines: toward biomedical applications, Adv. Funct. Mater. 26 (34) (2016) 6270–6278.
[379] B.L. Li, M.I. Setyawati, L. Chen, J. Xie, K. Ariga, C.T. Lim, S. Garaj, D.T. Leong, Directing assembly and disassembly of 2D MoS2 nanosheets with DNA for drug delivery, ACS Appl. Mater. Interfaces 9 (18) (2017) 15286–15296.
[380] S. Ariyasu, J. Mu, X. Zhang, Y. Huang, E.K.L. Yeow, H. Zhang, B. Xing, Investigation of thermally induced cellular ablation and heat response triggered by planar MoS2-based nanocomposite, Bioconjugate Chem. 28 (4) (2017) 1059–1067.
[381] L. Liu, J. Wang, X. Tan, X. Pang, Q. You, Q. Sun, F. Tan, N. Li, Photosensitizer loaded PEG-MoS2-Au hybrids for CT/NIRF imaging-guided stepwise photothermal and photodynamic therapy, J. Mater. Chem. B. 5 (12) (2017) 2286–2296.
[382] J. Xu, A. Gulzar, Y. Liu, H. Bi, S. Gai, B. Liu, D. Yang, F. He, P. Yang, Integration of IR-808 sensitized upconversion nanostructure and MoS2 nanosheet for 808 nm NIR light triggered phototherapy and bioimaging, Small 13 (36) (2017).
[383] B. Geng, H. Qin, F. Zheng, W. Shen, P. Li, K. Wu, X. Wang, X. Li, D. Pan, L. Shen, Carbon dot-sensitized MoS2 nanosheet heterojunctions as highly efficient NIR photothermal agents for complete tumor ablation at an ultralow laser exposure, Nanoscale 11 (15) (2019) 7209–7220.
[384] J. Liu, J. Zheng, H. Nie, D. Zhang, D. Cao, Z. Xing, B. Li, L. Jia, Molybdenum disulfide-based hyaluronic acid-guided multifunctional theranostic nanoplatform for magnetic resonance imaging and synergetic chemo-photothermal therapy, J. Colloid Interface Sci. 548 (2019) 131–144.
[385] W. Wei, X. Zhang, S. Zhang, G. Wei, Z. Su, Biomedical and bioactive engineered nanomaterials for targeted tumor photothermal therapy: a review, Materials science & engineering. C, Materials for biological applications 104 (2019) 109891.
[386] Y. Chen, Y. Wu, B. Sun, S. Liu, H. Liu, Two-dimensional nanomaterials for cancer nanotheranostics, Small 13 (10) (2017).
[387] L. Cheng, X. Wang, F. Gong, T. Liu, Z. Liu, 2D nanomaterials for cancer theranostic applications, Adv. Mater. 32 (13) (2020), e1902333.
[388] L. Fusco, A. Gazzi, G. Peng, Y. Shin, S. Vranic, D. Bedognetti, F. Vitale, A. Yilmazer, X. Feng, B. Fadeel, C. Casiraghi, L.G. Delogu, Graphene and other 2D materials: a multidisciplinary analysis to uncover the hidden potential as cancer theranostics, Theranostics 10 (12) (2020) 5435–5488.
[389] X. Li, J. Shan, W. Zhang, S. Su, L. Yuwen, L. Wang, Recent advances in synthesis and biomedical applications of two-dimensional transition metal dichalcogenide nanosheets, Small 13 (5) (2017).
[390] S. Liu, X. Pan, H. Liu, Two-dimensional nanomaterials for photothermal therapy, Angew. Chem. 59 (15) (2020) 5890–5900.
[391] C. Murugan, V. Sharma, R.K. Murugan, G. Malaimegu, A. Sundaramurthy, Two-dimensional cancer theranostic nanomaterials: synthesis, surface functionalization and applications in photothermal therapy, J. Contr. Release : official journal of the Controlled Release Society 299 (2019) 1–20.
[392] J. Shi, J. Li, Y. Wang, J. Cheng, C.Y. Zhang, Recent advances in MoS2-based photothermal therapy for cancer and infectious disease treatment, J. Mater. Chem. B. 8 (27) (2020) 5793–5807.
[393] V. Urbanova, M. Pumera, Biomedical and bioimaging applications of 2D pnictogens and transition metal dichalcogenides, Nanoscale 11 (34) (2019) 15770–15782.
[394] X. Wang, L. Cheng, Multifunctional two-dimensional nanocomposites for photothermal-based combined cancer therapy, Nanoscale 11 (34) (2019) 15685–15708.
[395] W. Zhao, A. Li, A. Zhang, Y. Zheng, J. Liu, Recent advances in functional-polymer-decorated transition-metal nanomaterials for bioimaging and cancer therapy, ChemMedChem 13 (20) (2018) 2134–2149.
[396] G. Guan, E. Ye, M. You, Z. Li, Hybridized 2D nanomaterials toward highly efficient photocatalysis for degrading pollutants, Current Status and Future Perspectives 16 (19) (2020), e1907087.
[397] X. Zhang, C. Gong, O.U. Akakuru, Z. Su, A. Wu, G. Wei, The design and biomedical applications of self-assembled two-dimensional organic biomaterials, Chem. Soc. Rev. 48 (23) (2019) 5564–5595.
[398] G. Reina, J.M. González-Domínguez, Promises, facts and challenges for graphene in biomedical applications, 46, 2017, pp. 4400–4416, 15.